Master's thesis

NTNU
Norwegian University of Science and Technology
Faculty of Engineering
Department of Energy and Process Engineering

Henrik Brude and Mari Skjærpe

Field Development Study of Combined Well Cleanup and Dewatering to Shore on Tanzania Block 2

Master's thesis in Energy and Process Engineering
Supervisor: Ole Jørgen Nydal
June 2020

NTNU
Norwegian University of
Science and Technology

Henrik Brude and Mari Skjærpe

Field Development Study of Combined Well Cleanup and Dewatering to Shore on Tanzania Block 2

Master's thesis in Energy and Process Engineering
Supervisor: Ole Jørgen Nydal
June 2020

Norwegian University of Science and Technology
Faculty of Engineering
Department of Energy and Process Engineering

NTNU
Norwegian University of
Science and Technology

Norwegian University of Science and Technology

Faculty of Engineering
Department of Energy and Process Engineering

EPT-M-2020-XX

MASTER THESIS

for

Henrik Brude and Mari Skjærpe

Spring 2020

Field development study of combined well cleanup and dewatering to shore on Tanzania Block 2 field

Feltutvikling-studie av kombinert brønnopprensking og avvanning til land på Tanzania Block 2 feltet

Background and objective

Operational improvements aiming at economic savings and reduced environmental impacts are highly emphasized in the oil and gas industry. Cleanup of offshore wells is associated with a relatively high environmental impact, in addition to being a costly operation, as it requires presence of a rig or vessel. Thus, one initiative aiming at the aforementioned improvements is to perform well cleanup to the production facilities onshore instead of to an offshore rig, which will both economize rig days and reduce the environmental impact. Cleanup to shore has already been carried out successfully at the Snøhvit field at the Norwegian Continental Shelf.

The aim of this thesis is to investigate the contingencies of well cleanup to shore, combined with dewatering of the trunkline for a gas-condensate field on Block 2 offshore Tanzania. Initial well conditions inhibit an efficient startup and well unloading. Thus, gravity driven mud drainage to the near-wellbore zone during well suspension is investigated as a possible solution. Furthermore, emphasis is made on the flushing of filtrate in the near-wellbore zone during early production, along with predictions of the period of time the drilling- and completion fluids will affect the production.

The following tasks are to be considered:

1 Establish models in OLGA and ROCX
2 Conduct comprehensive simulations using the models
3 Assess the effect of reservoir- and mud cake properties
4 Evaluate the results
5 Reporting

Within 14 days of receiving the written text on the master thesis, the candidate shall submit a research plan for his project to the department.

When the thesis is evaluated, emphasis is put on processing of the results, and that they are presented in tabular and/or graphic form in a clean manner, and that they are analysed carefully.

The thesis should be formulated as a research report with summary both in English and Norwegian, conclusion, literature references, table of contents etc. During the preparation of the text, the candidate should make an effort to produce a well-structured and easily readable report. In order to ease the evaluation of the thesis, it is important that the cross-references are correct. In the making of the report, strong emphasis should be placed on both a thorough discussion of the results and an orderly presentation.

The candidate is requested to initiate and keep close contact with his/her academic supervisor(s) throughout the working period. The candidate must follow the rules and regulations of NTNU as well as passive directions given by the Department of Energy and Process Engineering.

Risk assessment of the candidate's work shall be carried out according to the department's procedures. The risk assessment must be documented and included as part of the final report. Events related to the candidate's work adversely affecting the health, safety or security, must be documented and included as part of the final report. If the documentation on risk assessment represents a large number of pages, the full version is to be submitted electronically to the supervisor and an excerpt is included in the report.

Pursuant to “Regulations concerning the supplementary provisions to the technology study program/Master of Science” at NTNU § 20, the Department reserves the permission to utilize all the results and data for teaching and research purposes as well as in future publications.

The final report is to be submitted digitally in DAIM. An executive summary of the thesis, including title, student’s name, supervisor’s name, year, department name, and NTNU’s logo and name, shall be submitted to the department as a separate pdf file. Based on an agreement with the supervisor, the final report and other material and documents may be given to the supervisor in digital form.

☐ Work to be done in lab (Water power lab, Fluids engineering lab, Thermal engineering lab)
☐ Field work

Department for Energy and Process Engineering, *June 2020*

Ole Jorgen Nydal
Academic Supervisor

Co-Supervisor(s): Even Solbraa

Abstract

Operational improvements aiming at economic savings and reduced environmental impacts are highly emphasized in the oil and gas industry. Cleanup of offshore wells is associated with a relatively high environmental impact, in addition to being a costly operation, as it requires the presence of a rig or vessel. Thus, one initiative aiming at the aforementioned improvements is to perform well cleanup to the production facilities onshore instead of to an offshore rig, which will both economize rig days and reduce the environmental impact.

The aim of this thesis is to investigate the contingencies of well cleanup to shore, combined with dewatering of the trunkline for the gas-condensate field Block 2 offshore Tanzania. The technical challenges present on Block 2 along with the development concept to be implemented are presented. Moreover, several startup procedures on Block 2 are suggested and discussed. Comparisons to the challenges and concept solutions implemented on similar fields are presented. A description of the field development phase is presented, including the operations conducted prior to initializing the production. Furthermore, the principles of multiphase flow are highlighted, and the fundamental equations as prerequisites for simulating multiphase flows in porous media and flowlines are presented. Moreover, an introduction to multiphase flow simulations is provided, with emphasis on the simulators utilized in this thesis.

Initial well conditions at Block 2 inhibit an efficient startup and well unloading. Thus, gravity-driven mud drainage to the near-wellbore zone during well suspension is investigated as a possible solution. Furthermore, emphasis is made on the flushing of filtrate in the near-wellbore zone during early production. Of particular interest is the period of time the mud will affect the production. Utilizing a coupled wellbore-reservoir model, constituting an OLGA and a ROCX model, multiphase flow simulations are performed. A comprehensive model verification is conducted, including grid sensitivity studies and sensitivity on reservoir- and fluid parameters to assess their effect on the well drainage and reservoir flushing.

The results reveal that a suspension period of 7 days is required in order to drain a sufficient amount of mud from the well into the reservoir to ensure successful and effective unloading. The suspension period results in a drained mass of 13.7 tons, constituting 13.5 tons of mud and 0.2 tons of brine. The dewatering operation requires approximately 36.5 hours to complete, utilizing a PI controller to retain the pig velocity at 0.8 m/s. After 19 days, the drilling- and completion fluid content in the reservoir is reduced to 0.3 tons, and after 20 days, all the drilling- and completion fluids are produced out of the trunkline.

Sammendrag

Driftsforbedringer med sikte på økonomiske besparelser og reduserte miljøbelastninger er sterkt vektlagt i olje- og gassindustrien. Opprensking av offshore-brønner er forbundet med en relativt høy miljøpåvirkning, i tillegg til å være en kostbar operasjon, ettersom det krever tilstedeværelse av en rigg eller et fartøy. Et initiativ som tar sikte på de nevnte forbedringene er således å utføre brønnopprensking til produksjonsanleggene på land i stedet for til en offshore rigg, noe som både vil spare rigg-dager og redusere miljøbelastningen på grunn av redusert fakling.

Målet med denne masteroppgaven er å undersøke mulighetene for brønnopprensking til land, kombinert med avvanning av rørledningen for gasskondensatfeltet Block 2 offshore Tanzania. De tekniske utfordringene tilstede på Block 2, og utviklingskonseptet som skal implementeres, presenteres i denne oppgaven. Videre foreslås og diskuteres flere oppstartsprosedyrer på Block 2. Sammenligninger med utfordringene og konseptløsningene implementert på lignende felt presenteres. En beskrivelse av feltutviklingsfasen blir lagt frem, inkludert operasjoner som blir utført før produksjon startes opp. Videre blir flerfasestrømning introdusert, og de grunnleggende ligningene for å simulere flerfasestrømninger i porøse medier og rørledninger blir presentert. Videre gis en introduksjon til flerfasestrømssimuleringer, med vekt på simulatorene brukt i denne oppgaven.

De initielle brønnforholdene på Block 2 hemmer en effektiv oppstart og brønnopprenskning. Derfor undersøkes gravitasjonsdrevet boreslamdrenering til nærbrønnen under brønnsuspendering som en mulig løsning. Videre blir det lagt vekt på opprenskingen av boreslam i reservoarsonen nær borehullet under tidlig produksjon. Av stor interesse er perioden boreslammet vil påvirke produksjonen. Ved å benytte en koblet brønn-reservoar-modell, bestående av en OLGA og en ROCX-modell, blir flerfasestrømssimuleringer utført. Det gjennomføres en omfattende modellverifisering, inkludert sensitivitetsstudie av numerisk grid, og sensitivitetsstudie på reservoar- og væskeparametere for å vurdere deres effekt på brønndreneringen og opprenskingen av reservoaret.

Resultatene viser at en suspensjonsperiode på 7 dager er nødvendig for å drenere en tilstrekkelig mengde boreslam fra brønnen og inn i reservoaret, for å sikre en vellykket og effektiv brønnoppstart. Suspensjonsperioden resulterer i en drenert masse på 13.7 tonn, bestående av 13.5 tonn boreslam og 0.2 tonn saltlake. Avvanningsoperasjonen krever omtrent 36.5 timer, ved hjelp en PI-kontroller for å holde pig-hastigheten konstant på 0.8 m/s. Etter 19 dager reduseres boreslammet i reservoaret fra 15 tonn til 0.3 tonn, og etter 20 dager er alt boreslammet produsert ut av rørledningen.

Preface

This master thesis was accomplished at the Department of Energy and Process Engineering at the Norwegian University of Science and Technology. The work was in collaboration with Equinor, with Henning Holm as our contact person for the Tanzania field. Our supervisor has been professor Ole Jørgen Nydal at NTNU, and our co-supervisor has been Even Solbraa from Equinor.

This thesis is an extension of the project work conducted last semester. Consequently, some background theory is retained from the project work, as this still applies for the present thesis. Compared to the project work, this thesis digs more into the numerical aspects, including a more comprehensive grid sensitivity study. Furthermore, more complex physics and startup challenges are considered.

We would like to express our thankfulness to our supervisor, Ole Jørgen, for providing us with an interesting project and for his continuous support and enthusiasm throughout the master period. Thank you for always having an open door and for many good conversations. Further thanks go out to our co-supervisor, Even, and Henning in Equinor for providing us with input from the Block 2 field and reports from the pre-commissioning on Snøhvit and Ormen Lange. As these reports are classified as internal and confidential, these are not cited in this paper. Instead, "ref. Equinor" is used.

Further gratitude to Espen Egner in Schlumberger for hosting us at the office in Asker for a couple of days to get support on our work. A big thank also to Rahel Yusuf in Schlumberger for supporting us in OLGA and ROCX throughout the master period. We would also like to thank Milan Stanko, Pål Skalle and Sigbjørn Stangesland at the Department of Geoscience and Petroleum at NTNU, for their support.

A last big thank goes out to Kimambo Cuthbert and Joseph Kihedu for hosting us for a couple of weeks at the University of Dar es Salaam in Tanzania.

Trondheim, June 2020
Henrik Brude and Mari Skjærpe

Contents

Abstract i

Sammendrag iii

Preface v

Table of Contents xi

List of Tables xiii

List of Figures xvi

Nomenclature xvii

Subscripts xix

Abbreviations xix

1 Introduction 1

1.1 Background 1

1.2 Objective 1

1.3 Outline 1

2 Multiphase flow in porous media 3

2.1 Reservoir fluid properties 3

2.1.1 Fluid compressibility 4

2.1.2 Reservoir fluid pressure 4

2.1.3 Gas condensate field 5

2.2 Reservoir rock properties 5

2.2.1 Porosity 6

2.2.2 Rock compressibility 6

2.2.3 Fluid saturation 6

2.2.4 Permeability 7

2.2.5 Relative permeability 7

2.2.6 Surface tension and wettability 9

2.2.7 Capillary pressure 10

2.3 Skin factor 11

2.4 Conservation equations for flow in porous media 11
2.5 Ideal reservoir model 12

3 Multiphase flow in wells and pipelines **15**
3.1 Flow regimes 15
3.2 Conservation laws 16
3.2.1 Mass balance 16
3.2.2 Momentum balance 17
3.2.3 Energy balance 17
3.3 Closure relations 18
3.4 Flow assurance 19
3.4.1 Liquid accumulation 19
3.4.2 Low liquid loading flows 19
3.4.3 Three-phase pressure drop effect 20

4 Multiphase flow simulation **21**
4.1 OLGA 21
4.1.1 Numerical model 21
4.1.2 Stratified flow models 22
4.2 ROCX 22
4.2.1 Numerical model 23
4.3 Coupling between OLGA and ROCX 23
4.4 Errors in numerical modeling 24

5 Field development **25**
5.1 Drilling 25
5.1.1 Drilling fluid 25
5.1.2 Mud cake formation 26
5.2 Completion 27
5.2.1 Completion fluid 27
5.3 Well cleanup 27
5.4 Pipeline pre-commissioning 28
5.4.1 Flooding, cleaning, gauging and pressure testing 28
5.4.2 Dewatering and drying 29
5.4.3 Pig velocity control 30

6 **Subsea fields** **31**

6.1 Similar fields 31

6.2 Tanzania Block 2 32

6.2.1 Technical challenges 33

6.2.2 Pre-commissioning options 34

7 **Simulation** **37**

7.1 Simulation case 37

7.2 Model verification 38

7.2.1 Near-wellbore radius 38

7.2.2 Number of grid blocks in the ROCX model 39

7.2.3 Number of grid blocks in the OLGA model 40

7.3 Sensitivity studies on reservoir parameters 40

7.4 Simulation execution 41

7.5 ROCX model 42

7.6 OLGA model 44

8 **Results** **49**

8.1 Near-wellbore radius 49

8.2 Grid sensitivity study 51

8.2.1 Pressure drop sensitivity across the glass plug 51

8.2.2 Vertical gridding in ROCX 52

8.2.3 Radial gridding in ROCX 52

8.2.4 Angular gridding in ROCX 54

8.2.5 Gridding in OLGA 54

8.3 Sensitivity studies on reservoir parameters 55

8.3.1 Relative permeability curves 55

8.3.2 Capillary pressure curves 57

8.3.3 Determination of skin factor 59

8.3.4 Sensitivity study on mud density, skin factor and damaged zone length . . 60

8.4 Tuning of PID controller 62

8.5 Well suspension 63

8.6 Well cleanup, dewatering and early production 64

9 **Discussion** **67**

9.1 Near-wellbore radius 67
9.2 Grid sensitivity study 68
9.2.1 Pressure drop effect across the glass plug 68
9.2.2 Vertical gridding in ROCX 69
9.2.3 Radial gridding in ROCX 69
9.2.4 Angular gridding in ROCX 70
9.2.5 Gridding in OLGA 70
9.3 Sensitivity studies on reservoir parameters 70
9.3.1 Relative permeability curves 71
9.3.2 Capillary pressure curves 71
9.3.3 Determination of skin factor 71
9.3.4 Sensitivity study on mud density, skin factor and damaged zone length . . 72
9.4 Tuning of PID controller 72
9.5 Well suspension 73
9.6 Well cleanup, dewatering and early production 73

10 Conclusion **75**

11 Recommendations for further work **75**

References **77**

Appendix **i**

A OLGA models **i**

A.1 Stabilization model i
A.2 Simplified dynamic model i
A.3 Simplified dynamic model for ny=8 i
A.4 Simplified suspension model i
A.5 Complete suspension model and early production model i
A.6 Well cleanup and dewatering model ii

B ROCX models **ii**

B.1 Model with ny=8 ii
B.2 Final model ii

C Near-wellbore radius **iii**

D Grid sensitivity study **iii**

D.1 Vertical gridding in ROCX iii

D.2 Radial gridding in ROCX iv

D.3 Angular gridding in ROCX iv

D.4 Gridding in OLGA v

E Tuning of PID controller **v**

F Well suspension **vi**

G Well cleanup, dewatering and early production **vii**

List of Tables

6.1 Dewatering and well cleanup options for Block 2 (ref. Equinor) 34

7.1 Fluid properties at 420 bar and 81 °C 38

7.2 Overview of OLGA models 42

7.3 Reservoir properties for a zone in Zafarani 43

7.4 Material properties 45

7.5 Heat transfer coefficients at pipe boundaries 45

7.6 Mud and brine properties at standard conditions 46

8.1 Skin factors with corresponding mud cake thicknesses- and permeabilities 60

8.2 Skin factors with corresponding mud cake thicknesses- and permeabilities 61

8.3 Masses of drilling- and completion fluids injected into the reservoir during suspension and well kickoff 65

8.4 Filtrate backflow from the reservoir during dewatering and early production . . . 66

9.1 Results summary 67

List of Figures

2.1 Phase diagram for different reservoir types [1] 3

2.2 Pressure profile with depth for gas, oil and water respectively [1] 5

2.3 Typical relative permeability curves for a) oil wet- and a water-wet rock, respectively, and b) gas and oil 8

2.4 Water droplet submerged in oil on a rock surface 9

2.5 Effect of interfacial curvature: (a) internal pressure of droplet and (b) capillary pressure and capillary rise 10

2.6 Variables in Hawkins' equation (2.19) 11

2.7 Pressure profiles plotted in semi-log scale for a) unsteady-state, b) pseudosteady-state and c) steady-state flow, respectively 13

3.1 Horizontal multiphase flow regime map [6] 15

3.2 Control volume two fluid model [7] 16

3.3 Pipe wall layers and boundary temperatures 18

3.4 Multiple holdup region for low liquid loading flows [11] 20

4.1 Gridding scheme for a coupled wellbore-reservoir 24

5.1 Life cycle of a petroleum field [16] 25

5.2 Overburden gradient, fracture gradient, downhole mud weight and pore pressure gradient [18] 26

6.1 Field layout for Zafarani and Lavani [31] 32

6.2 a) Typical u_{sl} and local water cut along pipeline at 100% flow [14] and b) solutions of holdup equation for increasing u_{sl} [11] 33

6.3 Dewatering of trunkline A combined with flooding of trunkline B 35

6.4 Dewatering of trunkline B utilizing production gas from trunkline A as driving force 35

7.1 Starting point for Block 2 37

7.2 Numerical grid block indices 44

7.3 a) Zafarani well and infield flowline profile and b) complete flow path and ambient temperature profile on Tanzania Block 2 45

7.4 Pipe design 46

7.5 Illustration of the PVT files implemented in the model 47

8.1 Pressure distribution for an infinite acting reservoir 49

8.2 Position of the pressure front for a) $\Delta P = 0.2$ bar and b) an infinite acting reservoir 49

8.3 Pressure distribution for a reservoir of 2000 m radius modeled as (a) a closed tank (b) with pressure support at the outer boundary 50

8.4 Pressure distribution after a) 2 days and b) 52 weeks, and c) production rate for infinite acting reservoir and a 2000 m reservoir modeled as closed tank and with pressure support 50

8.5 Total mass flow above perforation for a) underpressure, b) overpressure and c) small pressure drops across the glass plug, respectively 51

8.6 a) Water content in the well and b) total mass flow above perforation during drainage for different number of grid blocks in z-direction 52

8.7 Water content in the well for a) uniform grid and b) logarithmic grid for different number of grid blocks in radial direction 53

8.8 Total mass flow above perforation during a), b) drainage and c) during kickoff for different number of grid blocks in z-direction 53

8.9 a) Water content in the well and b) total mass flow above perforation during production for different gridding in angular direction 54

8.10 a) Water content in the well and b) total mass flow above perforation during drainage for different gridding in OLGA 54

8.11 a) Relative permeability curves, b) water content in the well and b) total mass flow above perforation for different Corey exponents 55

8.12 Water content in the well and total mass flow above perforation for different values of K_{rwoc} 56

8.13 a) Water content in the well for different values of maximum capillary pressure and b), c) shape of the capillary pressure curves P_{cow} and P_{cgo}, respectively . . . 57

8.14 a) Water content in the well for different capillary pressure curvatures for oil and water, shown in b) 58

8.15 a) Water content in the well for straight line and curved capillary pressure curve for gas and oil, shown in b) 58

8.16 Water content in the well with and without capillary pressure 58

8.17 Steady-state production rate as a function of skin factor and mud cake thickness 59

8.18 Simulated relation between skin factor and thickness of a low permeable region plotted together with Hawkins' equation 59

8.19 Water content in the well for different a) mud densities, b) skin factors and c) damaged zone lengths 60

8.20 Water content in the well during a) well cleanup and b) dewatering of trunkline, and c) total mass flow rate above the perforation zone for different remaining mud cake thicknesses 61

8.21 a) Flow rate recorded by the transmitter and b) output from the PID controller for different amplification factors 62

8.22 a) Flow rate recorded by the transmitter and b) output from the PID controller for different integral constants 62

8.23 a) Pig velocity with and without controller and b) water mass ahead of pig with and without controller 63

8.24 Pressure drop across the wellhead for a) different suspension periods and b) 7 days of suspension 63

8.25 Drainage of drilling- and completion fluids in the well during the suspension period 64

8.26 Filtrate saturation in the 7 cells closest to the wellbore during the suspension period 64

8.27 Mass of mud and brine in the well (included infield flowline) and trunkline during a) first 2.5 hour of dewatering b) first 30 days of early production 64

8.28 a) Drilling- and completion fluid front propagating through the infield flowline and b) initial mud distribution in the trunkline after dewatering and mud displacement during early production 65

8.29 a) Accumulated filtrate backflow over each near-well source and b) total accumulated filtrate backflow over all three near-well sources 65

8.30 Filtrate saturation in the 7 cells closest to the wellbore during dewatering and early production 66

8.31 Remaining filtrate content in the reservoir during dewatering and well cleanup . . 66

A.1 Stabilization model used in sensitivity studies i

A.2 Simplified dynamic model used in sensitivity studies i

A.3 Simplified dynamic model used to assess a gridding with ny=8 i

A.4 Simplified suspension model used in sensitivity studies i

A.5 Suspension model for the actual simulation case i

A.6 Combined well cleanup and dewatering model with PI controller ii

B.1 Model used to assess a gridding with ny=8 ii

B.2 Final model obtained from grid sensitivity studies ii

C.1 Position of the pressure front for a) $\Delta P = 0.01$ and b) $\Delta P = 1E-7$ iii

D.1 a) Water content in the well and b), c) total mass flow above perforation during drainage for different number of grid blocks in z-direction iii

D.2 a) Water content in the well and b) total mass flow over the near-well source located at the bottom of the perforation zone iv

D.3 Total mass flow above perforation during the drainage for different number of grid blocks in angular direction iv

D.4 Water content in the well for different number of grid blocks in angular direction iv

D.5 Comparison of original flowline profile and simplified flowline profile v

E.1 a) Flow rate recorded by transmitter and b) output from PID controller for different integral constants v

E.2 Pig velocity with and without controller v

F.1 7 days well suspension vi

F.2 Holdup and flow regime ID (1=stratified, 2=Annular, 3=slug, 4=Bubble) in the well during 7 days of well suspension vi

F.3 Distance from the well boundary to each cell midpoint for the 7 cells closest to the well vii

F.4 Gas and liquid mass flow rate over the near-well sources vii

G.1 a) Initial and after b) 2 min, c) 20 min, d) 10 hours, e) 26 hours and f) 36 hours vii

Nomenclature

α	Phase fraction
ϵ	Roughness
η	Hydraulic diffusivity
γ	Rate of mass transfer between phases
μ	Dynamic viscosity
ρ	Density
σ	Surface tension
τ	Shear stress
τ_d	Derivative time constant
τ_i	Integral time constant
θ	Contact angle
θ	Pipe inclination
$\underline{\nu}^D$	Darcy velocity
A	Cross-sectional area
a	Sensitivity coefficient
B	Fluid formation factor
b	Sensitivity coefficient
C	Phase distribution effects
c_f	Fluid compressibility
c_r	Rock compressibility
c_t	Total compressibility
D_h	Hydraulic diameter
E_i	Exponential integral
f	Friction factor
g	Specific gravity
H	Enthalpy
h	Depth
h	Specific enthalpy
h_s	Heat transfer coefficient for surface, s
k	Permeability
K_c	Amplification factor
k_r	Relative permeability
k_s	Permeability of damaged zone
k_T	Thermal conductivity
L	Length
m	Mass transfer
n	Corey exponent
n	Number of moles of gas
P	Pressure
P_c	Capillary pressure
P_c	Characteristic pressure
P_p	Pseudopressure
P_s	Skin pressure
Q	Heat source term
q	Heat transfer
q	Volumetric flow rate
R	Droplet radius
R	Gas constant
r	Mean pore radius
r_{inv}	Radius of investigation
r_s	Radius of damaged zone
r_w	Radius of wellbore
S	Saturation
s	Cross-sectional contact length
s	Skin factor
S_c	Critical saturation
T	Temperature
t	Time
U	Internal energy
u	Specific internal energy
u	Velocity
u_0	Local slip effects
u_{sg}	Superficial gas velocity
u_{sl}	Superficial liquid velocity
V	Volume
V_ϕ	Pore volume
Z	Gas compressibility factor
z	Reservoir thickness

Subscripts

0	Initial condition	**o**	Oil phase
c	Capillary	**r**	Relative
c	Critical	**r**	Rock
f	Fluid	**s**	Damaged zone
g	Gas phase	**s**	Solid
i	Interface	**s**	Surface
i	Spatial index	**T**	Isothermal condition
k	Phase	**w**	Wall
l	Liquid phase	**w**	Water
m	Mixture	**w**	Wellbore

Abbreviations

DST	Drill stem test
GT	Total mass flow
IMPES	Implicit pressure explicit saturation
IPR	Inflow performance relationship
LNG	Liquefied natural gas
MAOP	Maximum allowable operating pressure
MEG	Mono ethylene glycol
PI	Productivity index
PID	Proportional-integral-derivative
PLEM	Pipeline end manifold
PV	Process variable
PVT	Pressure-volume-temperature
SP	Set point
TPR	Tubing performance relationship
TVD	Total variation diminishing
TVD	True vertical depth
TVDSS	True vertical depth subsea
VFP	Vertical flow performance
WATC	Water content in branch

1 Introduction

1.1 Background

Having drained most of the easily extracted reservoirs, a large number of the remaining oil and gas field discoveries are located in challenging deepwater environments. In order to meet the ever increasing global energy demand, these unconventional hydrocarbon reservoirs are becoming an important resource. With the ongoing trend to deepwater field development, attention has been turned to subsea development. Consequently, transport of unprocessed multiphase fluid through long-distance multiphase pipelines from remote facilities in deepwater environments has increased - introducing new possibilities as well as challenges.

Operational improvements aiming at economic savings and reduced environmental impacts are highly emphasized in the oil and gas industry. Cleanup of offshore wells is associated with a relatively high environmental impact, in addition to being a costly operation, as it requires presence of a rig or vessel. Thus, one initiative aiming at the aforementioned improvements is to perform well cleanup to the production facilities onshore instead of to an offshore rig, which will both economize rig days and reduce the environmental impact, due to reduced flaring. Cleanup to shore has already been carried out successfully at the Snøhvit field at the Norwegian Continental Shelf.

1.2 Objective

The aim of this thesis is to investigate the contingencies of well cleanup to shore, combined with dewatering of the trunkline for a gas-condensate field on Block 2 offshore Tanzania. Initial well conditions inhibit an efficient startup and well unloading, thus, gravity-driven mud drainage to the near-wellbore zone during well suspension is investigated as a possible solution. Furthermore, emphasis is made on the flushing of mud filtrate in the near-wellbore zone during early production. Of great interest is the period of time the mud will affect the production.

Utilizing a coupled wellbore-reservoir model, constituting an OLGA and a ROCX model, multiphase flow simulations are performed. A comprehensive model verification is conducted, including grid sensitivity studies and sensitivity on reservoir- and fluid parameters to assess their effect on the well drainage and reservoir flushing. The motivation behind this thesis is to support planning and decision making for the cleanup operation to be carried out on Block 2.

1.3 Outline

Chapter 2 and 3 highlights the principles of multiphase flow in porous media and in pipelines, respectively. Furthermore, the fundamental equations as prerequisites for simulating multiphase flows in porous media and pipelines are presented. Chapter 4 introduces multiphase flow simulation, with emphasis on the simulators utilized in this thesis. In Chapter 5, some important operations conducted in the field development phase are introduced. Technical challenges and the development concept to be implemented on Block 2, are presented in Chapter 6, along with parallels to fields utilizing similar concept solutions. Moreover, several startup procedures on Block 2 are suggested and discussed. Chapter 7 aims at providing an overview of the case to be simulated, the simulation steps executed and the simulation models. Chapter 8 presents the simulation results, and in Chapter 9 and Chapter 10, the results are evaluated and discussed and a conclusion is presented. Finally, remarks for improvements and recommendations for further work are presented in Chapter 11.

2 Multiphase flow in porous media

Petroleum reservoirs contain hydrocarbon mixtures that exhibit multiphase behavior with varying pressures and temperatures. Multiphase flow refers to the simultaneous flow of materials with multiple thermodynamic phases and occurs in many natural phenomena as well as within various industries. In oil and gas production, it is crucial to account for the effects of multiphase flow of oil, gas, and formation water. As this thesis is based on a gas condensate field, primarily two-phase flow of gas and liquid is considered hereafter. This chapter aims at providing a theoretical basis as a prerequisite for simulating multiphase flow in porous media. To understand the flow behavior in porous media, knowledge of the reservoir fluid- and rock properties along with the interactions between the reservoir rock and the reservoir fluid are essential, which will be introduced in the following sections. Furthermore, the equations governing multiphase flow in porous media are presented.

2.1 Reservoir fluid properties

The multiphase behavior of hydrocarbon fluids, along with the reservoir rock properties, yields different types of hydrocarbon reservoirs. The classification of a hydrocarbon reservoir depends on the composition of the mixture, the initial pressure and temperature in the reservoir, and the pressure and temperature at the surface facilities. In order to classify the different reservoir types and describe the phase behavior of the reservoir fluid, a pressure-temperature diagram of the multicomponent system is valuable, see Figure 2.1.

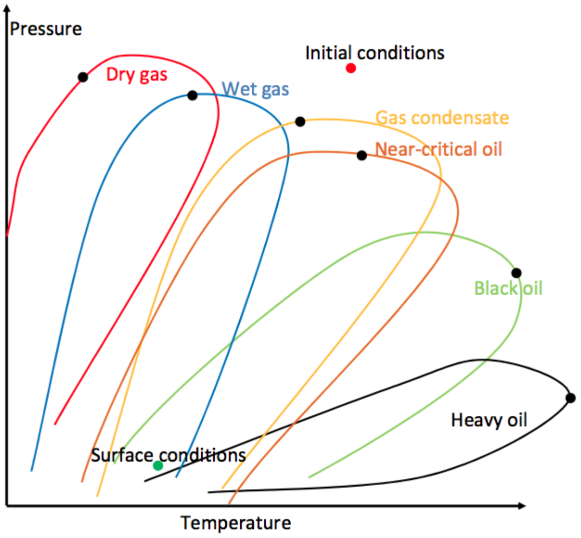

Figure 2.1: Phase diagram for different reservoir types [1]

Each curve in Figure 2.1 represents the phase diagram of each field type. The region enclosed by each curve is the two-phase envelope where gas and liquid coexist in equilibrium. The boundary of the two-phase region defines the bubble point- and dew point curves. The bubble point line is defined as the line separating the liquid phase region from the two-phase region, and the dew point line marks the transition between the gas phase region and the two-phase region. The bubble point is defined as the point of temperature at which the first bubble of gas is formed in the liquid at a given pressure, and the dew point marks the point of temperature at which the first drop of liquid is formed at a fixed pressure. The bubble point- and dew point lines meet at the critical point, marked with black dots in Figure 2.1 for the different field types. The critical point represents the state of pressure and temperature of the mixture, referred to as the critical- pressure and temperature, respectively, where all properties of the gas and liquid phases are equal.

As seen from Figure 2.1, the phase envelopes differ in size and shape for different reservoir fluids. The reservoir fluid type is classified according to the position of the initial pressure- and temperature of the mixture relative to the phase envelope. If the reservoir temperature is less than the critical temperature of the reservoir fluid, the reservoir is classified as an oil reservoir. If the reservoir temperature is greater than the critical temperature of the hydrocarbon fluid, on the other hand, the reservoir is considered a gas reservoir. As each fluid type requires a unique approach to develop and produce the reservoir, it is important to identify the fluid type early in the life of a reservoir. The primary method of determining the fluid type is through laboratory analysis [2].

2.1.1 Fluid compressibility

The compressibility of a fluid, c_f, is defined as the relative change in fluid volume as a response to a pressure change [2]. The density formulation of the definition of compressibility follows from the assumption of constant mass before and after a pressure change, see equation 2.2.

$$c_f = \frac{1}{V}\frac{\partial V}{\partial P} = \frac{1}{\rho}\frac{\partial \rho}{\partial P} \tag{2.1}$$

$$\frac{\partial}{\partial P}(\rho V) = \rho\frac{\partial V}{\partial P} + V\frac{\partial \rho}{\partial P} = \rho c_f V + V\frac{\partial \rho}{\partial P} = 0 \tag{2.2}$$

where V denotes the fluid volume, P is the pressure and ρ is the fluid density. Gas reservoirs have strong compressibility, as the physical parameters of the gas change with pressure.

2.1.2 Reservoir fluid pressure

Reservoir pressure is an important factor affecting the phase behavior and properties of a reservoir fluid. The fluid pressure at a specific location in the reservoir is estimated by the weight of fluid in the pore space above that location, given from

$$P = P_0 + \rho g h \tag{2.3}$$

where P_0 is a reference pressure, often atmospheric pressure and h is the depth. Hence, the fluid pressure increases with depth. As Figure 2.2 indicates, the oil and gas pressures decreases less rapidly with depth compared to the water pressure, simply due to the density differences between the fluids.

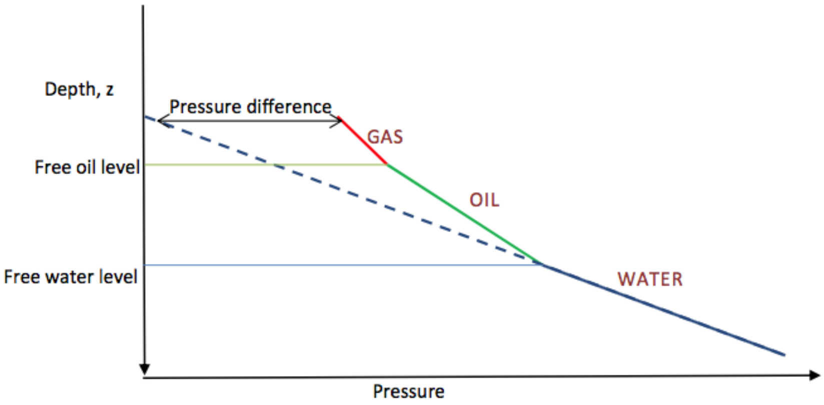

Figure 2.2: Pressure profile with depth for gas, oil and water respectively [1]

This deviation in pressure between the hydrocarbon-bearing zones and the surrounding water-saturated rock at the same depth can cause potential hazard during drilling. As the borehole is gradually filled with water during drilling, the higher pressure hydrocarbons could flow into the hole and cause blow out. Consequently, drilling fluid is injected into the borehole to ensure a higher pressure in the well than the formation [1]. Drilling fluids will be further described in Chapter 5.1.1.

2.1.3 Gas condensate field

A gas condensate field contains an amount of heavy hydrocarbons which condenses as droplet within the reservoir as the reservoir pressure drops below its dew point. The preferred method of production in a gas field is to drop the pressure as low as feasible to allow the gas to expand, whereas in an oil field gas will form for pressures below the bubble point. Due to viscosity differences between the oil and the gas, the less viscous gas will flow preferentially to the oil and thus leave behind the oil. Hence, for an oil field, it is preferable to maintain the pressure above the bubble point. However, a gas condensate field is more complex. If the pressure drops below the dew point - oil is formed and left behind in the reservoir during production. Consequently, the oil occupies the pore space in the reservoir and thus puts a constrain to the gas flow. The preferred method of production for a gas condensate field is either to maintain the pressure, as in an oil field, or to drop the pressure until the single-phase region is reached, thereby produce as in a gas field [1].

2.2 Reservoir rock properties

Reservoir rock properties are classified as static and dynamic. The former classification refers to properties shaped by the depositional environment in ancient times. Of interest are porosity, permeability, and rock compressibility. The latter classification refers to the rock properties influenced by interactions between the reservoir rock and the reservoir fluid. These include relative permeability, fluid saturation, capillary pressure, and wettability. Both the static- and dynamic rock properties are described in detail in the following sections [3].

2.2.1 Porosity

Porosity, ϕ, describes a reservoir rock's fluid storage capacity, defined as the ratio of pore volume to bulk volume of the rock. The bulk volume is comprised of pore volume and the grain volume. As not all pores are interconnected in the rock, a distinction is made between absolute- and effective porosity. Total porosity includes all void space, both interconnected- and isolated pore volume. In contrast, effective porosity includes only interconnected pore volume which contributes to fluid flow in the reservoir. Typical porosity values for a conventional reservoir rock range between 2-25%, and increases with increasing grain size. High porosity indicates a large storage capacity of reservoir fluids, in addition to good flow characteristics [3].

2.2.2 Rock compressibility

Rock compressibility, c_r, is a measure of the rate of change of pore volume as the reservoir pressure changes, expressed as

$$c_r = -\frac{1}{V_\phi}\left(\frac{\delta V_\phi}{\delta P}\right)_T \tag{2.4}$$

where V_ϕ denotes the pore volume of the rock and P is the pressure exerted on the formation. Subscript T denotes isothermal conditions. As explained in Section 2.1.2, the reservoir pressure declines during production resulting in a reduction of pore volume due to formation compressibility. The resulting reduction in porosity is given from

$$\phi = \phi_0 exp[c_r(P - P_0)] \tag{2.5}$$

where subscript 0 denotes initial properties.

2.2.3 Fluid saturation

The saturation of a fluid, S_k, is defined as the fraction of a pore occupied by the given fluid, k, including oil, gas, and water. The saturation of all fluids present in a pore adds up to 1, by definition

$$\sum_k S_k = 1 \tag{2.6}$$

Fluid saturation strongly affects the ability of a fluid to flow through the porous media, and detailed knowledge of the fluid saturation is highly valuable. For the oil phase to flow in the porous media, the oil saturation must exceed the critical oil saturation, S_{oc}, below which oil is immobile. As the reservoir pressure declines below the bubble-point, gas starts evolving from the oil phase. However, for this gas phase to begin to move, its saturation must exceed the critical gas saturation, S_{gc}. The same applies to the water phase, where S_{wc} denotes the critical water saturation, below which the water phase remains immobile due to capillary forces [3].

2.2.4 Permeability

Permeability, k, refers to a porous rock's ability to transmit fluids through its pores, which can be described as either absolute-, effective- or relative permeability. Absolute permeability reflects the permeability when a single fluid is present in the rock, whereas the effective permeability is the rock's ability to transfer a particular fluid with the presence of other immiscible fluids in the reservoir [4]. The absolute permeability assumes 100% saturation of the single fluid in the rock, while effective permeability depends highly on the fluid saturation as multiple fluids are present in the rock. The definition of permeability can be supported by an empirical correlation, Darcy's law, expressed as

$$q = \frac{KA\Delta h}{L} \tag{2.7}$$

where q is the volumetric flow rate, K is the hydraulic conductivity of the porous medium, A is the cross-sectional flow area and L is the length of the relevant flow interval. Equation 2.7 can be modified to account for the effect of viscosity, given from

$$u = \frac{q}{A} = -\left(\frac{k}{\mu}\right)\left(\frac{\delta P}{\delta L}\right) \tag{2.8}$$

where u is the fluid velocity, k is the average permeability in the rock, μ is the fluid viscosity. Darcy's law is considered as the foundation of fluid flow in porous media, valid upon the assumption that the rock is 100% saturated with incompressible and laminar flowing single-phase fluid. To allow the Darcy law to be applied to multiphase systems, the relative permeability needs to be considered.

2.2.5 Relative permeability

Relative permeability, k_r, is the ratio of effective permeability of a fluid at a given saturation to the absolute permeability of the fluid at total saturation. The relative permeability at a location in the reservoir may change during production as the fluid saturation changes [3]. Figure 2.3 below illustrates this nonlinear relationship, showing typical relative permeability curves as a function of water saturation for an oil-wet- and a water-wet rock, respectively.

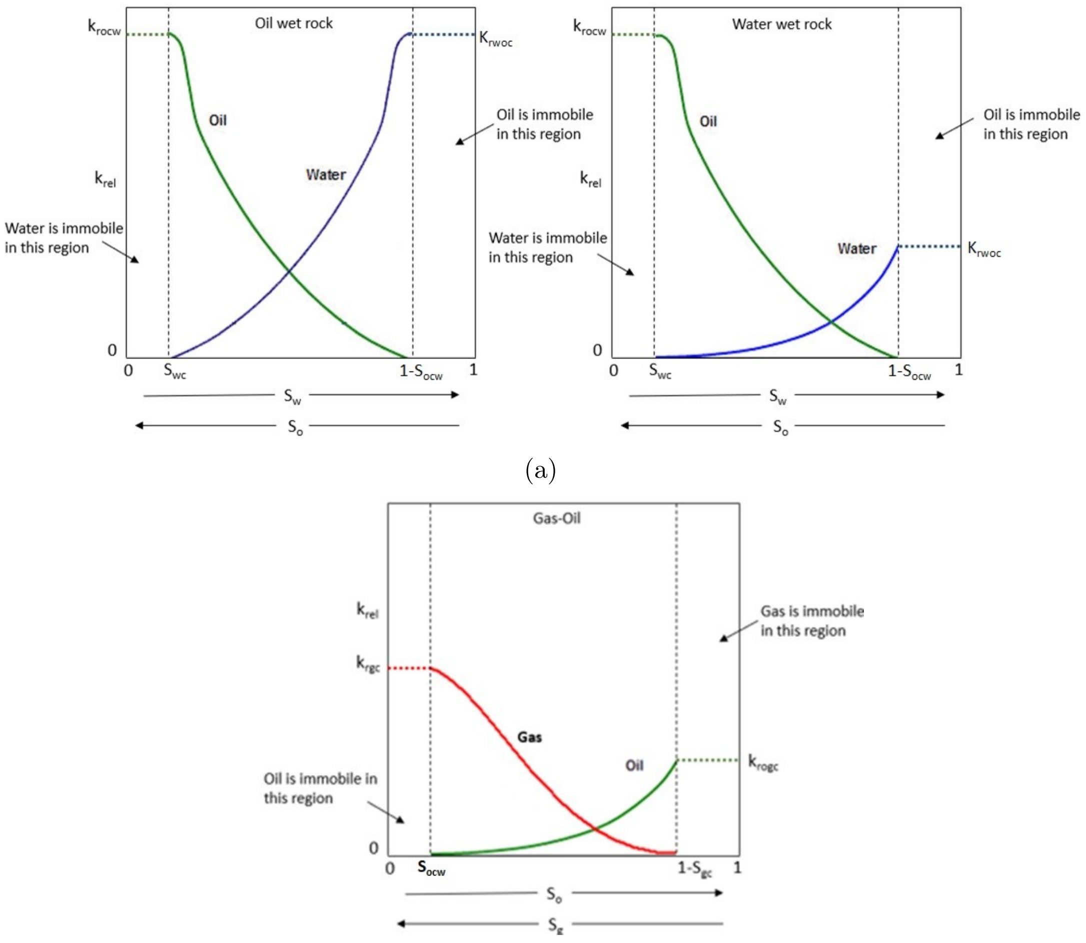

(a)

(b)

Figure 2.3: Typical relative permeability curves for a) oil wet- and a water-wet rock, respectively, and b) gas and oil

The values of relative permeability range between 0 and 1. In order to obtain these relative permeability curves based on fluid saturation, various empirical correlations are available. To mention one, the Corey correlation is frequently used in simulation software. The Corey correlations for water, oil in an water-oil system, oil in a oil-gas system, and gas, respectively, reads

$$k_{rw} = k_{rwoc}\left(\frac{S_w - S_{wc}}{1 - S_{wc}}\right)^{n_w} \tag{2.9}$$

$$k_{row} = k_{rocw}\left(\frac{1 - S_{ocw} - S_w}{1 - S_{ocw} - S_{wc}}\right)^{n_{ow}} \tag{2.10}$$

$$k_{rog} = k_{rocw}\left(\frac{1 - S_{ocg} - S_w - S_g}{1 - S_{ocg} - S_{wc}}\right)^{n_{og}} \tag{2.11}$$

$$k_{rg} = k_{rgco}\left(\frac{S_g - S_{gc}}{1 - S_{ocg} - S_{wc} - S_{gc}}\right)^{n_g} \tag{2.12}$$

where S_{ocw} and S_{ocg} are the critical oil saturations to water and gas, respectively, below which oil is immobile. k_{rwoc} is the end point relative permeability of water at S_w=1-S_{ocw}=0 and S_g=0, and k_{rgco} is the end point relative permeability of gas at S_w=S_{wc} and S_o=S_{ocg}. k_{rocw} is the end point relative permeability of oil at S_w=S_{wc} and S_g=0. n_w, n_{ow}, n_{og} and n_g are the Corey exponents.

Figure 2.3 shows the effect of wettability of the rock on the shape of the relative permeability curves. In an oil-wet rock, the wetting tendency is greater in comparison to in a water-wet rock, resulting in a relatively low irreducible water saturation. Similarly, the residual oil saturation is greater in oil-wet rocks compared to water-wet rocks. Hence, the relative permeability curve of an oil-wet rock is shifted to the left of the water-wet curve.

2.2.6 Surface tension and wettability

As a reservoir usually has several fluids present in the pores, it is crucial to consider interfacial forces between to immiscible fluids in contact, as well as surface tension between a fluid and a surface. Interfacial- and surface tension are caused by the increased molecular interaction energy at the interface, and are thereby defined as the excess energy per area. Figure 2.4 shows the acting forces at the intersection point of the oil, water, and the rock surface.

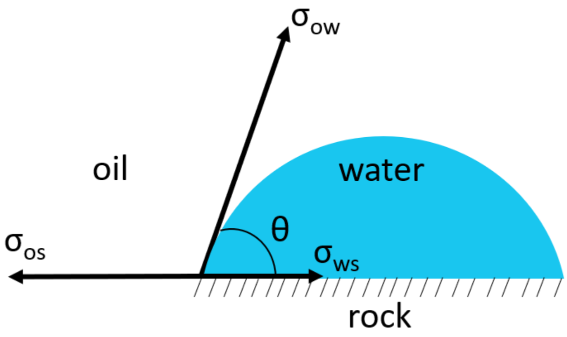

Figure 2.4: Water droplet submerged in oil on a rock surface

The contact angle, θ, is used to quantify the wettability of the rock. The wettability of the rock measures the tendency of a immiscible fluid to spread in contact with other fluids present at the rock surface, and depends on the rock minerals and the fluid composition in the rock. A force balance in the horizontal direction yields the following correlation for the contact angle

$$\cos\theta = \frac{\sigma_{os} - \sigma_{ws}}{\sigma_{ow}} \tag{2.13}$$

where σ_{ij} is the tension between surface i and j, and subscript o, w, s denotes oil, water, and solid, respectively. If the surface tension of the oil exceeds the surface tension of the water, i.e $\theta < 90°$, the water droplet will spread out on the surface and the rock is characterized as water-wet, illustrated in Figure 2.4. Most conventional gas reservoir tends to be water-wet. In the opposite case, for $\theta > 90°$, the rock is classified as oil-wet [3]. Figure 2.3 above shows the strong relationship between wettability and relative permeability.

2.2.7 Capillary pressure

Capillary pressure, P_c, denotes the pressure difference between two immiscible fluids in a porous media, based on the interfacial- and surface tensions between the fluids and rocks. The capillary pressure can be explained by the same physics as seen in a droplet. Consider a water droplet surrounded by oil, as illustrated in Figure 2.5 a).

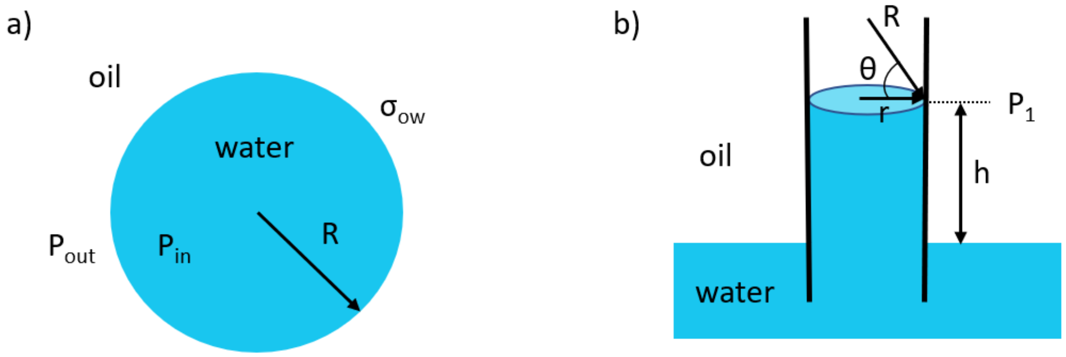

Figure 2.5: Effect of interfacial curvature: (a) internal pressure of droplet and (b) capillary pressure and capillary rise

By balancing the differential work of shrinkage and change in interfacial energy for a droplet, the equilibrium size of the droplet can be determined, given from

$$\Delta P dV = \sigma_{ow} dA \tag{2.14}$$

where V is the droplet volume and A is the interfacial area. Assuming spherical shape of the droplet, equation (2.14) simplifies to

$$\Delta P = P_{in} - P_{out} = \frac{2\sigma_{ow}}{R} \tag{2.15}$$

where R is the droplet radius. By applying basic trigonometry, illustrated in Figure 2.5 b), equation (2.15) can be rewritten to

$$P_c = \Delta P = \frac{2\sigma_{ow}\cos\theta}{r} \tag{2.16}$$

where P_c is the capillary pressure, i.e the pressure difference below and above the curved interface. The pressure is always greater inside the curvature than outside, hence the oil pressure is greater than the water pressure for $\theta < 90°$. r is the mean pore radius, often estimated as the square root of the absolute permeability divided by the porosity

$$r = \sqrt{\frac{k}{\phi}} \tag{2.17}$$

2.3 Skin factor

Formation damage in a well can be measured using a skin factor, s. The skin factor is a dimensionless pressure drop caused by a restriction of the flow in the near-wellbore region. Van Everdingen & Hurst expressed the skin pressure drop, ΔP_s, as

$$s = \left(\frac{kz}{141.2q\mu B} \right) \Delta P_s \tag{2.18}$$

where B is the fluid formation volume factor and z is the reservoir thickness. Hawkins introduced a modification to van Everdingen & Hurst

$$s = \left[\frac{k}{k_s} - 1 \right] ln \frac{r_s}{r_w} \tag{2.19}$$

where k_s is the average permeability of the damaged zone, and r_s and r_w are the radii of the damaged zone and wellbore, respectively. The variables are illustrated in Figure 2.6. A large skin pressure drop yields large well damage. However, it is more convenient to express the well condition terms of the skin factor. A positive skin factor represents a damaged well, whereas a negative skin factor represents a stimulated well.

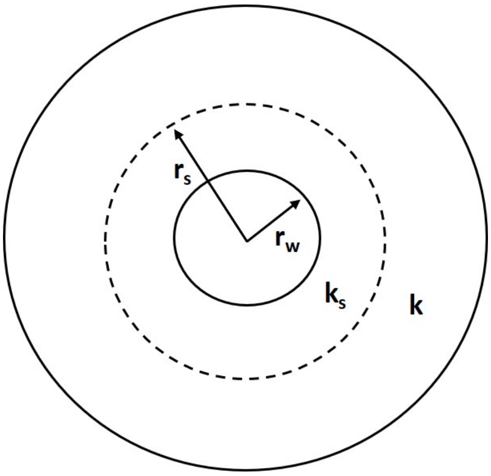

Figure 2.6: Variables in Hawkins' equation (2.19)

2.4 Conservation equations for flow in porous media

The flow in porous media is governed by conservation equations of mass, momentum, and energy for each phase, written as

$$\frac{\partial(\rho_k \phi S_k)}{\partial t} = -\frac{\partial(\rho_k u_k)}{\partial x} + m_k + \gamma_{k<-g} \qquad k = o, w \tag{2.20}$$

$$\frac{\partial(\rho_g \phi S_g)}{\partial t} = -\frac{\partial(\rho_g u_g)}{\partial x} + m_g + \gamma_{g<-o} + \gamma_{g<-w} \tag{2.21}$$

where m denotes the mass transfer and γ is the rate of mass transfer between the phases. Substituting Darcy's law into the above mass conservation equations, yields

$$\frac{\partial(\rho_k \phi S_k)}{\partial t} + \frac{\partial(\rho_k \underline{\nu_k}^D)}{\partial x} = m_k + \gamma_{k<-g} \qquad\qquad k = o, w \tag{2.22}$$

$$\frac{\partial(\rho_g \phi S_g)}{\partial t} + \frac{\partial(\rho_g \underline{\nu_g}^D)}{\partial x} = m_g + \gamma_{g<-o} + \gamma_{g<-w} \tag{2.23}$$

where $\underline{\nu_k}^D$ denotes the Darcy phase velocities given by

$$\underline{\nu_k}^D = -k\frac{k_{rk}}{\mu_k}\left(\frac{\partial P_k}{\partial x} - \rho_k \underline{g}\right) \tag{2.24}$$

To allow the Darcy law to be applied to multiphase systems, the set of equations must be supplemented with a capillary pressure-saturation relationship, accounting for interfacial forces, given from

$$P_k - P_w = P_c(S_w) \tag{2.25}$$

The conservation equation for temperature reads

$$\begin{split}\frac{\partial(\rho_w \phi S_w u_w + \rho_o \phi S_o u_o + \rho_g \phi S_g u_g + (1-\phi)\rho_s \phi u_s)}{\partial t} + \frac{\partial(\rho_w h_w \underline{u}_w + \rho_o h_o \underline{u}_o + \rho_g h_g \underline{u}_g)}{\partial x} \\ + \frac{\partial\left(k_T \frac{\partial T}{\partial x}\right)}{\partial x} = Q\end{split} \tag{2.26}$$

where u is the specific internal energy, h is the specific enthalpy, k_T is the thermal conductivity, T is the temperature and Q denotes heat source term. To distinguish phase velocity from specific internal energy in this equation, velocity is denoted by $\underline{u}$.

2.5 Ideal reservoir model

By combining the conservation equation of mass and Darcy´s law, the diffusivity equation for 1D radial flow can be obtained. For a vertical well in an isotropic cylindrical reservoir, the diffusivity equation can be written as follows in cylindrical coordinates

$$\eta \frac{1}{r}\frac{\partial}{\partial r}(r\frac{\partial P}{\partial r}) = \frac{\partial P}{\partial t} \tag{2.27}$$

where the hydraulic diffusivity, η, is given from

$$\eta = \frac{k}{\mu \phi c_t} \tag{2.28}$$

where the total compressibility, c_t, is defined as

$$c_t = c_r + c_f \tag{2.29}$$

Equation (2.27) applies under the assumptions of isothermal flow, where permeability, viscosity, and compressibility are independent of pressure. In addition, the equation is only valid for low compressible fluids, thus, not for gas reservoirs. The solution of the diffusivity equation exists for three different flow regimes; unsteady-state, pseudo steady-state, or steady-state flow. Analytical solutions for each flow regime can be obtained for a constant flow rate in the wellbore with no flow or constant pressure outer boundary condition, see Figure 2.7.

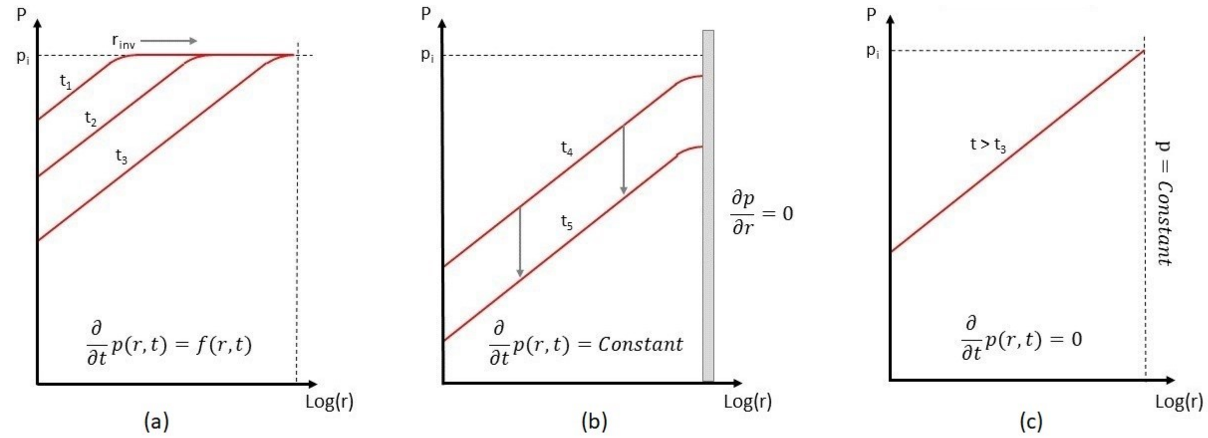

Figure 2.7: Pressure profiles plotted in semi-log scale for a) unsteady-state, b) pseudosteady-state and c) steady-state flow, respectively

Unsteady-state or transient flow occurs whenever the pressure change with respect to time, $\partial p/\partial t$, depends on both time and position in the reservoir. In a drainage scenario, transient flow occurs while the reservoir is said to be infinite acting, which is before the pressure is affected by the outer boundaries. For a well producing at a constant rate in an infinite acting reservoir, the diffusivity equation has the following analytical solution

$$P = P_0 - \frac{1}{2} P_c E_1 \left(\frac{1}{4\eta} \frac{r^2}{t}\right) \tag{2.30}$$

where P_c is the characteristic pressure and $E_i(\xi)$ is the exponential integral given by

$$P_c = \frac{Q\mu}{2\pi k h} \tag{2.31}$$

$$E_i(\xi) = -\int_{-\xi}^{\infty} \frac{e^{-t}}{t} dt \tag{2.32}$$

In such a case, a pressure disturbance will propagate in the reservoir. The radius of investigation, r_{inv}, is defined as the radius where $\xi = 1$. Applied to equation (2.30) yields the two following correlations

$$r_{inv} = \sqrt{4\eta t} \tag{2.33}$$

$$\Delta P = P_0 - P = \frac{1}{2} P_c E_1(1) \tag{2.34}$$

The radius of investigation is obtained when the pressure has decreased with ΔP from the initial pressure, P_0. Notice that the radius of investigation increases with $\sqrt{t}$, hence the propagation speed decrease with $\frac{1}{\sqrt{t}}$.

If the reservoir is modeled as a closed tank, the pressure disturbance will at some point reach the outer reservoir wall, thus, the reservoir is no longer infinite acting and the flow is characterized as pseudo steady-state flow. In such case, the change of pressure with respect to time is constant at any position in the reservoir. The reservoir pressure declines as the closed tank is drained. If the reservoir is modeled with pressure support at the outer boundary, however, the flow will become steady-state. Hence, the same amount of fluid enters and exits the reservoir, and there are no pressure variations with respect to time. Both the closed tank and the pressure support solution is illustrated in Figure 2.7.

As mentioned above, the analytical solutions are only valid for slightly compressible fluids, but can be extended to describe compressible fluids by introducing the real gas law and the pseudo-pressure transformation given by

$$PV = ZnRT \tag{2.35}$$

$$P_p(P) = 2 \int_{P_0}^{P} \frac{P}{\mu Z} dP \tag{2.36}$$

where Z is the gas compressibility factor, n is the number of moles of gas, R is the gas constant, and P_p is the pseudopressure. The transformation results in an equation on the same form as the diffusivity equation, equation (2.27), but with pressure replaced by pseudopressure [5].

3 Multiphase flow in wells and pipelines

With the ongoing trend to deepwater field development, the use of multiphase pipelines from remote facilities in deepwater environments has increased. The physics of multiphase flow in wells and pipelines, and the governing equations, differ from the flow in porous media, as introduced in the previous chapter. Hence, this chapter focuses on understanding the fundamental concepts as prerequisites for simulating multiphase flow in wells and pipelines, including the governing equations, limited to a two-phase scenario of gas phase and liquid phase.

3.1 Flow regimes

For multiphase flow in pipes, different flow regimes tend to occur dependent on pipe geometry, the fluid properties, and the flowrates of the fluids present. A flow regime describes the cross-sectional phase distribution of the multiphase mixture in the pipe. Prediction of flow regime is an important aspect of multiphase flow simulations, as different flow regimes affect parameters differently. A general distinction in two-phase flow is between separated flows and disperse flows. The former referring to continuous phases separated by well-defined interfaces, subdivided into stratified and annular flow, while the latter consists of droplets or bubbles distributed within a continuous phase, subdivided into bubble/droplet flow and slug flow.

The cross-sectional phase distributions are determined from the balance of stratifying and mixing forces: viscous, inertia, gravity, and surface forces. In horizontal pipelines at low flowrates, gravity forces dominate, causing the two phases to separate with the heavier fluid gravitating to the bottom. With increasing gas flow rate the mixing forces tend to gradually dominate, causing the interface in stratified flow to become wavy. Further increase in gas flow rate could turn into annular flow. If the liquid flow also increases, slug flow can occur. Flow regimes encountered in vertical pipelines are somewhat simpler, as gravity cause symmetry in the flow. The flow regimes are however much similar to those in horizontal flow, only the cross-sectional distribution differs [6]. Figure 3.1 shows a typical horizontal flow regime map, attempting to connect the observations made of the state of the two-phase flow to the pipe geometry, physical properties, and the flowrates of the fluids. It is important to stress that these flow regime maps are just suggestive, not exact.

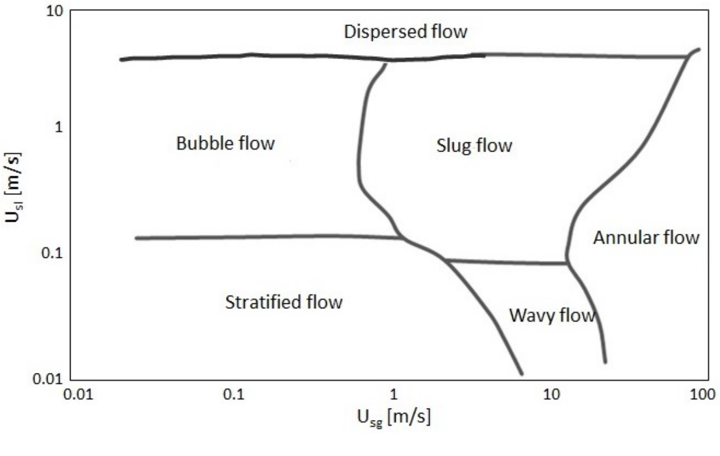

Figure 3.1: Horizontal multiphase flow regime map [6]

u_{sg} and u_{sl}, comprising the axes in the flow regime map, denotes the superficial gas and liquid velocities, respectively, representing the velocity the relevant phase would have if it was flowing alone in the pipe.

3.2 Conservation laws

Independent of flow regime, the simulation of multiphase flow is based upon the same mathematical models: conservation of mass-, momentum- and energy. The respective closure relations, on the other hand, depends highly on the flow regime. The following subsections present the one-dimensional conservation laws for two-phase flow of gas and liquid, as these are relevant for this thesis. Furthermore, the respective closure relations are presented. Figure 3.2 below illustrates characteristic parameters used in the conservation equations.

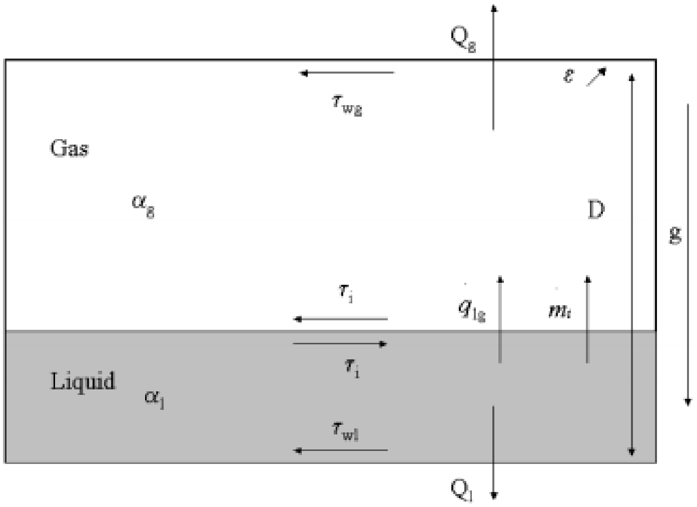

Figure 3.2: Control volume two fluid model [7]

3.2.1 Mass balance

The conservation equations of mass for the gas and liquid phase reads

$$\frac{\partial(\alpha_g \rho_g A)}{\partial t} + \frac{\partial(\alpha_g \rho_g u_g A)}{\partial x} = m_{lg} - m_{gw} \tag{3.1}$$

$$\frac{\partial(\alpha_l \rho_l A)}{\partial t} + \frac{\partial(\alpha_l \rho_l u_l A)}{\partial x} = -m_{lg} - m_{gw} \tag{3.2}$$

where α denotes the cross-sectional phase fraction defined as $\alpha_k = \frac{A_k}{A}$, m_{lg} is the mass transfer between the two phases, and m_{kw} is the mass transfer between phase k and other sources. The direction of mass transfer, which is assumed to be from the liquid phase to the mass phase, causes the negative sign in front of the mass transfer in the liquid.

3.2.2 Momentum balance

The conservation equations of momentum reads

$$\frac{\partial(\alpha_g \rho_g u_g A)}{\partial t} + \frac{\partial(\alpha_g \rho_g u_g^2 A)}{\partial x} = -\alpha_g A \frac{\partial P_g}{\partial x} - \alpha_g \rho_g A g sin\theta - s_{gw}\tau_{gw} - s_i \tau_i + m_{lg} u_i - m_{gw} u_g \quad (3.3)$$

$$\frac{\partial(\alpha_l \rho_l u_l A)}{\partial t} + \frac{\partial(\alpha_l \rho_l u_l^2 A)}{\partial x} = -\alpha_l A \frac{\partial P_l}{\partial x} - \alpha_l \rho_l A g sin\theta - s_{lw}\tau_{lw} + s_i \tau_i - m_{lg} u_i - m_{lw} u_l \quad (3.4)$$

where θ is the pipe inclination, s is the cross-sectional contact length between the phases or the wall and τ_{kw} and τ_i is the wall shear stress and interfacial shear stress, respectively.

3.2.3 Energy balance

The conservation equations for energy reads

$$\frac{\partial \alpha_g \rho_g A(U_g + \frac{u_g^2}{2} g h_g)}{\partial t} + \frac{\partial \alpha_g \rho_g u_g A(H_g + \frac{u_g^2}{2} + g h_g)}{\partial x} = q_{lg} + Q_g \quad (3.5)$$

$$\frac{\partial \alpha_l \rho_l A(U_l + \frac{u_l^2}{2} g h_l)}{\partial t} + \frac{\partial \alpha_l \rho_l u_l A(H_l + \frac{u_l^2}{2} + g h_l)}{\partial x} = -q_{lg} + Q_l \quad (3.6)$$

where U denotes internal energy, H is enthalpy, q_{lg} is the heat transfer between the two phases, and Q_k is the heat transfer to phase k from the surroundings through the pipe wall.

In a circular pipe with concentric wall layers, the heat transfer can be assumed radial symmetric. Thermal conduction and heat storage are considered for the solid wall layers in between the outer and inner walls. The boundary conditions for the inner and outer walls are given by

$$Q_i = h_{iw}(T_f - T_{iw}) \quad (3.7)$$

$$Q_{amb} = h_{amb}(T_{ow} - T_{amb}) \quad (3.8)$$

where Q_i is the heat flow from the fluid to the inner wall and Q_{amb} is the heat flow outer wall to the surroundings. T_f, T_{iw}, T_{ow} and T_{amb} are the fluid, inner wall, outer wall and ambient temperatures, respectively, as illustrated in Figure 3.3. h_{iw} and h_{ow} denotes the inner and outer wall heat transfer coefficients, respectively [8].

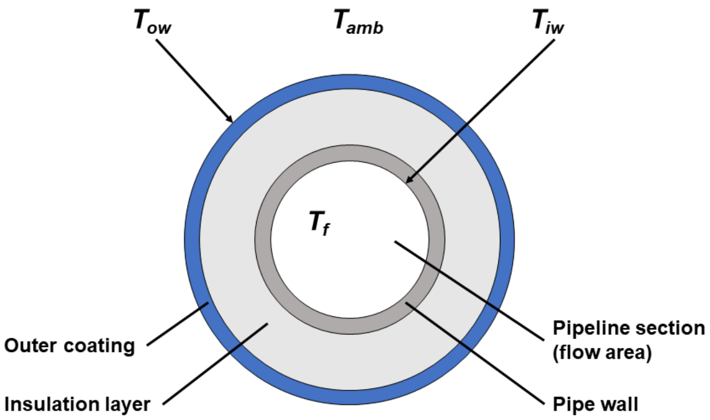

Figure 3.3: Pipe wall layers and boundary temperatures

3.3 Closure relations

The set of conservation equations are closed by a set of closure relations describing wall- and interfacial friction, droplet deposition, and the entrainment of bubble and droplet. The closure requirements depend on the flow model. In a two-fluid model, where each region has its separate momentum equation, the closure requirements are mainly the wall- and interfacial shear stresses, given from

$$\tau_{kw} = f_{kw}\rho_k \frac{u_k^2}{8} \tag{3.9}$$

$$\tau_i = f_i \rho_k \frac{(u_k - u_i)^2}{8} \tag{3.10}$$

where f_{kw} and f_i denotes the Darcy friction factors on the wall and interface, respectively. The friction factor between a fluid and the wall can be calculated using the Håland correlation, which is an explicit approximation of the implicit Colebrook equation. The Håland correlation reads

$$\frac{1}{2\sqrt{f_w}} = -1.8 \cdot \log_{10}\left[\frac{6.9}{Re} + \left(\frac{\epsilon}{3.7 \cdot D_h}\right)^{1.11}\right] \tag{3.11}$$

where Re is the Reynolds number, ϵ is the roughness of the pipe and D_h is the hydraulic diameter. For gas, the D_h is calculated for a closed channel, whereas for liquid it is calculated for open channel flow. Several correlations for the interfacial friction factor are proposed, among these are the empirical Wallis correlation (1969) given below.

$$\left(\frac{f_i}{f_{kw}}\right) = [1 + 75(1 - \alpha_k)] \tag{3.12}$$

In a mixture model, denoting the case where a mixture momentum equation is applied, a mixture shear stress and a slip relation are required. The mixture shear stress is calculated as for the wall frictions, but with mixture properties. A slip relation is typically an algebraic relation relating phase velocities, e.g as equation (3.13).

$$u_g = Cu_m + u_0 \tag{3.13}$$

where C denotes the phase distribution effects, u_m the mixture velocity, and u_0 represents the local slip effects [9]. However, in order to complete the set of equations, more closure relations are required, including relations for heat capacity, thermal conductivity, and entropy.

3.4 Flow assurance

The term flow assurance refers to the successful and economical flow of hydrocarbons from reservoir to end-user. Assessment of flow assurance challenges requires knowledge of flow variables such as pressure, temperature, velocities, composition, and flow regime [9]. Multiphase flow simulators, aiming to predict these local flow conditions, are crucial in flow assurance management. In this section flow assurance challenges related to subsea gas condensate pipelines will be described.

3.4.1 Liquid accumulation

In gas condensate pipelines, the liquid flow rate often increases along the pipeline, due to water and condensate dropout as temperature decreases along the pipeline [10]. If the gas rate is sufficiently low, liquid accumulation may occur in upward inclined sections of the pipe. This is in general undesirable, as increased liquid content in the pipeline can cause surge waves or severe slugging dependent on the flow rate. These phenomenons can cause serious liquid managing challenges and damage at the receiving facility.

3.4.2 Low liquid loading flows

In fully developed steady-state two-phase stratified flow, the holdup is given by the balance of friction and gravity forces [11]. This balance is governed by the holdup equation (level gradient term is neglected)

$$0 = \alpha_l s_g \tau_g - \alpha_g s_l \tau_l + s_i \tau_i - \alpha_l \alpha_g (\rho_l - \rho_g) g A sin\theta \tag{3.14}$$

Solving equation (3.14) for flows in upwards inclined pipes with low superficial liquid velocity, u_{sl}, will yield multiple holdup solutions, see Figure 3.4. Barnea et al. investigated the different solutions and found the lower solution to be stable, and the other two to be unstable [12]. When the gas rate is decreased below a certain value, referred to as the critical superficial gas velocity or the accumulation point, the holdup will jump discontinuously from a low holdup value to a higher. Flows experiencing such holdup jump in upwardly inclined pipes are referred to as low liquid loading flows [11]. The area of the multiple holdup region increases with decreasing

u_{sl}, as illustrated in Figure 6.2 b). Gas condensate pipelines with sufficiently low u_{sl} and steep inclinations are likely to operate in the low liquid loading domain, hence accurate prediction of the onset point for liquid accumulation is crucial [10].

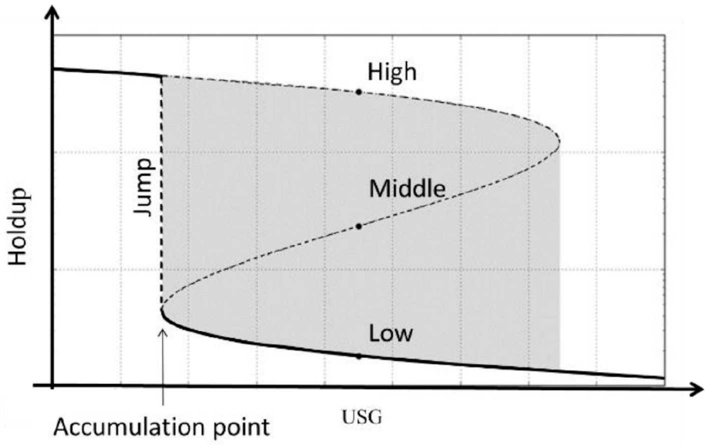

Figure 3.4: Multiple holdup region for low liquid loading flows [11]

3.4.3 Three-phase pressure drop effect

Recently, a three-phase pressure drop effect has been discovered for flows in the low liquid loading domain [13]. Frictional pressure drop has shown to be reasonably higher, 20-30%, for three-phase flows than for two-phase flows at equal flow conditions. This pressure effect is highly sensitive to the water cut, and frictional pressure drop has shown to increase with increasing water cut. Multiphase flow simulators have shown poor or no ability to capture this effect. Limited experimental data for three-phase low liquid loading flows at high rates exists. However, new experiments have been conducted and improvements in flow simulators have been made to account for this effect [14]. These uncertainties in flow models are especially important in projects related to very long subsea gas condensate pipelines, as pressure drop miscalculations scale with pipeline length and such pipelines often have a narrow operational envelope.

4 Multiphase flow simulation

Transient multiphase flow simulation provides valuable insight into the physics describing flow from the reservoir to processing facilities. In a computational model, the aforementioned conservation equations are discretized and solved numerically on a grid for given boundary- and initial conditions. In order to simulate a well cleanup, the model needs to consider multiphase flow in two different environments: porous media and wellbore.

Conventional dynamic well models use steady-state inflow performance relationship (IPR) to describe the inflow from the reservoir, ignoring the transients in the near-wellbore area. Furthermore, conventional reservoir models use steady-state vertical flow performance (VFP) curves to describe the flow in the tubing, tubing performance relationship (TPR), ignoring the wellbore dynamics. Hence, these approaches do not account for dynamic interactions between wellbore and reservoir, which in some cases are of great importance. In order to bridge this modeling gap, a wellbore model can be coupled to a near-wellbore reservoir model. In this thesis, transient integrated wellbore-reservoir simulations are performed utilizing coupling between OLGA and ROCX. The purpose of this chapter is to yield an understanding of the numerical aspects of each simulator, as well as the numerical coupling.

4.1 OLGA

OLGA is a one-dimensional dynamic multiphase flow simulator, comprising advanced fluid mechanical- and numerical models. With its ability to simulate multiphase flow in networks of wells, pipelines, and process equipment, OLGA accounts for the production system from bottomhole to receiving facilities. The following sections introduce the fundamentals of OLGA, based on material from the OLGA user manual [8].

4.1.1 Numerical model

OLGA is a three-fluid model, described by five different velocity fields; three continuous layers (gas, water, and oil) and two droplet fields (oil and water droplets in gas). The velocity fields are described by three momentum equations and two slip relations. Furthermore, three conservation equations for mass and one mixture energy equation are applied, based on the assumption of thermal equilibrium between the phases at a specific location. Altogether, this sums up to seven conservation equations, in addition to one equation of state. This system of equations is closed by applying fluid properties and boundary- and initial conditions. The least computational demanding method of describing fluid properties in OLGA includes using a PVT lookup table. By interpolating in the property tables, a fluid with related phase properties for specific pressures and temperatures is obtained at each segment along the flowline [8]. All pressure- and temperature-dependent properties are given as points in a pressure-temperature diagram, as introduced in Chapter 2.1.

Each flowpath in the production system is divided into user-defined sections, or control volumes, constituting the spatial grid in the numerical model. OLGA utilizes a staggered grid, with the flow variables, such as velocity, flux, and mass flow, defined at the cell boundaries, whilst the volume variables, such as pressure, temperature, and volume fractions, are defined in the center of the cell. The main spatial discretization scheme is a 1.order implicit upwind scheme. The implicit upwind method is the most robust and thus the preferred scheme in most cases. Unfortunately, the scheme suffers from numerical diffusion. To bridge this modeling gap, a 2.order Total Variation Diminishing (TVD) scheme with less numerical diffusion can be applied to the mass equations, being the preferred choice in cases where it is important to track sharp holdup fronts. However, the TVD scheme suffers from instabilities. The discretization in time is implemented as a semi-implicit time integration, based on user-defined time-step values.

By linearizing and discretizing the conservation equations in space and time, OLGA runs a sequential solution scheme. Pressure and temperature are de-coupled, meaning current pressure is calculated using the previous temperature. The sequential scheme will cause a numerical error in local fluid volume, which will be corrected over a period of time [8].

4.1.2 Stratified flow models

OLGA utilizes two models for stratified flow; the standard model and the HD model. The models are distinguished by the number of dimensions taken into account. Standard OLGA is based on one-dimensional bulk velocity and closure relations for the friction factors, computed as described in Section 3.3. The OLGA HD model utilizes two-dimensional velocity distributions in the cross-sectional area to determine the frictions and momentum flux terms. Mechanistic models based on the log law are used for the wall and interfacial frictions. The two-dimensional velocity field can be integrated over the pipe cross-section and combined with the one-dimensional conservation equations, resulting in a three-dimensional flow representation [11]. The model requires closure relations for the turbulence parameters, K, representing scaled eddy viscosities. By manipulating these closure relations, it is possible to tune the wall- and interfacial frictions to fit experimental data [8]. The OLGA HD model has proven to be strong concerning simulation of liquid accumulation, thus chosen as the preferred flow model for the Tanzania project [14].

4.2 ROCX

ROCX is a three-dimensional dynamic near-wellbore reservoir simulator, capable of simulating three-phase Newtonian Darcy flow in porous media. By solving the flow equations in three dimensions, saturation-, pressure- and temperature distributions in space for each time step in addition to the flow rate of each phase are obtained. ROCX can either be run standalone or with coupling to OLGA. To obtain a suitable condition in the reservoir, prior to initiating a coupled simulation, a standalone simulation can be useful. When coupled to OLGA, the coupled simulation is fully controlled by OLGA, as ROCX is considered as a plug-in.

4.2.1 Numerical model

The reservoir volume of interest is divided into user-defined grid cells, either as a rectangular grid or a radial grid. Each grid cell is assigned reservoir fluid- and rock properties. The fluid properties can be implemented using a PVT table or using the Black Oil approach. The reservoir rock properties can either be specified with values for each numerical block, or they can be set constant in each layer or even in the whole near-wellbore zone. The relative permeabilities are defined together with their corresponding phase saturations, and can be implemented manually or using the Corey correlation.

Finally, initial- and boundary conditions should be given to fulfill the numerical model. The initial conditions can either be manually implemented, by specifying saturations for each phase, pressure for one of the phases and temperature, or automatic, by computing an initial state based on hydrostatic equilibrium in the reservoir. ROCX can also be initialized with data from a restart record from a previous run. Boundary conditions can be specified either at the well boundary or at the outer reservoir boundary, formulated as Dirichlet- or Neumann boundary conditions. If a Dirichlet boundary condition is given, the boundary is prescribed by a pressure, along with temperature and saturation. If the Neumann boundary condition-type is given, no flow across the boundary is assumed, constituting a closed boundary system. The latter is implemented in ROCX simply by not specifying any boundary condition.

ROCX is governed by three conservation equations in a porous medium; water, oil, and gas. Furthermore, it is governed by a volume balance for the phases, two mass balances for the flash terms, two pressure relations, and one mixture energy equation. By discretizing the aforementioned equations in time and space on the numerical grid, ROXC runs an implicit modification of the Implicit Pressure Explicit Saturation (IMPES) scheme, yielding numerical stability and robustness. ROCX solves one pressure equation, one energy equation, and three mass equations at each time step. Furthermore, the volume saturations are calculated based on the solved masses. As a result, pressure-, temperature- and saturation distribution at each time step are obtained [15].

4.3 Coupling between OLGA and ROCX

In order to couple the ROCX model to an OLGA model, a near-well source for each perforation is defined at the wellbore side in OLGA and linked to a well boundary grid block as a boundary condition on the reservoir side in ROCX specifying temperature, pressure and, saturations for each perforation. Figure 4.1 illustrates the gridding scheme for a coupled wellbore-reservoir model.

Numerically, the coupling is implemented in an implicit modification of the IMPES scheme, constituting a robust and numerical stable model. An implicit coupling simultaneously solves the wellbore and reservoir models [15]. In short, OLGA provides ROCX with pressure boundary conditions, and ROCX calculates the mass flow rate of each phase at the interface along with the fluid temperature and transmits back to OLGA. The implicit numerical coupling algorithm is outlined in three steps below.

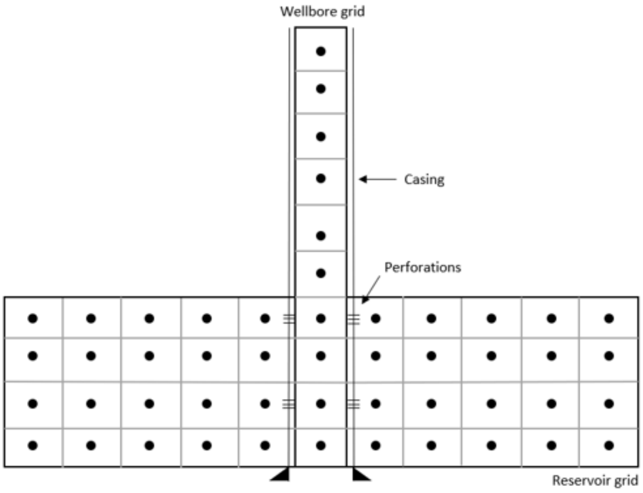

Figure 4.1: Gridding scheme for a coupled wellbore-reservoir

In the first step of the iteration algorithm, ROCX calculates, on request from OLGA, sensitivity coefficients for the production rate based on the wellbore pressure, defined from

$$m_{k,i}^{n+1} = a_{k,i}^{n} P_{k,i}^{n+1} + b_{k,i}^{n} \tag{4.1}$$

where a and b are the sensitivity coefficients. Subscript k denotes phase, including oil, gas, and water, while subscript i refers to cell number. Superscript n denotes the time step.

In the second step, OLGA uses equation (4.1) as a boundary condition and solves the complete flow network in the wellbore at time step $n+1$ and transmits $P_{k,i}^{n+1}$ and $m_{k,i}^{n+1}$ back to ROCX. In the final step, ROCX calculates new sensitivity coefficients based on the computed values from OLGA, given from

$$a_{k,i}^{n} = \frac{dm_{k,i}^{n}}{dP_{k,i}^{n}} \qquad\qquad b_{k,i}^{n} = m_{k,i}^{n} - a_{k,i}^{n} P_{k,i}^{n} \tag{4.2}$$

4.4 Errors in numerical modeling

It is important to be aware of the potential errors when conducting numerical simulations. As the simulation models are based on certain assumptions, the model itself is usually approximate. Furthermore, the replacement of differential equations to difference equations introduces truncation error, as the exact solution of the difference equations differs from the solution of the differential equations. In some schemes, the discretization error is second-order proportional to grid block size, thus the smaller grid block size the smaller error. Grid sensitivity will be highly emphasized in this thesis, in which numerical errors are used as a vital decision basis, the most important being numerical dispersion. Numerical dispersion is a numerical error caused by grid block approximation that occurs in simulations of rapid holdup changes and results in a smearing of holdup fronts. Reducing the number of grid blocks will reduce the effect of numerical dispersion.

5 Field development

After discovery of a petroleum field, exploration and production activities take place throughout the lifetime of the field, as shown in Figure 5.1. If the evaluation of the petroleum reserves indicates a commercially viable field, preparations prior to initiation of production begins. The development phase includes drilling and completion of production wells, design and construction of pipelines, processing systems, and receiving facilities. This chapter highlights some operations executed prior to production.

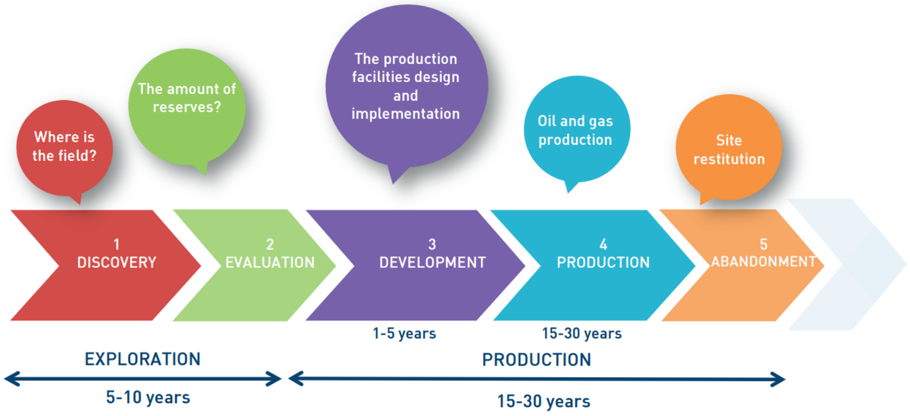
Where is the field?
The amount of reserves?
The production facilities design and implementation
Oil and gas production
Site restitution
1 DISCOVERY
2 EVALUATION
3 DEVELOPMENT
4 PRODUCTION
5 ABANDONMENT
1-5 years
15-30 years
EXPLORATION
5-10 years
PRODUCTION
15-30 years

Figure 5.1: Life cycle of a petroleum field [16]

5.1 Drilling

In order to extract the discovered petroleum resources in a field, a well needs to be drilled. The most common method is rotary drilling, which requires a rotary table at the surface to rotate the assembly. After drilling operations, or even during drilling, drill stem tests (DST) are often conducted in order to determine formation potential and thus evaluate the commercial viability of the zone of interest. Dependent on the DST, the well either becomes a producer or it will be plugged and abandoned. In the former case, completion operations must be undertaken.

5.1.1 Drilling fluid

During drilling operations, drilling fluid, often referred to as drilling mud, is injected into the wellbore to facilitate the drilling process. Drilling fluids serve a range of purposes including suspending drill cuttings, controlling pressure to prevent formation fluids to enter the wellbore, keep the drill bit cool and clean, and maintain wellbore stability [17].

Different types of drilling fluids are available, classified into water-based, oil-based, or synthetic-based. Water-based mud is most commonly used and is considered cheaper than oil-based- and synthetic-based fluids. The drilling fluid selection for a specific well is driven by factors such as technical performance, cost, and environmental impact. Selecting an appropriate mud weight requires knowledge of the pore pressure gradient and the fracture pressure gradient. Fracture pressure is the pressure required to fracture the formation causing mud losses to the formation, whereas the pore pressure is simply the pressure in the pores in the formation. The mud weight must be less than the fracture pressure to avoid mud losses to the formation, while it must be greater than the pore pressure to avoid formation fluids to flow into the well on the other hand. Hence, the fracture pressure gradient constitutes the upper bound of the mud weight, whereas the pore pressure gradient provides a lower limit of the mud weight, see Figure 5.2.

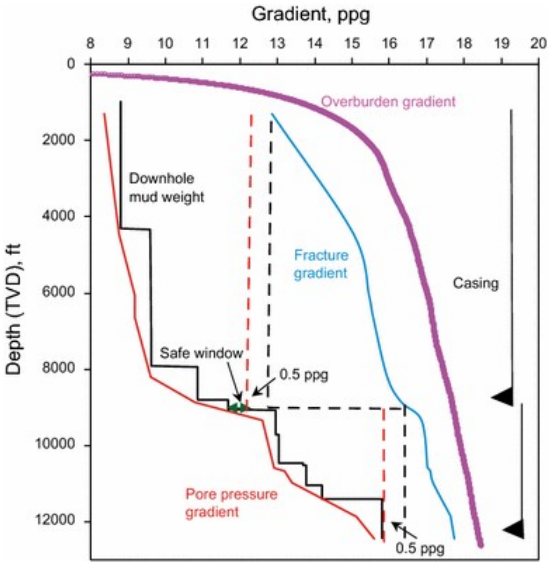

Figure 5.2: Overburden gradient, fracture gradient, downhole mud weight and pore pressure gradient [18]

5.1.2 Mud cake formation

During overbalanced drilling, the pressure of the mud column in the well exceeds the formation pore pressure, preventing the formation fluids from entering the wellbore. The overbalanced pressure forces the drilling mud through the formation where the solid particles in the mud deposits and gradually builds up a low permeability barrier, a mud cake, at the wellbore boundary. This barrier around the wellbore, skin, will cause a reduction in wellbore productivity, referred to as formation damage.

During the buildup of the mud cake, the liquid component of the drilling mud, filtrate, will invade the formation and thus displace the movable fluids in the formation, leaving an invaded zone, sometimes also referred to as skin zone. However, with the buildup of the mud cake, and thus reduction in permeability at the wellbore boundary, the filtrate influx to the formation decreases accordingly. The time evolution of the buildup of mud cake and the flow rate of filtrate invasion depends on mud properties and rock properties, including porosity, permeability, water saturation, capillary pressure, and relative permeability. If the pressure drawdown, or lift-off pressure, is sufficiently high when the well is kicked off, this external mud cake will be removed [19].

5.2 Completion

Once a well is drilled, well completion event begins. Well completion incorporates the operations needed to transform a drilled well into a producing one. The most common methods of completion includes cased hole- and open hole completions. The first step in a cased hole completion involves running a steel casing through the wellbore to the bottom of the reservoir, in order to protect the wellstream and stabilize the wellbore. Furthermore, cement slurry is pumped down into the well, permanently positioning the casing into the well. Once the casing is installed the production tubing is run inside the casing, allowing produced fluid to flow from the reservoir to the surface. However, in order to achieve production, perforating the well is required. Utilizing a perforating gun, perforation tunnels through the casing and cement are created. In an open hole completion, on the other hand, the production casing is set above the reservoir and cemented into place. The remaining part of the wellbore, however, is left uncased, leaving the reservoir zone completely exposed to the wellbore, improving the wellbore performance [17].

5.2.1 Completion fluid

In order to minimize formation damage during well completion, completion fluids are injected into the well to displace the drilling mud. The completion fluid interacts with the reservoir components in order to increase the permeability. The most widely used completion fluid is clear brine, in which there are a number of types commercially available. The fluid selection depends on three basic criteria: density requirement, required crystallization temperature for storage and chemical compatibility between the completion fluids and the formation.

Pressure control in the well is the primary requirement of the completion fluid. Hence, the completion fluid density must contribute to a sufficient hydrostatic pressure to overcome and control the formation pressure. The second selection criterion is the crystallization temperature, meaning the temperature at which the completion fluid is saturated with salt. If the completion fluid is cooled below this temperature, precipitation of salt solids will occur, introducing several rig problems. This crystallization of brine is especially important to take into account in deepwater wells with low temperatures. The third criterion in selecting completion fluid is the chemical compatibility with the formations. The main concern with incompatibility is formation damage and thus lost productivity, as a result of swelling or deflocculation of formation clays blocking the pores [20].

5.3 Well cleanup

After a well is drilled and completed, it is filled with segregated drilling- and completion fluids. Hence, cleanup operations must be conducted in order to ensure a successful removal of these drilling- and completion fluids, as well as the mud cake, prior to diverting the well to production facilities. The well cleanup operation depends highly on the interaction between the drilling fluids in the wellbore and the formation. Additionally, the cleanup operation depends largely on the weight of the initial column of drilling- and completion fluids, reservoir properties, well design and infrastructure for the tieback.

In cases with sufficient reservoir pressure, well cleanup can be achieved by simply initializing production. As the well is kicked off, the reservoir fluid enters the wellbore and starts to displace the fluids, utilizing the reservoir pressure as the driving force. In cases with limiting reservoir pressure, on the other hand, additional artificial lift such as gas lift or nitrogen injection through coiled tubing is required to achieve an efficient cleanup. Inefficient cleanup operations can result in stagnant mud or completion fluid in the lower section of the well, causing back pressure and thus significantly reduced well productivity [21].

Usually, wells drilled from existing templates or platforms can be cleaned up shortly after the well has been commissioned. For subsea wells drilled in new field developments, on the other hand, it may take months or even years before cleanup is possible. In the latter case, as well as in cases where producing drilling fluids into the pipeline can cause operational problems for receiving facilities, cleanup to the drilling rig is preferable [22]. In the present thesis, however, contingency for well cleanup to production unit instead of cleanup to drilling rig is investigated. Cleanup to rig is extremely costly, hence it is more preferable to do cleanup through the pipeline. As will be discussed in the next chapter, this cleanup procedure has been performed successfully on Snøhvit.

5.4 Pipeline pre-commissioning

Once a pipeline is installed and before it can be commissioned for production, several operations are required to ensure it meets the requirements. The first step in preparing a pipeline for production is usually to fill it with water and clean it. Thereupon, gauging and hydrotesting are conducted to verify the integrity throughout the pipeline. Finally, the pipeline must be dewatered and dried. To successfully perform these pre-commissioning tasks, several pigging operations are usually necessary. A pig is a tool that occupies the whole cross-section of a pipeline, mainly used to separate flows from each other. A row of several pigs separated by fluids or gasses is called a pig train.

5.4.1 Flooding, cleaning, gauging and pressure testing

Subsea pipelines can either be flooded from offshore or onshore. Free flooding from offshore can be achieved by opening the choke at the PLEM and let seawater flow naturally into the pipeline, while flooding from onshore normally requires pumping effort. Prior to the hydrotest, it is required that the pipeline cross-section is fully occupied by water with no gas pockets present. This can be achieved by inserting a pig train in front of the water and drive it through the pipeline. Flooding and cleaning may be performed in one operation, utilizing a pig train equipped with cleaning tools such as brushes or discs. This way, the pig can remove rust from the inner surface and transports debris from the construction phase out of the pipeline.

Once the pipeline is clean, gauging is conducted in order to prove the dimensional quality of the internal diameter and ensure no other defects are present. Gauging is usually performed using a caliper pig, with an aluminum disk machined to a diameter according to the maximum tolerated defect size. If the aluminum disk does not contain any defects, such as buckles or deformations after traveling through the pipeline, the requirements have been met [23]. Finally, the hydrotest can be carried out by pressurizing the pipeline to at least 1.25 MAOP, maximum allowable operating pressure. The pressure should retain this value for a period to verify the mechanical strength of the pipeline, the integrity of the connections and make sure no leaks are present [24].

5.4.2 Dewatering and drying

For oil pipelines, dewatering can be achieved by simply initializing production to displace the water, as small quantities of water to the first production will not cause any significant problems. The situation for gas pipelines is however not so straightforward, as the presence of water may have serious consequences in terms of flow assurance challenges. In the latter case, pigging is essential in the dewatering operation [23]. The choice of pigging direction mainly depends on two concerns; the location of the water discharge and the available driving sources for the pig train. If the seawater flooded in the pipeline is treated with chemicals to prevent corrosion, discharge in shallow waters is not preferred due to environmental reasons. In such a case, it is preferable to dewater the pipeline to shore and treat the contaminated seawater in the processing plant.

Usually, compressed air or hydrocarbon gas is used as the driving medium for the pigging operation. With air as the driving medium, the pipeline is dewatered and dried in two separate operations, by bulk dewatering and air purging respectively. Compressors located at a mobile unit or at the onshore facility will deliver compressed air to propel the pigging train through the pipeline. Afterwards, the pipeline pressure will be blend off and air will be purged through the pipeline using the same compressors. Both events contribute to dry the pipeline, as a pressure decrease will increase the water content in saturated air, and circulation of dry air will displace the water out of the pipeline by convection. In the latter case, when hydrocarbon gas is utilized as a driving source, it is supplied from the reservoir or in some cases from other fields. As no air purging operation is conducted before the hydrocarbon gas is introduced, the pig train must be designed in such a manner that no water can mix with the gas and cause flow assurance challenges.

A dewatering pig train normally consists of 6-8 pigs separated by glycol slugs at the front and dry air at the rear. The purpose of the glycol slugs is to dilute the water passing through the pigs. The water concentration decreases for every batch further back, and in the third batch the concentration is typically is less than 1%. The sweeping pigs at the rear end remove liquid leaking through the front pigs. Hydrocarbon gas sources have proven to be both time and cost-efficient, as dewatering, drying, gas filling and pressurization can be performed in one operation, with the absence of expensive mobile units or temporary installment of compressor equipment [25].

5.4.3 Pig velocity control

To ensure a successful and efficient pigging operation, the pig velocity must be maintained within reasonable limits, generally in the range 0.5-1 m/s. By controlling the flow in the pipeline, the desired pig velocity can be maintained. In a dewatering operation, pig velocity control is especially important, as liquid management at the receiving facility can be challenging. Bypass pigging is the standard operating procedure in order to reduce the pig velocity. Alternatively, a PID controller can be utilized to maintain the volume rates within specified bounds by adjusting the valve opening of the production choke. A PID controller generates its output, $u(t)$, proportionally to the error between the desired setpoint (SP) and measured process variable (PV), the integral and the derivative of the error, expressed by

$$u(t) = K_c \left[e(t) + \frac{1}{\tau_i} \int_0^t e(t)dt + \tau_d \frac{de(t)}{dt} \right] \tag{5.1}$$

where K_c denotes the amplification factor, describing how fast the system responds. A high amplification factor yields a fast response, and vice versa. Furthermore, τ_i and τ_d are the integral and derivative time constants, respectively, and $e(t)$ denotes the controller error defined as

$$e(t) = (PV(t) - SP) \tag{5.2}$$

Careful considerations must be made when tuning a PID controller. The aim of tuning is to adjust the control parameters to yield the optimum values for the desired response. The main requirement of the control response is stability and must be fulfilled for all combinations of process conditions and setpoints.

I some applications, only one or two control terms are sufficient to provide appropriate control. A P controller is beneficial to use for fast-response systems. However, the P controller suffers from offset. Adding the integral action, the resulting PI controller enables to eliminate offset. Thus, the PI controller provides a balance complexity and capability, and is consequently the most widely adopted in industrial applications. However, introducing the integral action has a negative effect on the speed of the response, thus, PI controllers are utilized in applications where fast response is not required [26]. The derivative term provides a dampening effect, by taking into account the current rate of change of the error.

6 Subsea fields

A large number of the remaining oil and gas field discoveries are located in ultra deepwater- and arctic environments, introducing new technical challenges for oil and gas field development. Over the past two decades, attention has been turned to subsea field development, as introduced in Chapter 5. The subsea-to-beach concept, to be implemented on Block 2, enables transport of unprocessed reservoir fluids in multiphase pipelines from subsea to shore processing facilities [27]. This chapter aims at presenting the technical challenges and the startup procedure performed on similar fields utilizing the subsea-to-beach concept, along with parallels to the challenges present at Block 2. Moreover, several startup procedures on Block 2 are suggested and discussed.

6.1 Similar fields

The Snøhvit project marks a milestone in subsea field development, being the first Norwegian offshore development utilizing the subsea-to-beach concept, with all subsea facilities tied-back to and remotely controlled from shore [28]. Additionally, the 145 km long pipeline transporting the production to the LNG plant at Melkøya is the world's longest pipeline transporting unprocessed flow [29]. The Snøhvit development area is located in an arctic environment in the Barents Sea at 350 meters water depth, 140-160 km from the coastline of Northern Norway.

Dewatering was performed at Snøhvit during May/June, 2007. Prior to dewatering, all infield flowlines were filled with a mixture of MEG and water, while the main pipeline was flooded with seawater. The dewatering was accomplished launching a pig train from a temporary pig launcher at the PLEM, driven by process gas from the wells, towards a permanent pig receiver at Melkøya (ref. Equinor). 10 years later, in October 2017, cleanup of the F-3H well at Snøhvit was performed to shore through the main trunkline during production. Cleanup to rig was the base case for the well, but great savings in rig time and reduced environmental impact caused a change of concept. However, field development studies predicted that the F-3H-well, initially containing large volumes of drilling- and completion fluids, was not able to unload. In order to ensure efficient well start-up and unloading at Snøhvit, well suspension was performed in order to reduce the mud volume in the well, due to drainage to the reservoir under the influence of gravity. By pressurizing the tubing with nitrogen, sufficient overbalance against the reservoir was created to shatter the glass plug between the tubing and the reservoir. Over-pressure in the tubing forced a given amount of the drilling fluid to backflow into the reservoir, and the well pressure stabilized at reservoir pressure. This reduction in liquid content in the well made well cleanup during production possible (ref. Equinor).

Ormen Lange comprises another field utilizing the subsea-to-beach concept, located in the North Sea approximately 120 km from the coastline of Norway [30]. Subsea systems are located at the seabed 850 m below sea level, tied back to the onshore production facility at Nyhamna through dual multiphase production trunklines. In contrast to the dewatering approach performed at Snøhvit, Ormen Lange utilized gas from shore to dewater the trunklines. Both trunklines were initially filled with seawater after a successful hydrotest. The pigging trains were launched from shore into pipeline A, and received onshore again after turning around in the pigging loop at the PLEM and dewater/cleaning pipeline B. Regarding the dewatering with gas from shore, the major challenge is the capacity of the gas driving source. Expansion of the gas will contribute to transport the pigs back onshore, serving a great advantage of using gas as the driving source. However, long pipelines in deepwater environments require a large amount of gas at high pressures to push the pigs from shore to subsea. The requirements were met by supplying gas from the Sleipner platform through the Langeled gas transport pipeline to Nyhamna [30].

6.2 Tanzania Block 2

In 2011, Equnior started exploration drilling activities in Block 2 offshore Lindi, southern Tanzania. 15 exploration wells have been drilled, resulting in discoveries with estimated volumes of more than 20 trillion cubic feet of gas across eight fields. Appraisal wells have been drilled in the main discoveries, Zafarani, Lavani Main, Lavani Deep, Piri and Tangawizi, confirming the volumes and properties. Figure 6.1 shows the field layout for Zafarani, Lavani Main and Lavani Deep. Following the successful discoveries in Block 2, Equinor is currently preparing for the development phase.

The gas discoveries on Block 2 are located at water depths ranging from 2200 m to 2600 m, contributing to challenging development solutions. Consequently, the development concept to be implemented comprise gas extraction through subsea wells- and dual pipelines tied to a receiving LNG plant onshore, resembling the subsea-to-beach production system implemented on Snøhvit and Ormen Lange. Via satellite jumpers, the wells are tied back to a dual header cluster manifold and further tied through dual- flowlines and trunklines to shore [31].

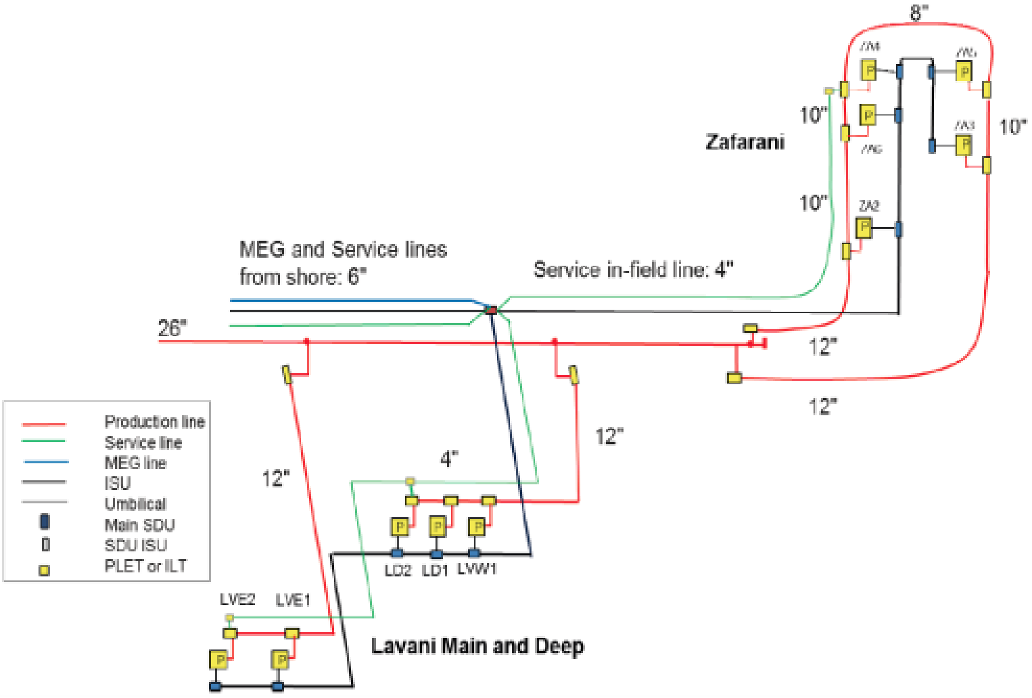
8"
10"
10"
Zafarani
10"
ZA2
MEG and Service lines
from shore: 6"
Service in-field line: 4"
26"
12"
12"
12"
12"
4"
Production line
Service line
MEG line
ISU
Umbilical
Main SDU
SDU ISU
PLET or ILT
LD2
LD1
LVW1
LVE2
LVE1
Lavani Main and Deep

Figure 6.1: Field layout for Zafarani and Lavani [31]

6.2.1 Technical challenges

The water depth, along with challenging seabed conditions with steep seabed canyons and steep inclination towards shore, contributes to flow assurance challenges. Although the large scale topography is relatively smooth, the global pipeline profile is generally steep with inclinations typically at 4 to 5 degrees. The steep escarpment towards shore bringing the pipeline to locally inclinations as high as 20 to 30 degrees. In addition, large in-field differences in water dept can cause problems in terms of significant static heads or too low MEG concentrations if liquid accumulation should occur during low flow rates.

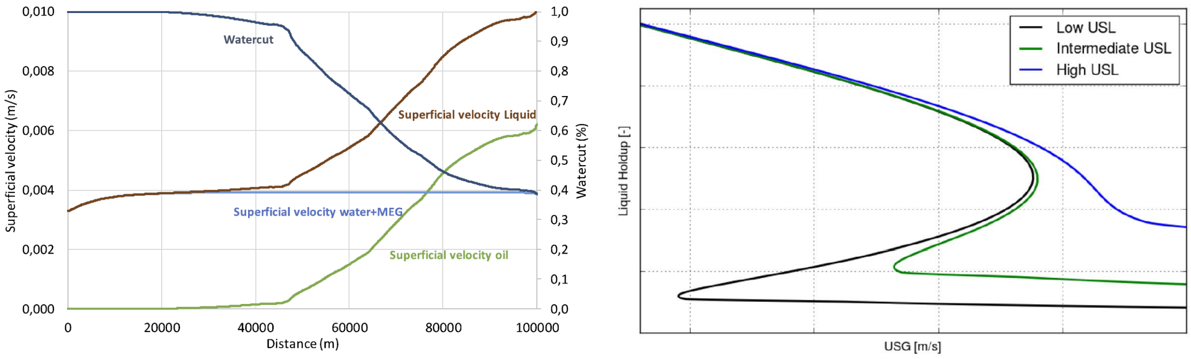

(a) (b)

Figure 6.2: a) Typical u_{sl} and local water cut along pipeline at 100% flow [14] and b) solutions of holdup equation for increasing u_{sl} [11]

Another challenge of concern is the large temperature variations in the flow from the reservoir to shore. The flow from the reservoir has a temperature of approximately 80°C, while the seabed temperature ranges from around 3°C at the deepest, before the temperature starts increasing towards shore. Depending on the pipeline configuration, the arrival temperature may be as high as 30°C [14]. High reservoir temperature yields high water saturation in the gas, resulting in high water cuts in the pipeline where the temperatures are sufficiently lower. The reservoir fluids are relatively dry with little condensate content initially. However, condensation will occur in the second half of the pipeline where pressures are low. Consequently, the water cut increases in the first half of the pipeline, while it decreases in the second half as the gas condenses, see Figure 6.2 a).

Most gas condensate fields, including Snøhvit and Ormen Lange, operate at higher superficial liquid velocities where the holdup is continuously decreasing with increasing superficial gas velocity, typically described by the blue curve in Figure 6.2 b). The reservoir fluids in the Block 2 field are dry, hence the superficial liquid velocity is low. In combination with steep inclinations, this may result in operating points where several holdup solutions exist, known as low liquid loading flow, described by the green and black curve in Figure 6.2 b). As described in Chapter 3.4, low liquid loading flows in combination with high water cuts give rise to some challenges in flow modeling associated with liquid accumulation and three-phase pressure drop effects. As the reliability of flow simulators are crucial for the development of subsea field in Tanzania, Equinor has investigated these effects in several experimental campaigns over the past years. Experiments have been conducted by SINTEF at the Multiphase Flow Laboratory in Trondheim [14].

6.2.2 Pre-commissioning options

Procedure	Alt.	Description	Pros	Cons
Dewatering	1 a)	High pressure compressed air/nitrogen at the terminal	- Independent of field and terminal start-up	- Require very large temporary equipment spreads - Very expensive
	1 b)	LNG tanker or national grid as pressure source	- Independent of field start-up - Possible synergy with terminal commissioning	- Require terminal partly commissioned to receive LNG from tanker and compressor to achieve export pressure - Expensive
	1 c)	Gas from the reservoir as pressure source	- Possible synergy with terminal commissioning - Less expensive	- Dependent on field start-up - Potential flow assurance issues due to low flowrates
Well Cleanup	2 a)	Cleanup to rig	- Well known procedure	- Higher pollution - Expensive due to many rig days
	2 b)	Cleanup through pipeline to shore	- Most environmental friendly - Less expensive	- Potensial risk of equipment damage due to mud transport

Table 6.1: Dewatering and well cleanup options for Block 2 (ref. Equinor)

There are three alternatives to obtain pressure support with high enough capacity to drive the pig train during dewatering at the Block 2 field. The first alternative, 1 a), includes temporary equipment to produce high-pressure air or nitrogen to be installed. However, this is very costly as it must be installed and removed only for this occasion. In addition, such equipment requires large installation areas. The advantage with this option is that the subsea pipeline can be pre-commissioned before the wells and LNG terminal are ready for start-up.

In Tanzania, the national gas grid stretches from Dar es Salaam in the north, along the coastline all the way to the border to Mozambique in the south. Thus, the second alternative comprises pressure support from Lindi to dewater the trunkline, in the same way as Langeled supplied gas for pre-commissioning at Ormen Lange. Alternatively, gas can be supplied from an LNG tanker. In both cases, the LNG terminal must be partly commissioned to be able to receive gas from such sources.

The last alternative, 1 c), comprises the approach investigated in this thesis. This is considered the cheapest option, as the reservoir gas is utilized as the driving source. A similar dewatering approach was successfully conducted at the Snøhvit field. A downside with this option is the huge amount of contaminated water needed to be handled at the receiving facility onshore. However, as the development concept is based on dual trunklines, this can be avoided by reusing the same water to flood tunkline B, see illustration in Figure 6.3. Filtration at the onshore facility may be necessary depending on the contamination. After trunkline B has passed the hydrotest, the dewatering operation can be conducted from onshore to offshore, driven by production gas through trunkline A. Finally, the water can be discharged to deep sea at the PLEM, as illustrated in Figure 6.4.

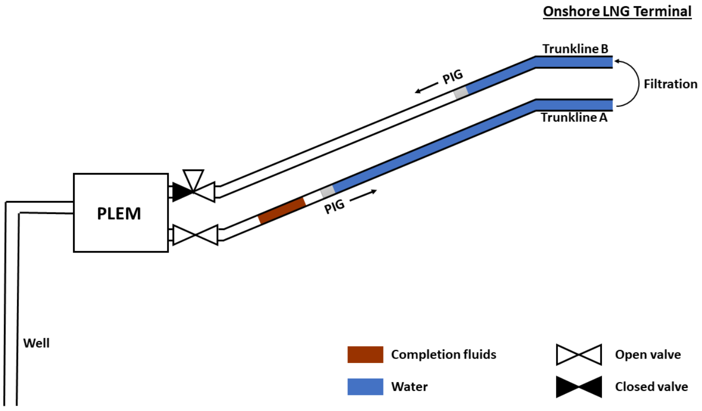
Onshore LNG Terminal
Trunkline B
Filtration
Trunkline A
PIG
PIG
PLEM
Well
Completion fluids
Water
Open valve
Closed valve

Figure 6.3: Dewatering of trunkline A combined with flooding of trunkline B

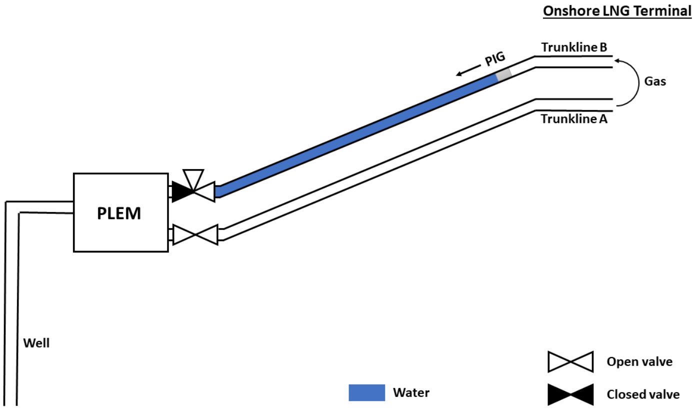
Onshore LNG Terminal
Trunkline B
Gas
Trunkline A
PIG
PLEM
Well
Open valve
Water
Closed valve

Figure 6.4: Dewatering of trunkline B utilizing production gas from trunkline A as driving force

Regarding well cleanup, there are two main options; cleanup to rig or to shore. Traditionally, cleanup to rig is performed. However, cleanup to process facilities onshore is considered beneficial as it could trigger substantial cost savings from reduced rig time. Furthermore, reduced environmental impact due to reduced hydrocarbon flaring and risk of discharges to sea are also positive outcomes (ref. Equinor). This thesis investigates how dewatering option 1 c) can be done in combination with well cleanup option 2 b). The main challenge with this combination is to obtain an initial well condition with a sufficiently high reservoir pressure able to flush the drilling- and completion fluids out of the well, and further dewater the trunkline, see Figure 6.3. As the initial water column in trunkline A causes a large hydrostatic pressure drop, the weight of the drilling- and completion fluid column must be sufficiently lower to achieve the desired overpressure. Exchange of heavy completion fluids with light reservoir gas, during a well suspension period under the influence of gravity, is considered as a possible solution, investigated in this thesis. However, equipment damage can be a potential risk as debris or larger particles are produced from the well. Subsea chokes might be restricted or completely blocked when mud passes through.

As the well cleanup and dewatering of trunkline A are considered the critical procedures during pre-commissioning, this will be the focus of this thesis. Flooding and dewatering of trunkline B will be doable after trunkline A is dewatered and the well is properly cleaned, hence those processes are not simulated in this thesis.

7 Simulation

Both well cleanup and dewatering are highly transient operations, hence, dynamic multiphase simulation is essential to model these operations with reasonable accuracy. This thesis utilizes a coupled OLGA-ROCX model, described in Chapter 4, to investigate the contingencies of combining these operations. This chapter highlights the simulation case, and describes how the simulations have been executed. To obtain a robust and efficient model, several sensitivity studies have been conducted. Furthermore, a detailed description of each part of the model, along with the simplifications applied, is provided.

7.1 Simulation case

The starting point for the present case is a newly drilled and completed well, filled with segregated drilling- and completion fluids. The trunkline is flooded with seawater, pre-commissioned and ready to be dewatered, see Figure 7.1.

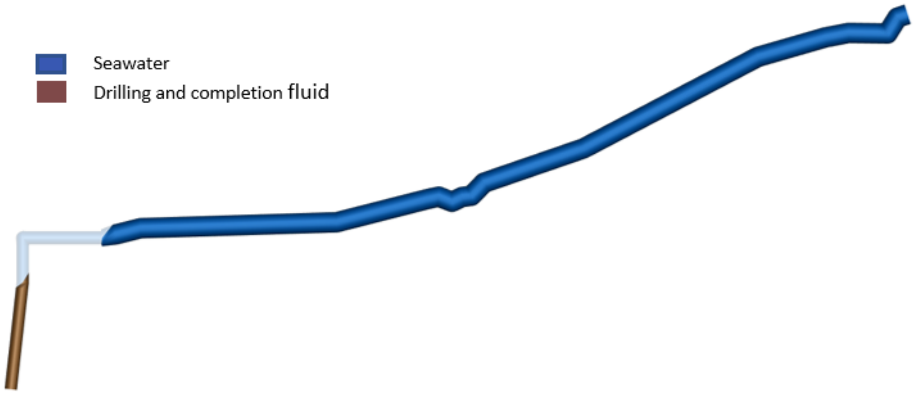

Figure 7.1: Starting point for Block 2

The start-up challenges described in Chapter 6.1 for the F-3H well at Snøhvit also account for this case. The initial pressure at the PLEM is fixed due to the hydrostatic pressure of the fully flooded trunkline. The reservoir pressure is slightly above the hydrostatic pressure at the reservoir depth. However, the initial liquid volume in the well needs to be reduced to perform an effective start-up operation. This will be achieved by suspending the well for a period of time to drain the drilling- and completion fluids into the reservoir under the influence of gravity.

During drilling, a mud cake is formed, constituting a low permeable layer at the wellbore wall, introduced in Chapter 5.1.2. As the mud invades the near-wellbore zone, through the mud cake, it is filtrated. Consequently, the viscosity of the mud decreases, and the resulting liquid is considered as filtrate hereafter. When the well is kicked off after the suspension period, the mud cake is expected to collapse, due to a drawdown pressure. Furthermore, the production gas will unload the well and drive a pigging train to dewater the trunkline. The pigging train will be controlled by a PID-controller, in order to retain the pig-velocity within reasonable limits.

7.2 Model verification

To produce reliable simulation results, a suitable grid for the simulation models must be determined. The aim of the gridding is to turn the flow domain into a discrete system on which the governing equations, presented in Chapter 2 and 3, can be solved numerically. The choice of gridding may have a considerable impact on the accuracy of the simulation results. The grid cells must be sufficiently small to provide an accurate numerical approximation, as this will reduce numerical dispersion. However, a fine grid will increase the CPU time. Grid sensitivity studies are conducted to obtain a grid able to provide accurate numerical solutions as well as keeping the CPU time within reasonable limits. In this section, the considerations made to determine the near-wellbore radius and suitable grid block sizes for both the OLGA and ROCX model are described.

7.2.1 Near-wellbore radius

Restart files are used to keep track of the mud content and distribution in the reservoir during well suspension, dewatering, cleanup and early production. Hence, the same reservoir model should be used in all the simulation cases. As mentioned in Chapter 4.2, the near-wellbore reservoir zone can either be modeled as a closed tank or with a pressure support at the outer boundary. Upon the assumption of an infinite acting reservoir, the closed tank reservoir must be sufficiently large to retain a constant pressure at the outer boundary. As the production case might require simulation times up to several months, an inconveniently large reservoir is required to ensure no pressure decline at the outer reservoir boundary. Alternatively, an infinite acting reservoir can be assumed during the dewatering and cleanup simulations, whilst a pressure support retains a constant pressure at the outer boundary for longer simulation periods. Both alternatives are investigated and compared with a standalone ROCX simulation study. Initially, the pressure in all cells is set to 415 bar, whilst the inner boundary condition is set to 390 bar. The inner boundary condition is based on the minimum pressure the coupled OLGA dewatering simulation reaches in the perforation section.

The theoretical radius of investigation, given by equation (2.33), is calculated from the reservoir properties given in Table 7.3 and the reservoir fluid properties given in Table 7.1. The fluid compressibility, c_f, and the hydraulic diffusivity are calculated using equation (2.1) and (2.28), respectively. The rock compressibility is assumed to be zero, hence the total compressibility, c_t, is equal to the fluid compressibility, by equation (2.29).

Table 7.1: Fluid properties at 420 bar and 81 °C

Interfacial tension oil-water, σ_{ow}	0.023 N/m
Interfacial tension gas-oil, σ_{go}	0.0008 N/m
Gas density, ρ	219 kg/m^3
Pressure derivative of density, $\frac{\partial \rho}{\partial p}$	3.25e-6 kg/mN
Total compressibility, c_t	1.48e-8 1/Pa
Hydraulic diffusivity, η	1.41 m^2/s

7.2.2 Number of grid blocks in the ROCX model

In order to obtain a suitable grid in ROCX, a simplified dynamic case is designed for this purpose. The actual simulation case, described in the above section, is too complex and computational heavy for such a comprehensive sensitivity study. The simplified case consists of a separate stabilization case with a closed glass plug, see Figure A.1 in Appendix A, and one dynamic case including both the suspension and drainage scenario, as well as the kickoff followed by a few hours of production, see Figure A.2 in Appendix A. Initially, the deviated section in-between the glass plug and kickoff is filled with drilling mud. To save simulation time, no mud cake is considered in this simplified case. The well is suspended until all the mud is drained into the reservoir.

The initial pressure in the reservoir in the stabilization case is determined based on a standalone simulation in ROCX, under the influence of gravity only. The reservoir in the standalone simulation is modeled as a closed tank without a well, with an initial pressure of 415 bar in all cells. The initial pressure in the perforation section in OLGA is fixed according to the reservoir pressure in each vertical layer. In the stabilization case, the glass plug and production choke at the wellhead are both closed, and the case is simulated until a steady condition is reached in the entire system. Of particular interest is a steady condition through the near-well sources between ROCX and OLGA, as a dynamic condition with circulations between the near-well sources could potentially influence the drainage. Furthermore, this stabilization case is used as a restart file for the dynamic case in both OLGA and ROCX. Initially, the dynamic case starts with an open glass plug, and the liquid in the well is expected to drain backwards into the reservoir under the influence of gravity only. The next action is the kickoff, initialized by opening the wellhead choke, followed by a few hours of production.

The first grid sensitivity to be conducted is the gridding in vertical direction in ROCX. Vertically, the grid must be sufficiently fine to be able to reproduce viscous- and gravitational effects. During this grid sensitivity, one grid block in angular direction and 20 grid blocks in radial direction are used, chosen rather arbitrarily. When the number of grid blocks in vertical direction is determined, sensitivity on the gridding in radial direction is conducted. Grid refinement in radial direction toward the well in the ROCX model is crucial in order to capture the transient behavior around the wellbore with more accuracy, as the near-wellbore area is the area of most interest. However, excessive grid refinement increases the number of cells, and thus increases the CPU-time accordingly. Consequently, it is desirable with a small number of grid blocks in radial direction. Finally, the effect of gridding in angular direction, and how three-dimensional effects in the reservoir affect the simulation results, is investigated. It is considered especially beneficial to limit the gridding in angular direction to as few grid blocks as possible, as more grid blocks in angular direction require more near-well sources. Reason being that one near-well source only can be coupled with one grid block boundary in ROCX. Figure A.3 in Appendix A shows a model for 8 grid blocks in angular direction and 3 grid blocks in vertical direction, constituting 24 near-well sources, which is undesirable.

7.2.3 Number of grid blocks in the OLGA model

To reduce the CPU-time further, the provided trunkline profile in OLGA is simplified, using the standalone Profile Generator tool in OLGA. While maintaining the key characteristics of the original profile, the number of data points is reduced from 528 to 17, see Figure D.5 in Appendix D. The main geometry is retained, whilst local elevation differences smaller than approximately 30 m are not captured by the simplified profile, resulting in a loss of 25 m length. However, this is considered to not have a significant influence on the objective of this thesis.

When it comes to gridding in OLGA, careful considerations must be made. In general, large variations in grid block size of neighboring cells are undesirable. It is considered good practice to keep all grid cells within the range 50-150% of the neighboring cell size, thus, used as a basis for the gridding in this thesis. To determine the gridding in OLGA, the built-in discretization function is used. The grid is constructed based on two criteria; minimum number of sections per pipe and maximum section length. As the coupling section between ROCX and OLGA must be equal in size, the grid in the perforation section of the well is manually fixed corresponding to the gridding in vertical direction in ROCX. Consequently, the grid sensitivity is performed from the top of the perforation section on, using the same simplified case as in the grid study in ROCX.

7.3 Sensitivity studies on reservoir parameters

Prior to running the suspension case, sensitivity studies on formation- and mud cake properties are performed, to assess their effect on the mud invasion and well cleanup, utilizing the simplified dynamic case. The first sensitivity study investigates the impact of relative permeability. The Corey correlation, introduced in Chapter 2.2.5, is used to determine the relative permeability curves. Throughout the sensitivity study on relative permeability, capillary pressure is neglected.

As no experimental core data are obtainable for this specific reservoir, the capillary pressures must be estimated. Equation (2.16) combined with equation (2.17) is used to obtain a rough estimate of the value for the capillary pressure between the different phases within the pores. Zero contact angle, θ, yields the maximum capillary pressure, hence this is the most conservative estimate for a water-wet reservoir. Sensitivity on capillary pressure curvature is performed. The investigated oil-water curvatures are defined by a half-saturation exponential decay

$$P_{cow}(S_w) = \begin{cases} P_{cow,max}e^{-\lambda S_w} & 0.0 \geq S_w \leq S_{wa} \\ \frac{P_{cow}(0.4)}{1-0.4}(1-S_w) & S_{wa} < S_w \leq 1.0 \end{cases} \tag{7.1}$$

where

$$\lambda = \frac{\ln 2}{S_{w1/2}} \tag{7.2}$$

$S_{w1/2}$, from now on called the half-saturation, is the saturation when the maximum capillary pressure reaches half of its value. The gas-oil capillary pressure curve stays unchanged as a straight line while the effect of different P_{cow} curvatures is investigated. Afterward, the effect of gas-oil curvature is investigated with a fixed oil-water capillary curve.

A mud cake with thickness of 3 mm and permeability of 0.001 mD is assumed to be present at the wellbore wall. The mud cake can be modeled using two different approaches; by adding a low permeable grid block adjacent to the wellbore wall, or by adding a skin factor at the wellbore wall. The latter approach is desirable as the skin factor does not influence the grid in radial direction and can be provided as a time-series in ROCX. Hawkins' equation (2.19) is used to calculate a skin factor corresponding to a damaged zone of the given permeability and thickness. To verify that Hawkins' equation can be applied for a thin mud cake of very low permeability, a simulation study is conducted to relate skin and mud thickness for a fixed mud permeability. Standalone ROCX simulations with fixed inner- and outer boundary pressures are conducted to obtain the steady-state production rate for different mud thicknesses and skin factors. The results obtained by the two simulation approaches are compared, to couple the mud thicknesses and the skin factors yielding the same production rates.

During the well suspension, the mud density, mud cake properties and the length of the damaged zone are considered to be the variables of most influence on the drainage rate. Hence, sensitivity studies on the aforementioned variables are conducted. The sensitivity on mud density is performed simply by modifying the density in the mud PVT table. By varying the skin factor at the well boundary, Hawkins' equation (2.19) provides insight into the effect of mud cake thickness- and permeability. In order to conduct sensitivity on the damaged zone length, the corresponding grid blocks representing the length of interest are initially saturated with filtrate.

As the well is kicked off, it is assumed that the entire mud cake is collapsed, with a sufficient pressure drawdown. However, a sensitivity study is conducted on different skin factors after kickoff, modeling the remaining mud cake amounts on the wellbore wall. As these simulations are considered time-consuming, a simplified suspension model is created for this purpose. For simplicity, the infield flowlines, the trunkline and the wellhead choke are removed, replaced by a closed node at the wellhead, see Figure A.4 in Appendix A.

7.4 Simulation execution

With a robust and efficient model obtained based on the aforementioned sensitivity studies, the simulation case is conducted. The simulations are executed in several steps, using four different OLGA models with corresponding ROCX models. Table 7.2 below provides an overview of the models.

Table 7.2: Overview of OLGA models

	Stabilization	**Well suspension**	**Cleanup and dewatering**	**Early production**
Model purpose	Insert pig and stabilize the system	Well suspension to drain the mud into the reservoir	Well unloading, pigging and dewatering	Early production to investigate the mud displacement
Initial condition	53% mud and 47% brine in deviated well section, trunkline filled with seawater and gas elsewhere	Restart file from the stabilization model	Restart file from the well suspension model	Restart file from the cleanup and dewatering model
Boundary condition well	3 mm mud cake with permeability 0.001 mD	3 mm mud cake with permeability 0.001 mD	No mud cake	No mud cake
ROCX file	Initial reservoir saturated with 100% gas	ROXC file with restart file from stabilization case	ROXC file with restart file from suspension case	ROXC file with restart file from cleanup and dewatering case
Status glass plug	Closed	Fully open	Fully open	Fully open
Status wellhead choke	Closed	Closed	Open 20%	Open 20%
Onshore choke	Open 5%	Open 5%	Controlled by PID	Fully open
Simulation time	14 days	7 days	2 days	60 days
Model illustration	A.1	A.5	A.6	A.5

Initially, the deviated section in-between the glass plug and the kickoff is filled with 53% mud and 47% brine. This is in correspondence with the fraction of mud- and brine volumes in the F-3H well prior to startup at Snøhvit, see Chapter 6.1. The drilling option is turned on in order to keep track of the different liquids in the well. In the above sensitivity studies, all mud and brine in the well is completely drained. However, not all the drilling- and completion fluids necessarily need to be removed in order to achieve an effective startup. In general, it is not desirable to have mud in the reservoir. Consequently, the minimum drainage volume resulting in a sufficient pressure drop across the wellhead choke, is to be found. It is assumed that a pressure drop of 20 bar across the wellhead is sufficient to collapse the mud cake at the inner wellbore wall and unload the well. Thus, simulations aiming at a pressure drop greater than 20 bar are conducted.

The suspension case is further used as a restart case for the cleanup- and dewatering case. The kickoff simulation is initialized by opening the wellhead choke and remove the skin factor. To retain the pig velocity within reasonable limits, a PID controller is utilized to control the valve at the trunkline outlet to constrain the flow during dewatering. The dewatering simulation is followed by 2 months of early production, in order to investigate the filtrate displacement from the reservoir.

7.5 ROCX model

In order to track the drilling- and completion fluids drained into the reservoir during well suspension and the reservoir flushing after well kickoff, a ROCX model is utilized. In addition, the ROCX model is capable of capturing the transients associated with the combined well cleanup and dewatering procedure. The simulations are based on the Zafarani wells on Block 2, which will be the first brought into production. The reservoir rock- and fluid properties for a zone in Zafarani are taken into account in this thesis, summarized in Table 7.3.

Table 7.3: Reservoir properties for a zone in Zafarani

Mid zone producing depth	3886 m TVDSS
Mid zone initial pressure	415 bara
Mid zone temperature	81°C
Length of producing zone	141 m
Porosity, ϕ	0.22
Permeability ϕ-dir, K_ϕ	130 mD
Permeability r-dir, K_r	130 mD
Permeability z-dir, K_z	13 mD
Irreducible water saturation, S_{wi}	0.15
Residual gas saturation, S_{gr}	0.3
K_{rg} at $S_w = S_{wi} = 0.15$	0.9
K_{rw} at $S_g = S_{gr} = 0.3$	0.2

Reservoir rock properties such as porosity and absolute permeability are assumed constant in space, which is a reasonable simplification at this early stage. Relative permeability curves are obtained using the Corey correlation, based on the relative permeability endpoints given in Table 7.3. However, some modifications regarding the endpoints are conducted, including neglecting the irreducible water saturation. For tracking purposes later on in the simulations, no water initially in the reservoir is assumed, yielding $K_{rg} = 0.9$ at $S_w = 0$. Due to numerical reasons, ROCX automatically adds (0,0) and (1,1) to Corey. Hence, in order to apply Corey on the gas relative permeability, the endpoint at $S_w = 0$ or $S_g = 1$ is shifted from $K_{rg} = 0.9$ to $K_{rg} = 1$, which is considered to not have a major effect.

The reservoir fluid properties are provided as a PVT file to ROCX. In addition to reservoir rock- and fluid properties, grid and initial- and boundary conditions also need to be specified in ROCX. As the simulation case is a near-wellbore study, dominated by radial inflow, a radial grid with logarithmic block size distribution in the radial direction is used in the reservoir model. While grid refinement is used in radial direction, the grid block sizes in angular- and vertical direction are constant. The radius of the near-wellbore reservoir zone and the gridding in the ROCX model are determined based on sensitivity studies. Figure 7.2 below illustrates a radial reservoir grid, with grid block indices. In a radial grid, the well is directed along the z-axis. In the present ROCX model, the gravity direction is defined in negative z-direction, constituting a straight vertical well, whereas the actual wells in Zafarani are 45°inclined. However, as the x-axis is perpendicular to the direction of the well for a radial grid, a deviated well would yield a corresponding deviated reservoir, which is undesirable.

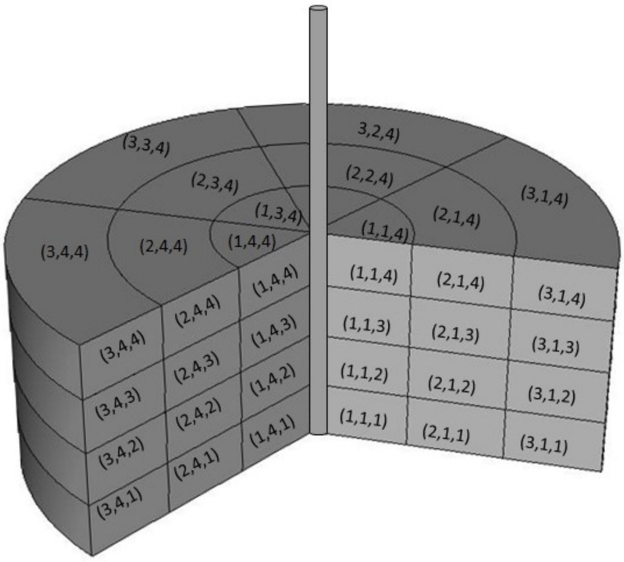

Figure 7.2: Numerical grid block indices

Each numerical grid block in the reservoir model is initially saturated with 100% gas, assuming no water or oil. The initial pressure in each numerical layer in vertical direction is determined based on a standalone simulation in ROCX with an initial pressure of 415 bar, under the influence of gravity only. The initial temperature is set equal to the mid zone temperature of 81°C in all cells. Temperature calculations are not carried out in the reservoir model, as temperature variations in the near-wellbore region are not of interest to simulate. Hence, no thermal rock properties are provided.

Boundary conditions are provided for each cell adjacent to the wellbore boundary. Thus, the number of well boundary conditions required depends on the number of grid blocks in angular- and vertical direction. The skin factor, pressure and temperature are provided as a well boundary condition. Based on the sensitivity on near-wellbore radius, it is decided whether a boundary condition should be provided at the outer reservoir boundary, or not. A fixed pressure boundary condition at the outer boundary will provide the reservoir with pressure support, whereas a non-defined boundary condition at the outer boundary constitutes a closed boundary system with no flow.

7.6 OLGA model

In order to couple the ROCX model to an OLGA model, a near-well source is defined in OLGA for each wellbore boundary condition provided in ROCX. The simulation case assumes open hole completion, constituting a perforation zone in OLGA fully exposed to the reservoir. Thus, the gridding in the perforation zone in OLGA should be fixed in correspondence with the gridding in vertical direction in ROCX, meaning equivalent grid block sizes.

The OLGA model incorporates a Zafarani well tied back through flowlines to shore. The wellbore consists of a 141 m vertical perforation section, a 1780 m 38°inclined section and a 500 m vertical section from kickoff to the wellhead located at the seabed. A tubing disappearing glass plug is located above the perforation section, and production chokes are located at the wellhead and at the trunkline outlet, respectively. All chokes are modeled as orifice hydrovalves in OLGA. The well is tied back through a 150 m spool and a 9850 m infield flowline to a PLEM located at 2234 m TVD, modeled as an internal node. The seabed profile in-between the wellhead and the PLEM is unknown, hence the spool and the infield flowline are assumed to be horizontal, see Figure 7.3 a). From the PLEM, the reservoir fluids are transported further through a 101.617 km trunkline to the separator onshore, modeled as a pressure node fixed at 70 bara and a temperature of 30°C. Figure 7.3 b) shows the flow path from the reservoir to the receiving LNG plant onshore along with the corresponding ambient temperature.

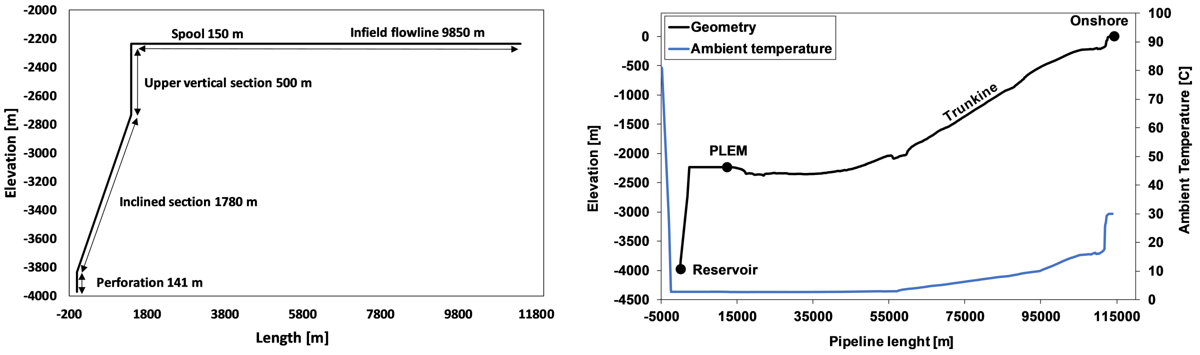

(a) (b)

Figure 7.3: a) Zafarani well and infield flowline profile and b) complete flow path and ambient temperature profile on Tanzania Block 2

The pipe roughness is 0.05 mm in the wellbore and for the infield flowline, and 0.03 mm for the trunkline. Furthermore, pipe dimensions and coatings for the tubing, spool, infield flowline and trunkline are specified in the model, presented in Figure 7.4. Corresponding material properties and heat transfer coefficients are given in Table 7.4 and 7.5, respectively. With temperature calculations set to WALL in OLGA the fluid temperature gets affected by the temperature of the surroundings as described in Chapter 3.2.3. The temperature setting FASTWALL is used in the stabilization case to obtain steady-state temperature solutions faster from initial conditions. The temperature is calculated in the same manner as for WALL, however, heat storage within the pipe wall is neglected in FASTWALL.

Table 7.4: Material properties

	Capasity [J/kgC]	**Conductivity [W/mK]**	**Density [kg/m^3]**
Steel	460	45	7850
Polypropylene, PP	1800	0.22	900
Fusion bonded epoxy, FBE	1800	0.30	1500
Formation, FORM	1320	2.30	2000

Table 7.5: Heat transfer coefficients at pipe boundaries

	Min. h_i [W/m^{2}C]	**h_{amb} [W/m^{2}C]**
Tubing	0	5
Spool	0	70
Infield flowline	0	70
Trunkline	10000	1000

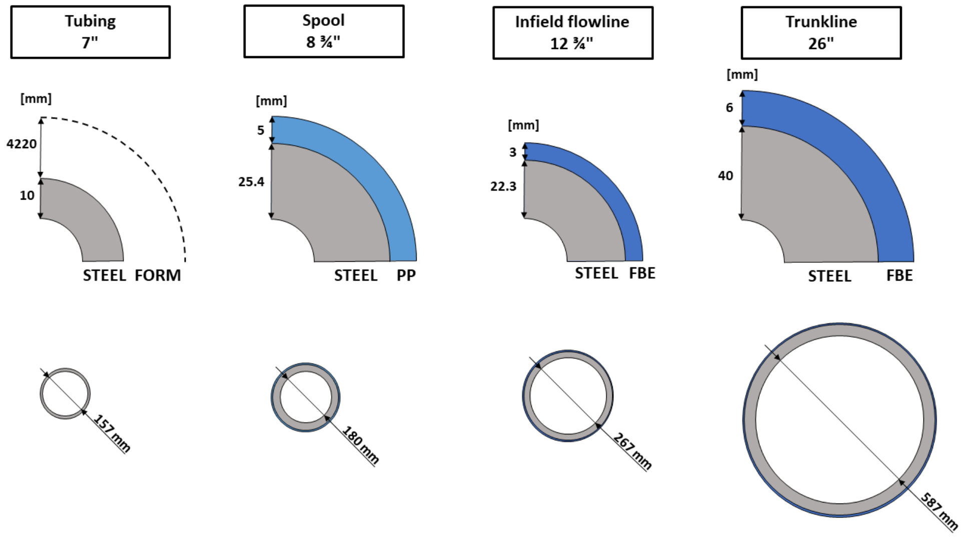

Figure 7.4: Pipe design

As described in Chapter 4.1.1, OLGA models three phases; gas, oil and water. The simulation cases introduced in Chapter 7.4 include modeling of six different fluids; hydrocarbon gas, condensate, mud, filtrate, brine and seawater. As a water-based mud is assumed, the four latter are modeled as the water phase. To be able to separate them from each other, the drilling fluid option is used. The drilling option includes one additional mass equation for each drilling fluid, enabling the fluids to be tracked throughout the pipeline. As the four fluids are still treated as one phase in the momentum and energy equations, slip can not occur in-between them. One PVT table is provided for each drilling fluid, and the fluid properties of the mixture are calculated by interpolation in-between the PVT tables.

The fluid property tables are generated using the standalone fluid-package OLGA Fluid Definition Tool. A PVT table describing the reservoir fluids in Zafarani is provided by Equinor. This is used as the base PVT in the Fluid Definition Tool to generate tables for mud, filtrate, brine and seawater. Modifications in the water phase are calculated using the built-in tool based on the densities and viscosities specified in Table 7.6. The properties are assumed equivalent as on Snøhvit at standard conditions.

Table 7.6: Mud and brine properties at standard conditions

	Density [kg/m^3]	**Viscosity [CP]**
Mud	1150	14
Brine	1100	1
Filtrate	1150	0.5
Seawater	1030	1.08

After the mud has passed through the mud cake, it is considered as filtrate. Thus, the filtrate PVT table is used in the reservoir. To avoid the filtrate from being modeled with mud properties as it enters the wellbore again, the filtrate PVT is also used as the main PVT in OLGA. This implicates that brine in the reservoir and condensed water in the pipeline will be calculated with filtrate properties. As most of the brine is expected to remain in the well during suspension, and water, brine and filtrate properties are rather similar, this is considered to not cause any problems. Mud, brine and the seawater ahead of the pig is addressed as drilling fluids. The fluid property configuration is illustrated in Figure 7.5.

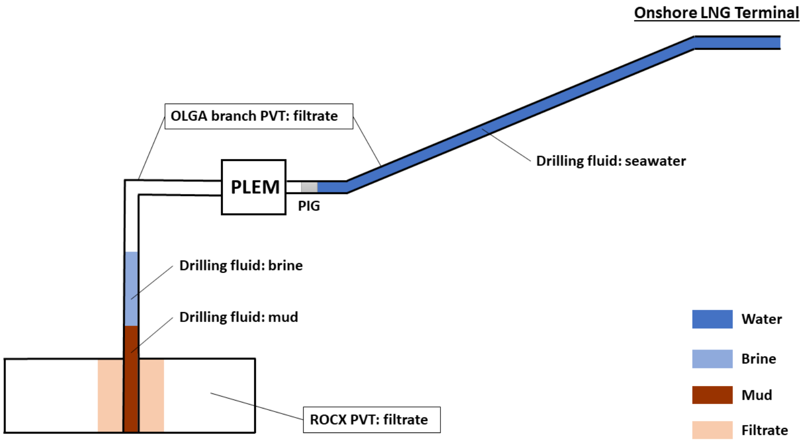
Onshore LNG Terminal
OLGA branch PVT: filtrate
PLEM
PIG
Drilling fluid: seawater
Drilling fluid: brine
Drilling fluid: mud
ROCX PVT: filtrate
Water
Brine
Mud
Filtrate

Figure 7.5: Illustration of the PVT files implemented in the model

As the pig travels through the pipeline, the hydrostatic pressure will decrease and the pig velocity will increase accordingly. In order to maintain the pig velocity within reasonable limits, a PID controller is utilized to regulate the valve at the end of the trunkline. The controller regulates the total volume flow rate based on measurements received from the transmitter located upstream of the valve. As the pipeline downstream of the pig is completely filled with seawater, which is incompressible, the pig velocity is strongly coupled with the total volume flow rate.

The output signal from the controller is set to be within a range of 0-0.05, constituting a valve opening spanning from closed to 5% of fully open. Larger choke openings are not necessary and will only slow the response of the controller as it requires some time to close the choke from fully open. The initial value of the controller is set to its maximum, 0.05. For practical reasons, a manual controller is also implemented to override the PID controller when necessary.

8 Results

The results from the simulations are presented in this chapter. Firstly, the results from the sensitivity on near-wellbore radius and the grid sensitivity study are presented. Furthermore, the results from the sensitivity on reservoir parameters are presented. Finally, the simulation results are presented. As the drilling- and completion fluids are modeled as water, they will be expressed interchangeably with water hereafter.

8.1 Near-wellbore radius

Figure 8.1 shows how a pressure front propagates through an infinite acting reservoir before the boundary is reached. The pressure distribution curves are plotted with semi-logarithmic axes. A linear behavior is observed, which is in good agreement with the theory described in Chapter 2.5.

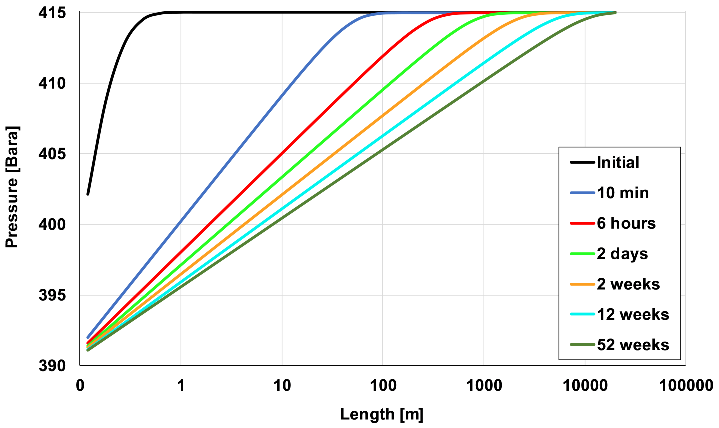

Figure 8.1: Pressure distribution for an infinite acting reservoir

In Figure 8.2 a), the simulated radius of investigation is plotted along with the theoretical curve calculated in Chapter 7.2.1. The position of the simulated radius of investigation is plotted as the largest radius where the pressure has decreased with at least 0.2 bar. The simulated radius of investigation increases with $\sqrt{t}$, which is in correspondence with the theoretical curve. Figure 8.2 b) shows how the theoretical radius of investigation increases during a period of several months.

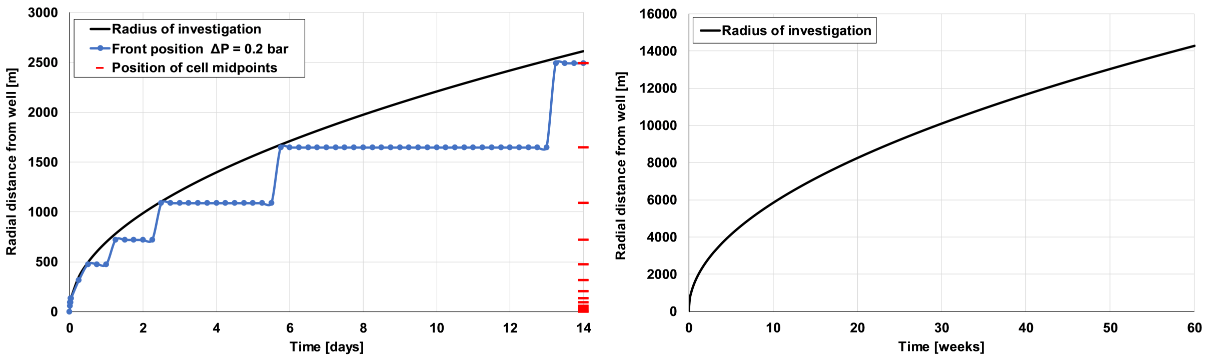

(a) (b)

Figure 8.2: Position of the pressure front for a) $\Delta P = 0.2$ bar and b) an infinite acting reservoir

To fulfill the assumption of an infinite acting reservoir, the reservoir must be very large, see Figure 8.2 b). Based on the results in Figure 8.2 a), a reservoir of radius 2000 m can be assumed to be infinite acting for two days, which will most likely cover the dewatering period with some margins.

Figure 8.3 shows how the pressure distribution in radial direction varies with time for a reservoir of radius 2000 m, with and without a pressure support at the outer boundary, respectively. Figure 8.4 shows how the same two reservoir models behave compared to a large infinite acting reservoir. Based on these results, a reservoir with a radius of 2000 m with pressure support at the outer boundary is used in further simulations.

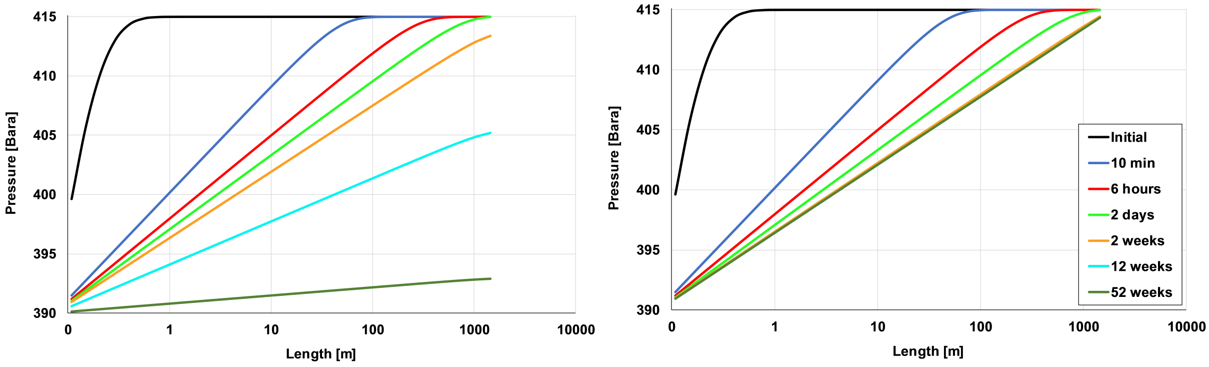

(a)

(b)

Figure 8.3: Pressure distribution for a reservoir of 2000 m radius modeled as (a) a closed tank (b) with pressure support at the outer boundary

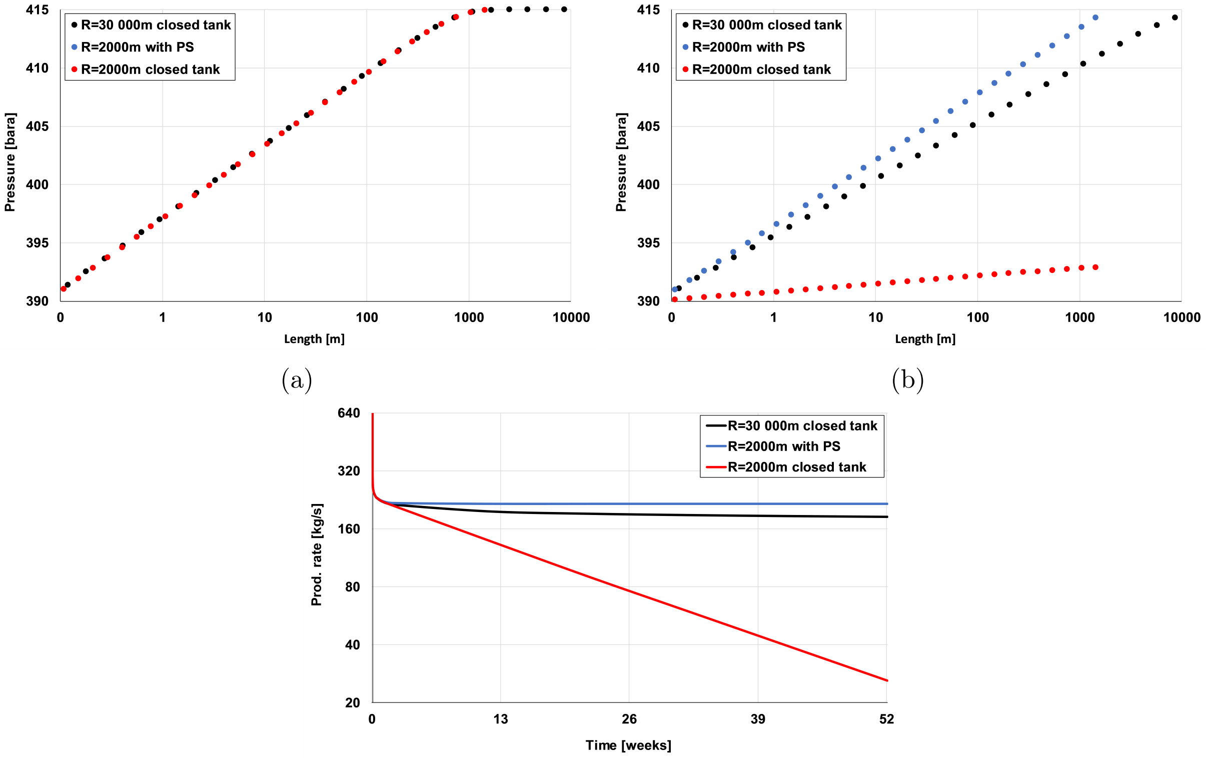

(a)

(b)

(c)

Figure 8.4: Pressure distribution after a) 2 days and b) 52 weeks, and c) production rate for infinite acting reservoir and a 2000 m reservoir modeled as closed tank and with pressure support

8.2 Grid sensitivity study

With the near-wellbore radius determined, sensitivity on how to turn the reservoir into a discrete system is conducted. During the well suspension, the main variable of interest is the drainage rate, which is investigated using the OLGA variable WATC (Water content in branch). Moreover, the total mass flow rate, the GT-variable in OLGA, above the perforation is a variable of great interest in revealing instabilities in the flow during the grid determination. However, prior to performing the grid sensitivity, a pressure drop sensitivity across the glass plug is conducted, as this may be decisive on the drainage rate.

8.2.1 Pressure drop sensitivity across the glass plug

To investigate the effect of pressure drop across the glass plug, sensitivity on different initial pressure drops is conducted, see Figure 8.5. Initial over- or underpressure across the glass plug yields quite different results during the drainage period. Instabilities and a delayed drainage startup are observed for both over- and underpressure. For small pressure drops, however, the drainage commences immediately and stability during the drainage is obtained. No initial pressure drop is assumed in further simulations.

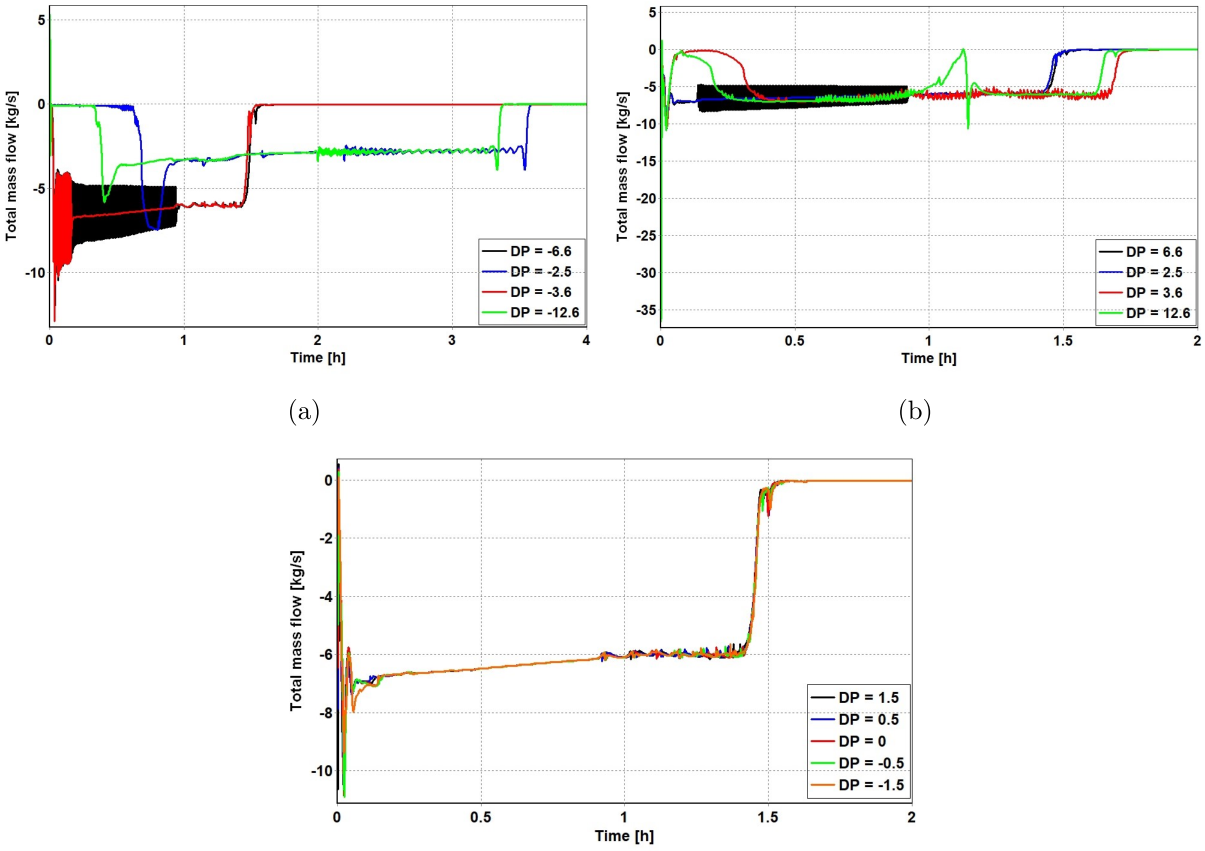

(a)

(b)

(c)

Figure 8.5: Total mass flow above perforation for a) underpressure, b) overpressure and c) small pressure drops across the glass plug, respectively

8.2.2 Vertical gridding in ROCX

To evaluate the effect of the gridding in vertical direction on the drainage rate of mud in the well, the water content in the well during the suspension and kickoff is plotted in Figure 8.6 a). It is observed that the mud will not drain to the reservoir during the suspension for one grid block in vertical direction in ROCX. For 10 grid blocks, the drainage rate is slower compared to the cases for 3,4,5 and 8 grid blocks. The total mass flow above the perforation during the drainage for different number of grid blocks in vertical direction is shown in Figure 8.6 b). Oscillating behavior is observed for 1, 8 and 10 grid blocks during the drainage, whilst 3, 4 and 5 grid blocks promote a stable drainage period. To keep the number of near-well sources low, 3 grid cells in vertical direction are chosen in further simulations.

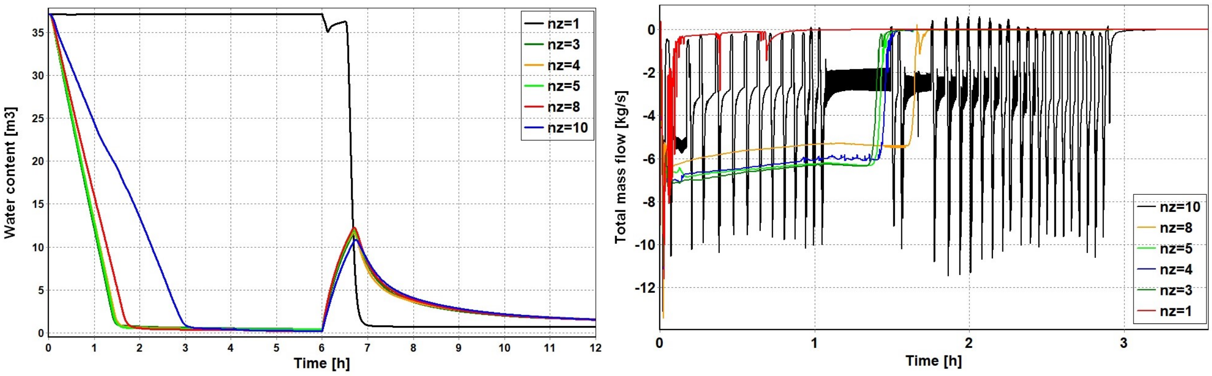

(a) (b)

Figure 8.6: a) Water content in the well and b) total mass flow above perforation during drainage for different number of grid blocks in z-direction

8.2.3 Radial gridding in ROCX

Prior to carrying forward the grid sensitivity in radial direction, the effect of a logarithmic grid is investigated. In the case of uniform grid blocks in radial direction, a large number of grid blocks are required in order to capture the physics during the suspension and kickoff, see Figure 8.7 a). As this is undesirable in terms of computational time, a logarithmic grid is used in further simulations.

Sensitivity on the number of radial grid blocks on a logarithmic grid is presented in Figure 8.7 b), showing the water content in the well. It is observed that the drainage rate is more or less independent of the number of grid blocks in radial direction, whilst some deviations are present in the flushing rate after kickoff. 5 and 10 grid blocks yield a conspicuously slower flushing, compared to the other cases. 15 to 100 grid blocks yield approximately the same curve, with a slightly higher peak for an increasing number of grid blocks.

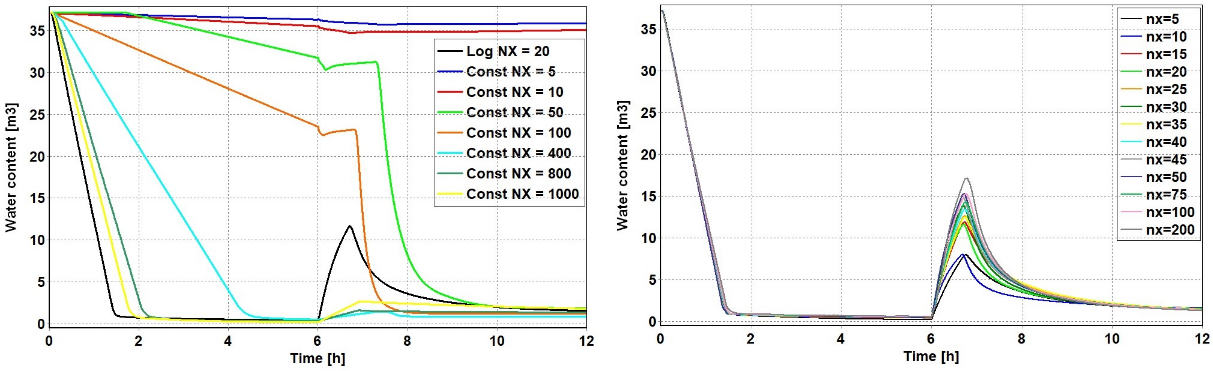

(a) (b)

Figure 8.7: Water content in the well for a) uniform grid and b) logarithmic grid for different number of grid blocks in radial direction

Moreover, stability during the drainage is preserved in most cases, except for 30, 45 and 50 grid blocks, where oscillations occur, see Figure 8.8 a) and b). Furthermore, oscillating behavior in the flow rate is observed during early production with few grid blocks, but is reduced with an increasing number of grid blocks, see Figure 8.8 c). As the CPU-time is highly affected by the number of grid blocks in radial direction, 20 is chosen in further simulations.

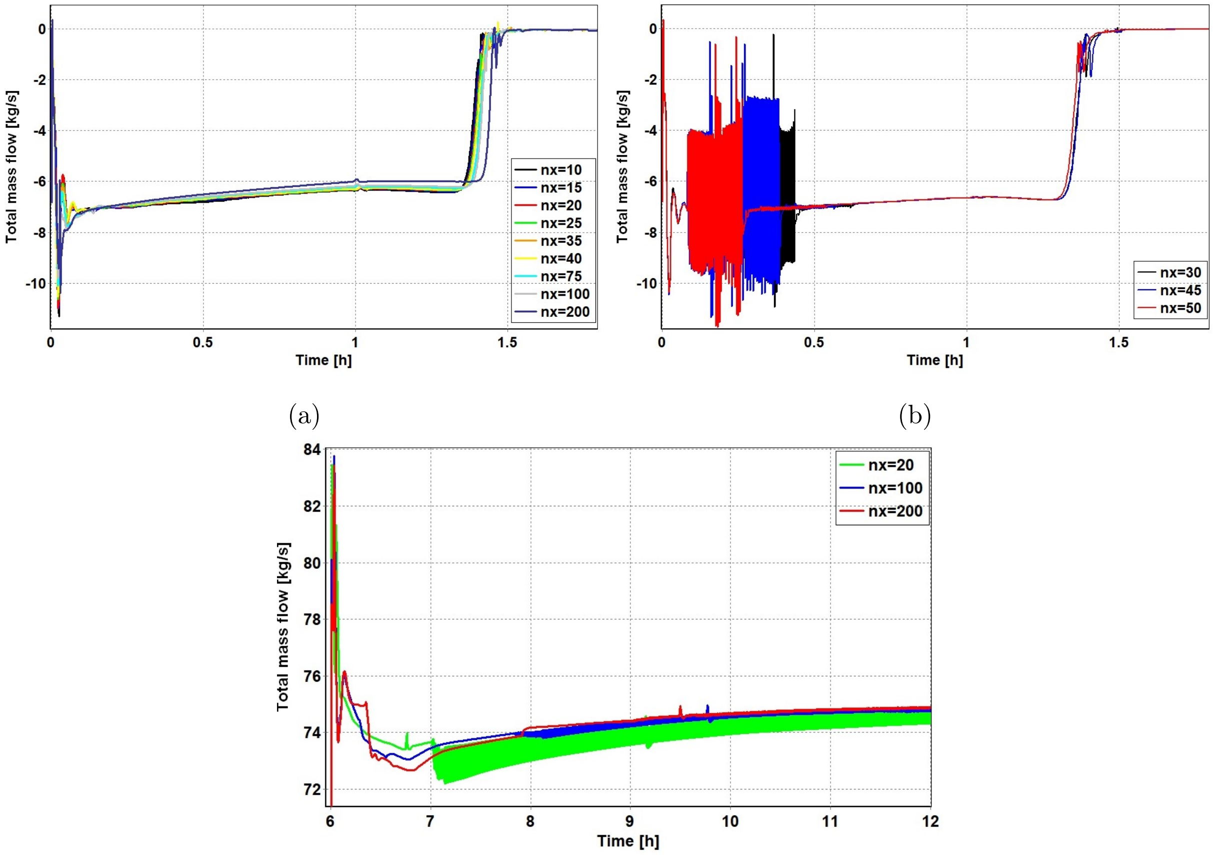

(a) (b)

(c)

Figure 8.8: Total mass flow above perforation during a), b) drainage and c) during kickoff for different number of grid blocks in z-direction

8.2.4 Angular gridding in ROCX

A delayed drainage startup is observed for 4 grid points, whilst the drainage for 1,2 and 8 grid blocks commence immediately, see Figure 8.9. As 8 and 2 grid blocks coincide with the two-dimensional case of 1 grid block, neglecting the three-dimensional effects in the reservoir shows to be a reasonable assumption. Furthermore, oscillations occur in the flow after kickoff for 8 grid blocks, providing a reason for not choosing 8 grid blocks.

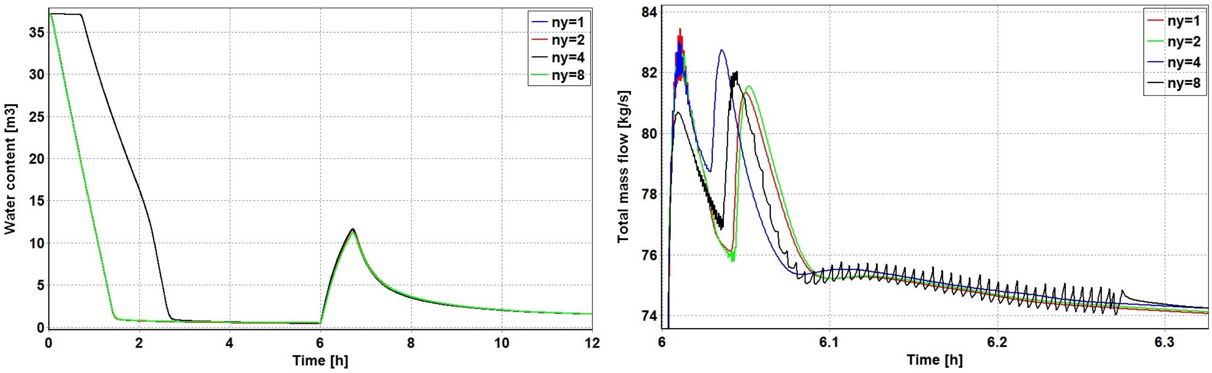

(a) (b)

Figure 8.9: a) Water content in the well and b) total mass flow above perforation during production for different gridding in angular direction

The final grid determined in the above sections is illustrated in Figure B.2 in Appendix B.

8.2.5 Gridding in OLGA

The simulation results for 4 different grids in OLGA are shown in Figure 8.10. Oscillating behavior is observed during drainage for the finest grid, see Figure 8.10 b). As the flow rate oscillates around the drainage rate of the stable cases, no effect is observed on the water content in the well. In further simulations, a minimum of 3 sections per pipe and maximum section length of 100 m is chosen.

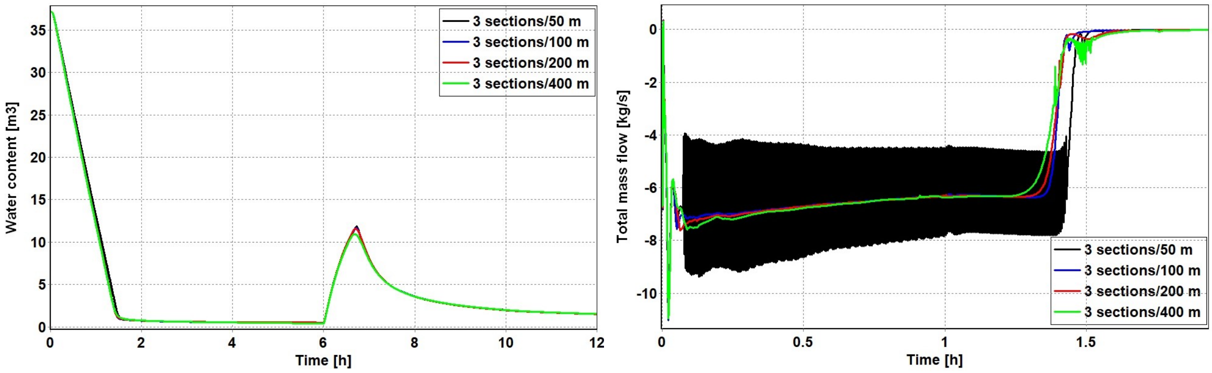

(a) (b)

Figure 8.10: a) Water content in the well and b) total mass flow above perforation during drainage for different gridding in OLGA

8.3 Sensitivity studies on reservoir parameters

With an optimal grid determined, sensitivity on relative permeability and capillary pressure curves is conducted. As not sufficiently details on relative permeability and capillary pressure are provided for this specific case, the remaining details are determined based on the results presented below. In addition, a skin factor for the mud cake is determined, before sensitivity studies on different mud densities, skin factors and damaged zone lengths are conducted.

8.3.1 Relative permeability curves

By keeping the modified relative permeability endpoints given in Table 7.3 fixed, the curvature defined by the Corey exponent is varied, see Figure 8.11 a). $K_{rgom} = 1$ is held fixed, yielding $K_{rg} = 1$ at $S_g = 1$ for the gas relative permeability for varying Corey exponents. K_{rwoc}, on the other hand, is varied for each Corey exponent, in order to keep $K_{rw} = 0.2$ at $S_w = 0.7$ for the water relative permeability fixed. The curvature shows no effect on the drainage rate, however, some deviations in the flushing are present, see Figure 8.11 b). Stability is preserved in all cases, see Figure 8.11 c).

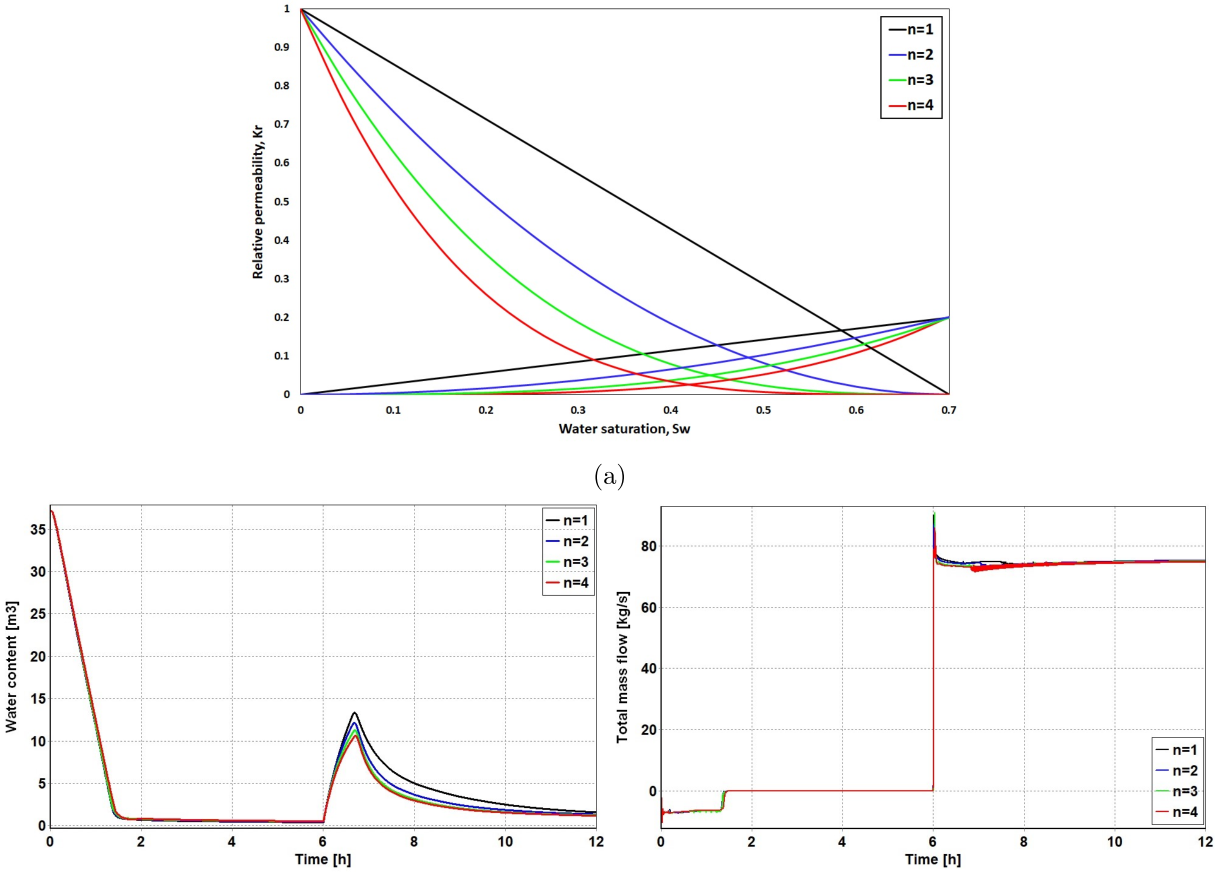

(a)

(b)

(c)

Figure 8.11: a) Relative permeability curves, b) water content in the well and b) total mass flow above perforation for different Corey exponents

In order to keep $K_{rw} = 0.2$ at $S_w = 0.7$ fixed, K_{rwoc} is adjusted for each Corey exponent, by rearranging equation (2.9). The effect of varying K_{rwoc} for different Corey exponents is presented in Figure 8.12 below. It can be observed that the cases for large Corey exponents are highly sensitive to changes in K_{rwoc}. Corey exponent 2, however, remains more or less unaffected with varying K_{rwoc} throughout the simulation, see Figure 8.12 a) and b). Thus, Corey exponent 2 is chosen in further simulations.

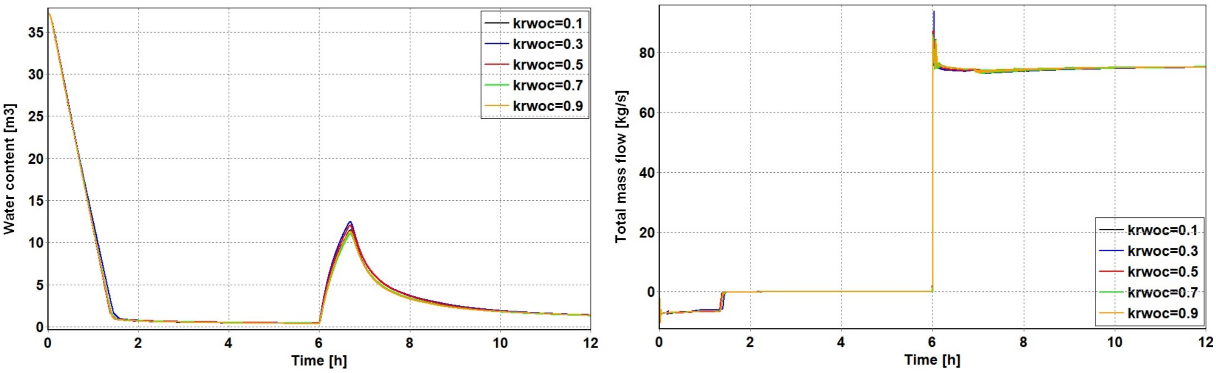

(a) $n = 2$

(b) $n = 2$

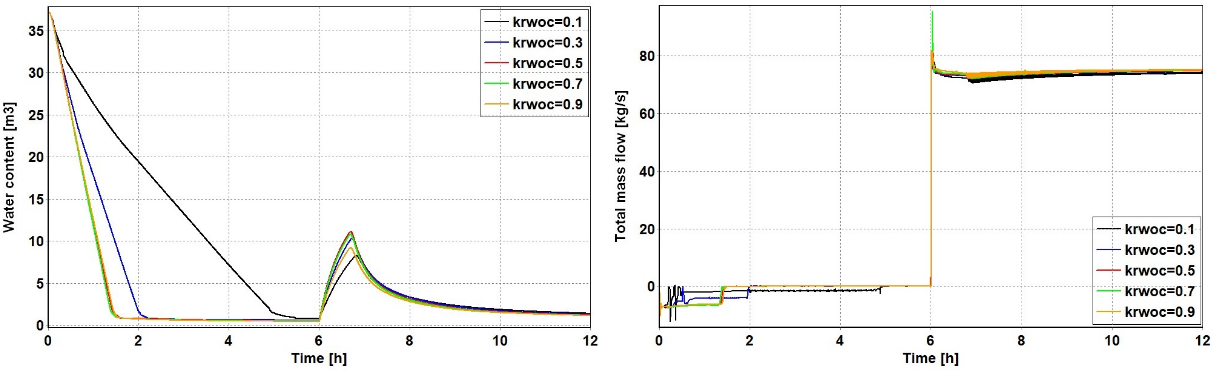

(c) $n = 3$

(d) $n = 3$

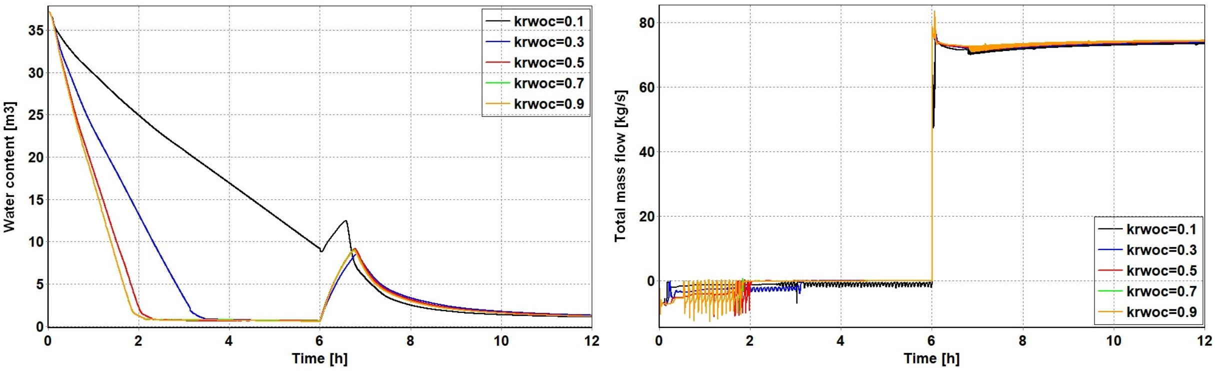

(e) $n = 4$

(f) $n = 4$

Figure 8.12: Water content in the well and total mass flow above perforation for different values of K_{rwoc}

8.3.2 Capillary pressure curves

Figure 8.13 a) shows the effect of different capillary pressure curves, presented in Figure 8.13 b) and c). All curves have the same shape, but with different values of the maximum capillary pressure. The shape of the curves are defined by 4 points; the maximum capillary pressure, the half- and a quarter of the maximum capillary pressure and zero capillary pressure at $S_w = 1$ or $S_g = 0$. The results reveal that the effect of capillary pressure is insignificant on the drainage rate. In comparison, the filtrate backflow rate after kickoff is highly affected by capillary pressure curves with maximum capillary pressure greater than 0.1 bar.

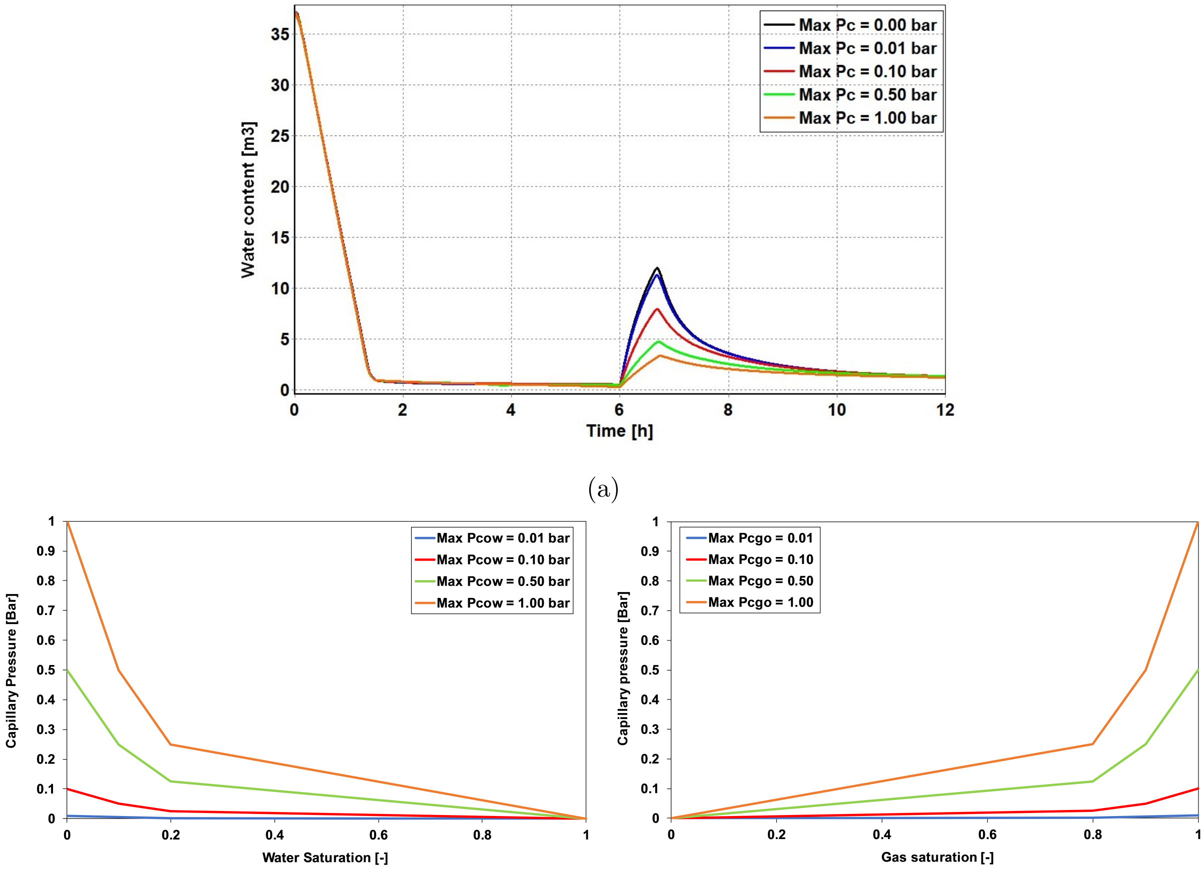

(a)

(b)

(c)

Figure 8.13: a) Water content in the well for different values of maximum capillary pressure and b), c) shape of the capillary pressure curves P_{cow} and P_{cgo}, respectively

By applying the fluid and rock properties given in Table 7.3 and 7.1 to equation (2.16), P_{cow} and P_{cgo} are calculated to be 0.6 bar and 0.02 bar, respectively. As P_{cow} is greater than 0.1 bar, the capillary pressure may affect the results significantly during early production. Figure 8.14 shows how different oil-water capillary pressure curves defined by equation (7.1) affect the water content in the well for the dynamic case.

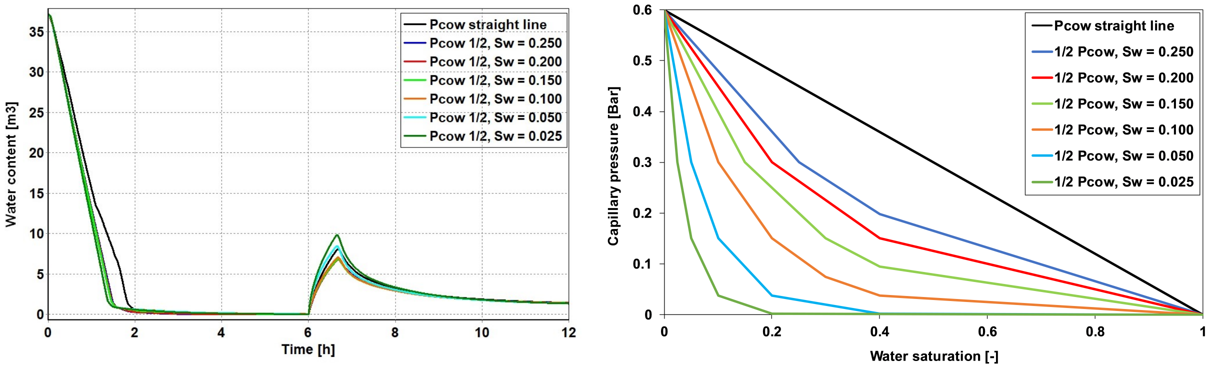

(a) (b)

Figure 8.14: a) Water content in the well for different capillary pressure curvatures for oil and water, shown in b)

$S_{w1/2} = 0.1$ is amongst the capillary curves yielding the minimum mud return rates, thus, the most conservative scenario. In comparison with a straight line gas-oil capillary curve, the same results are obtained in both cases, see Figure 8.15. Thus, for simplicity, a straight line P_{cgo}-curve is used in further simulations. Figure 8.16 shows the effect of capillary pressure with the curves for P_{cow} and P_{cgo} determined in this section.

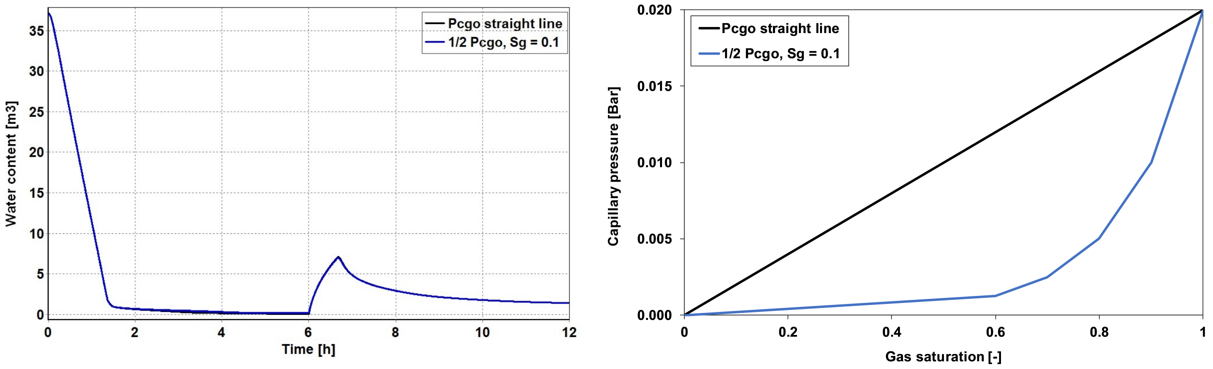

(a) (b)

Figure 8.15: a) Water content in the well for straight line and curved capillary pressure curve for gas and oil, shown in b)

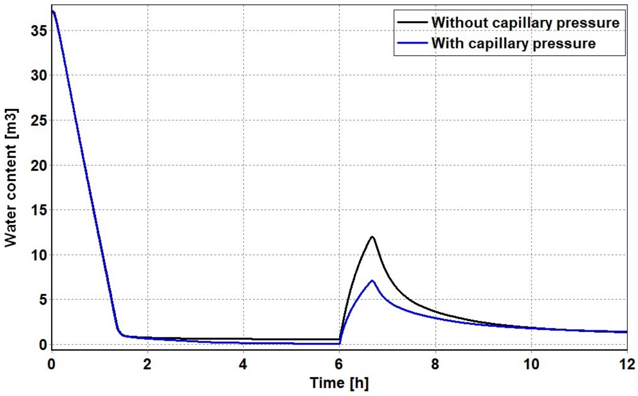

Figure 8.16: Water content in the well with and without capillary pressure

8.3.3 Determination of skin factor

The results from the skin factor study are presented in Figure 8.17, obtained from a standalone ROCX simulation with a reservoir radius of 2000 m and fixed inner- and outer boundary pressures at 300 bar and 415 bar, respectively. The result from the two approaches highlighted in Chapter 7.3 are presented individually in Figure 8.17 b) and c), along with a comparison of the two approaches provided in a).

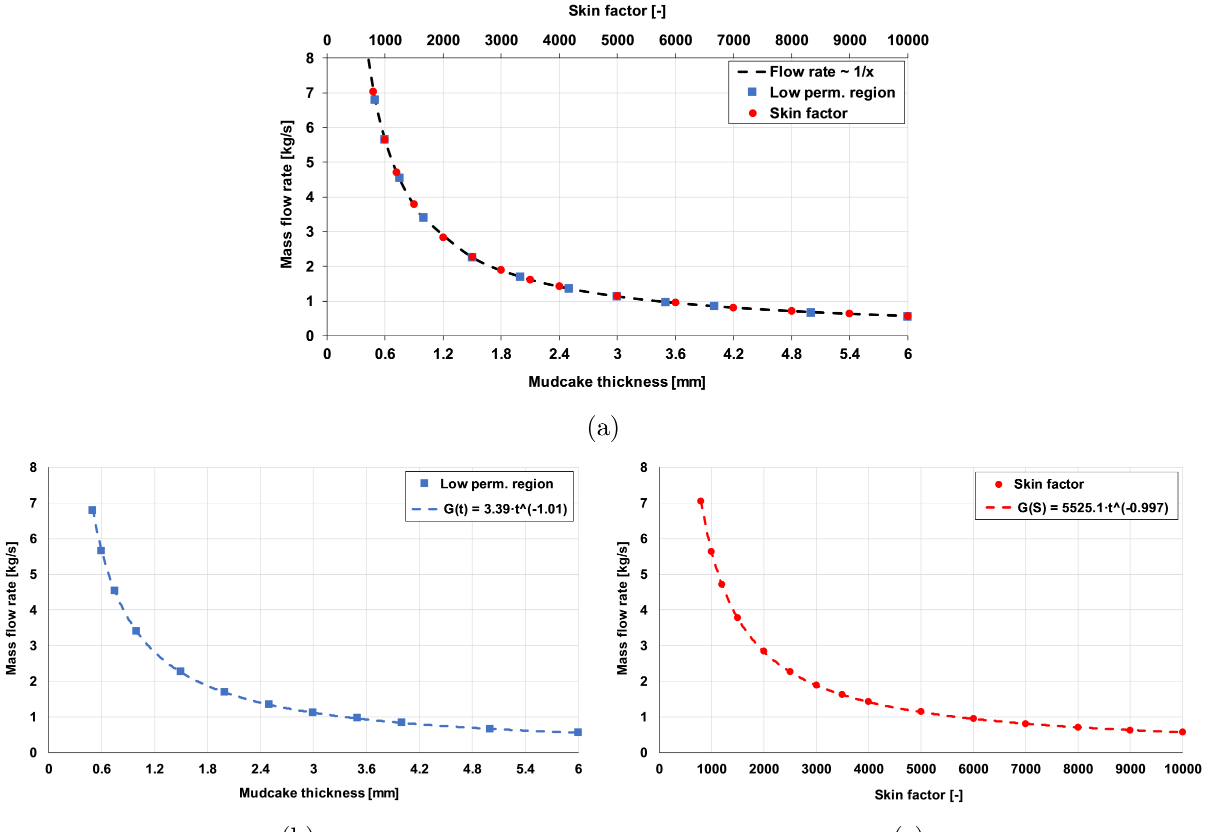

(a)

(b)

(c)

Figure 8.17: Steady-state production rate as a function of skin factor and mud cake thickness

In Figure 8.18, the two horizontal axes in Figure 8.17 a) are plotted against each other and compared with Hawkins' equation (2.19).

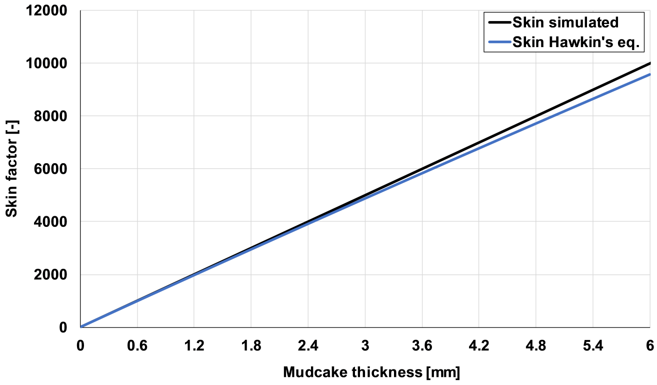

Figure 8.18: Simulated relation between skin factor and thickness of a low permeable region plotted together with Hawkins' equation

In comparison, Hawkins' relation is roughly linear for thin layers of very low permeability, thus, the simulated result is in good agreement with the theory. Based on these results, the mud cake of thickness 3 mm and permeability 0.001 mD is modeled with a skin factor of 5000 in further simulations.

8.3.4 Sensitivity study on mud density, skin factor and damaged zone length

As the mud drainage is completely gravity-driven, a higher mud density increases the drainage rate significantly, see Figure 8.19 a). Figure 8.19 b) reveals that the drainage rate is also highly affected by the skin factor. Using Hawkins' equation (2.19), the skin factors are presented with corresponding mud cake thicknesses and permeabilities in Table 8.1. The results from the sensitivity on damaged zone length, presented in Figure 8.19 c), show an insignificant effect.

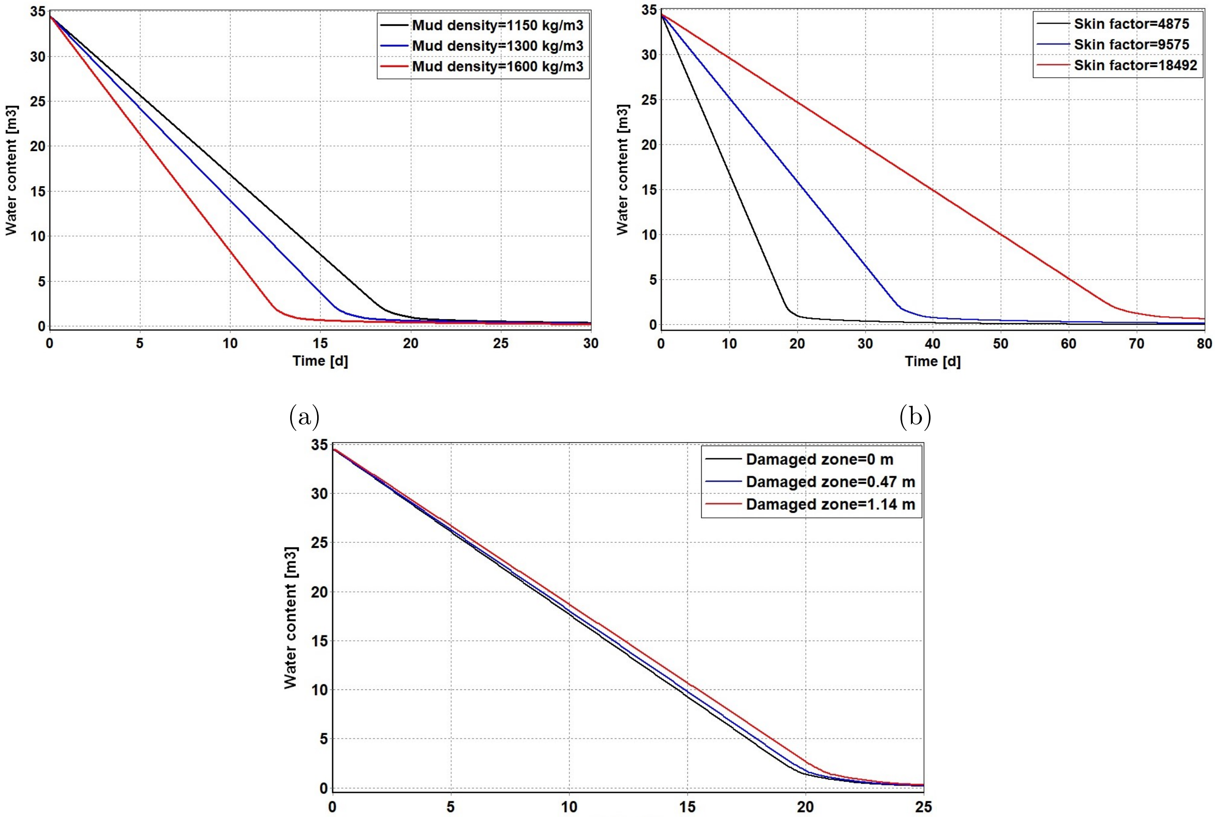

(a) (b)

(c)

Figure 8.19: Water content in the well for different a) mud densities, b) skin factors and c) damaged zone lengths

Table 8.1: Skin factors with corresponding mud cake thicknesses- and permeabilities

Skin factor	Mud cake thickness [mm]	Mud cake permeability [mD]
4875	3	0.001
9575	6	0.001
18492	12	0.001
9575	3	0.00051
18492	3	0.00026

Figure 8.20 shows the results from the sensitivity on skin factor after kickoff, revealing that both the well cleanup- and dewatering are highly sensitive to remaining mud cake amounts. The cases are simulated with a fully open production choke onshore, thus, no constraints on the flow rate. The black dots in Figure 8.20 represent the points in time for each case where the pig speed exceeds 1 m/s, which is undesirable. The dotted lines in Figure 8.20 b) predict the dewatering rate with a PID-controller constraining the flow rates, indicating an even longer dewatering period. Figure 8.20 a) shows that no remaining mud cake yields the most efficient dewatering. Regarding the well cleanup, Figure 8.20 a), the point of velocity increase indicates no further cleanup below this point. The most efficient cleanup is achieved with no remaining mud cake, due to high initial flow rates compared to the other cases, see Figure 8.20 c). In further simulations, the mud cake is assumed completely removed. The skin factors used in the sensitivity study above, along with the corresponding mud cake thickness- and permeability, are presented in Table 8.2.

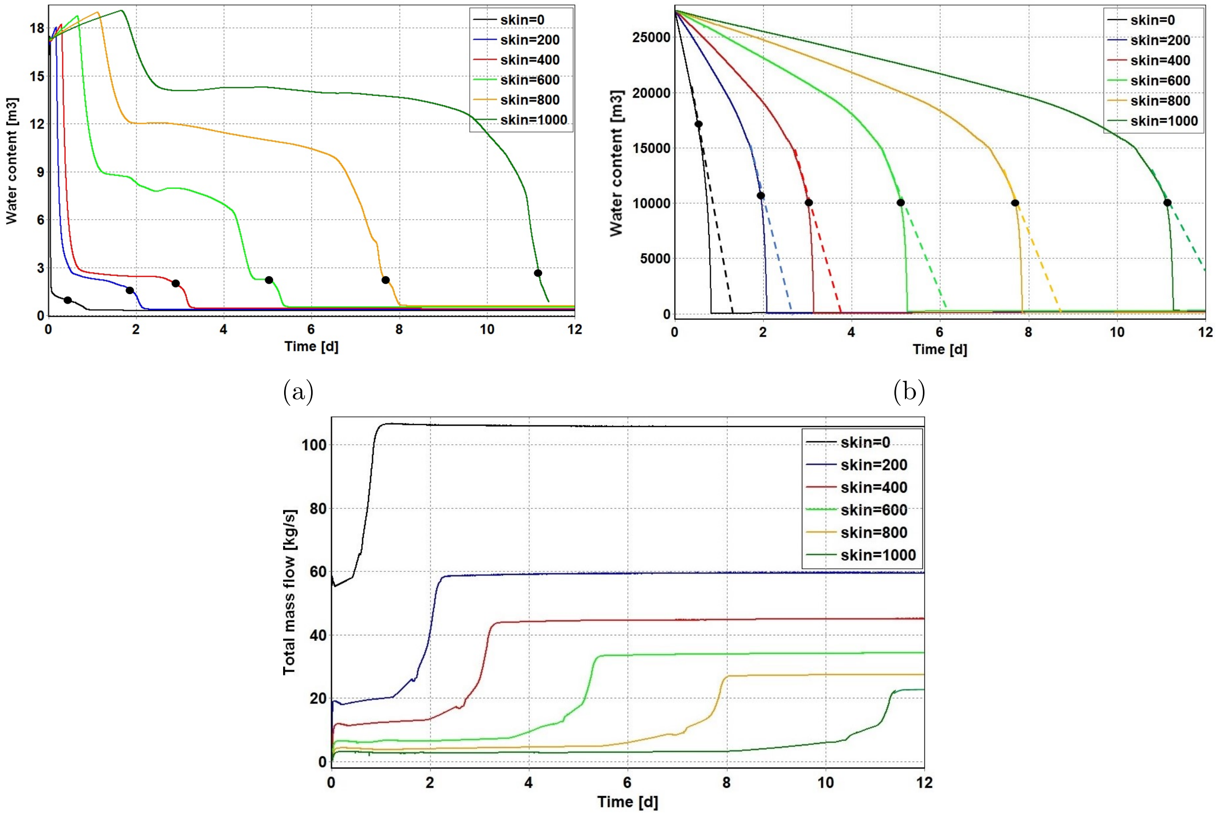

(a) (b)

(c)

Figure 8.20: Water content in the well during a) well cleanup and b) dewatering of trunkline, and c) total mass flow rate above the perforation zone for different remaining mud cake thicknesses

Table 8.2: Skin factors with corresponding mud cake thicknesses- and permeabilities

Skin factor	Mud cake thickness [mm]	Mud cake permeability [mD]
1000	0.6	0.001
800	0.48	0.001
600	0.36	0.001
400	0.24	0.001
200	0.12	0.001

8.4 Tuning of PID controller

Figure 8.21 shows how a proportional controller regulates the flow for different amplification factors. It can be observed that the proportional controller does not manage to meet the setpoint requirement. Adding the integral action, the resulting PI controller manages to maintain a flow rate of 0.22 m^3/s during the entire dewatering period for K_c = -0.01 and τ_i = 5 s, see Figure 8.22. Hence, these values are used in further simulations.

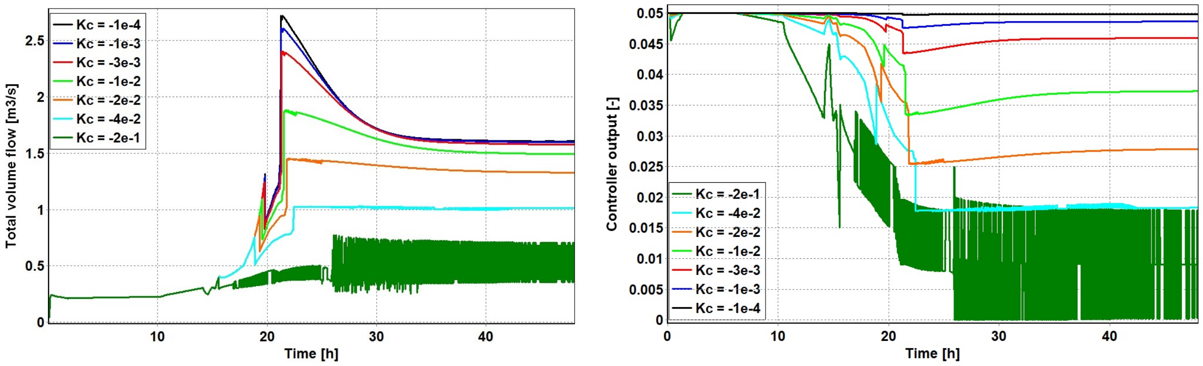

(a)

(b)

Figure 8.21: a) Flow rate recorded by the transmitter and b) output from the PID controller for different amplification factors

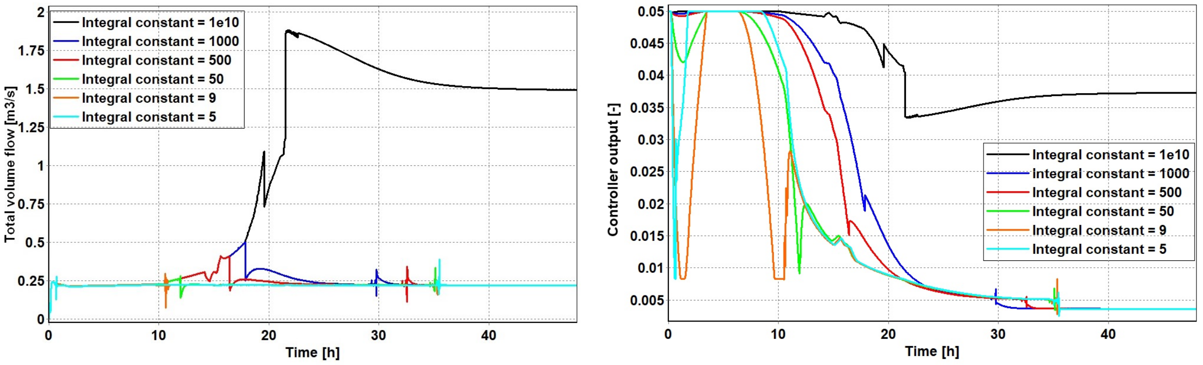

(a)

(b)

Figure 8.22: a) Flow rate recorded by the transmitter and b) output from the PID controller for different integral constants

Figure 8.23 shows the difference in pig velocity and dewatering time with and without the PI controller. In the case without a PI controller, the pig velocity is observed to increase rapidly as the hydrostatic pressure in the trunkline gradually decreases toward shore. By constraining the volume flow through the production choke utilizing the PI controller, the dewatering time increases accordingly. Figure 8.23 b) reveals a required dewatering time of 36.5 hours.

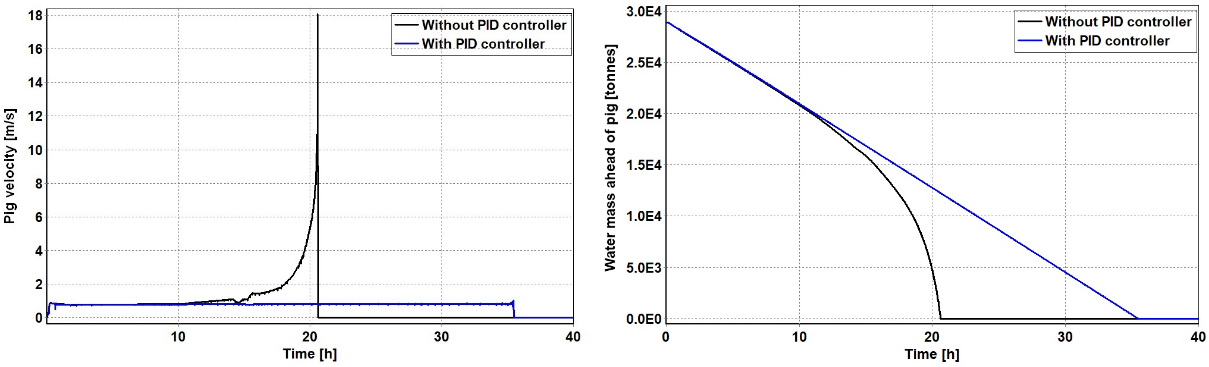

(a) (b)

Figure 8.23: a) Pig velocity with and without controller and b) water mass ahead of pig with and without controller

8.5 Well suspension

The results in Figure 8.24 reveal that a suspension period of 7 days is required to achieve a pressure drop across the wellhead greater than 20 bar.

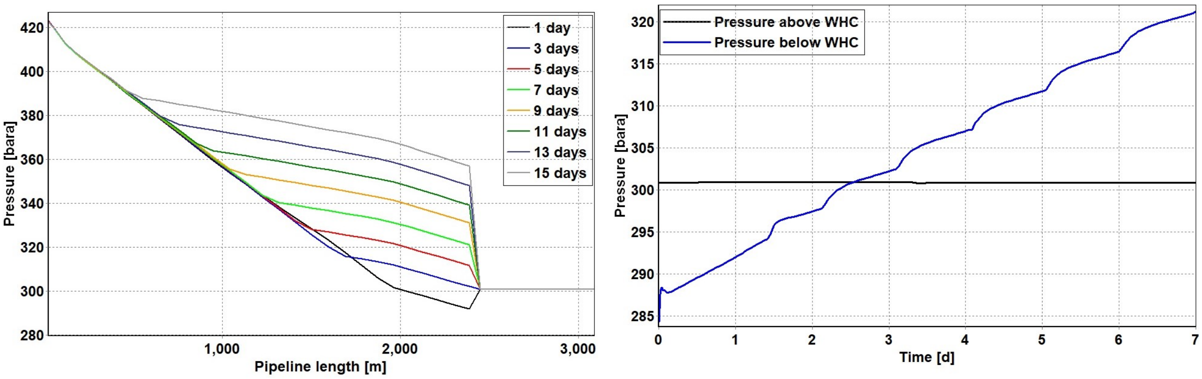

(a) (b)

Figure 8.24: Pressure drop across the wellhead for a) different suspension periods and b) 7 days of suspension

The corresponding drainage mass after 7 days is 13 719 kg, constituting 13 516 kg of mud and 203 kg of brine. This leaves 7 231 kg mud and 17 567 kg brine in the well, see Figure 8.25. Based on these values, the average drainage rate is calculated to be 1960 kg/day. Figure 8.25 shows the drainage from the well-side, while Figure 8.26 illustrates the drainage on the reservoir-side, obtained from Floviz.

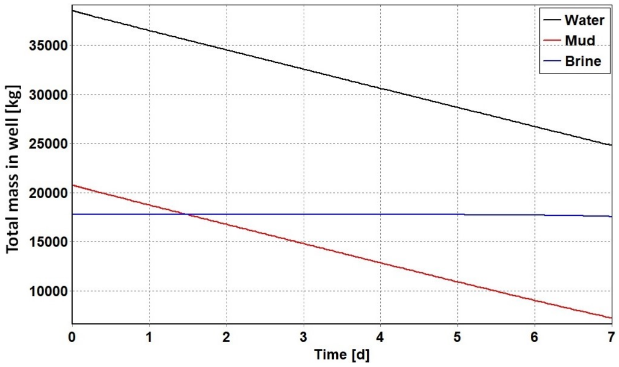

Figure 8.25: Drainage of drilling- and completion fluids in the well during the suspension period

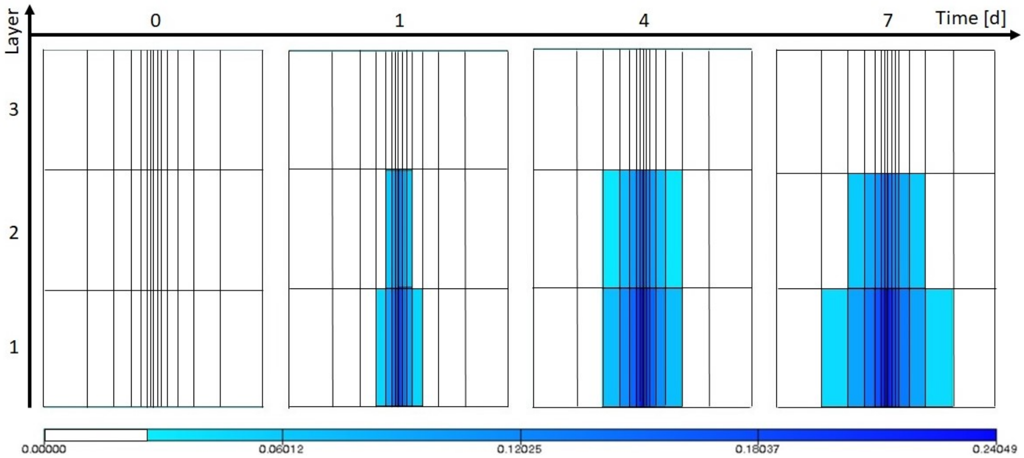

Figure 8.26: Filtrate saturation in the 7 cells closest to the wellbore during the suspension period

8.6 Well cleanup, dewatering and early production

Figure 8.27 a) reveals that the well is successfully unloaded and the drilling- and completion fluids are transferred from the infield flowline into the trunkline after approximately 1 hour. By comparing the mud and brine masses in Figure 8.27 a) and b), it can be observed that all the mud and brine remain in the trunkline during the dewatering simulation. During the 20 first days of production, all the drilling- and completion fluids are produced out of the trunkline.

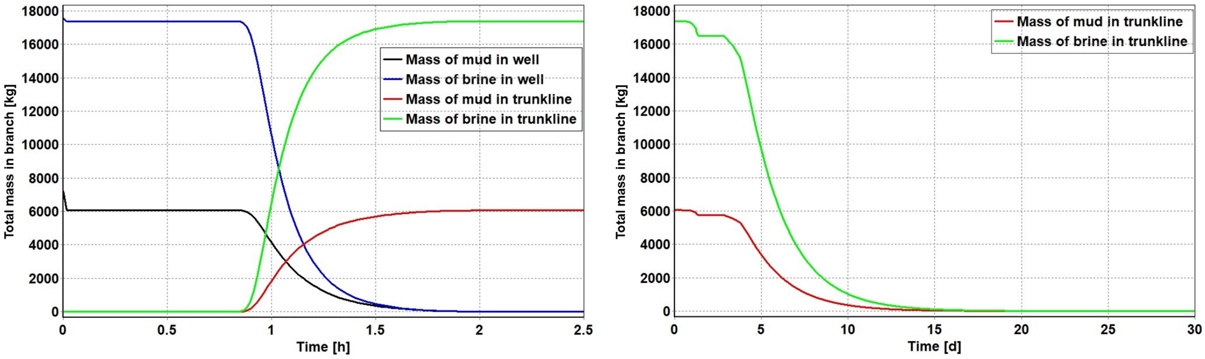

(a) (b)

Figure 8.27: Mass of mud and brine in the well (included infield flowline) and trunkline during a) first 2.5 hour of dewatering b) first 30 days of early production

Furthermore, it is observed from Figure 8.27 a) that some mud and brine are lost to the reservoir prior to well unloading. The resulting losses are quantified in Table 8.3, along with the drained masses during well suspension. The results in the table reveal that the total amount of the drilling- and completion fluids injected into the reservoir is approximately 15 tonnes.

Fluid	**Drained during suspension [kg]**	**Lost during kickoff [kg]**	**Total mass [kg]**
Mud	13 516	1 171	14 687
Brine	203	181	384
Total	13 719	1 352	15 071

Table 8.3: Masses of drilling- and completion fluids injected into the reservoir during suspension and well kickoff

Figure 8.28 a) illustrates how the front of the drilling- and completion fluids propagates through the infield flowline. The initial mud distribution in the trunkline after dewatering, and the mud displacement during early production, are illustrated in Figure 8.28 b).

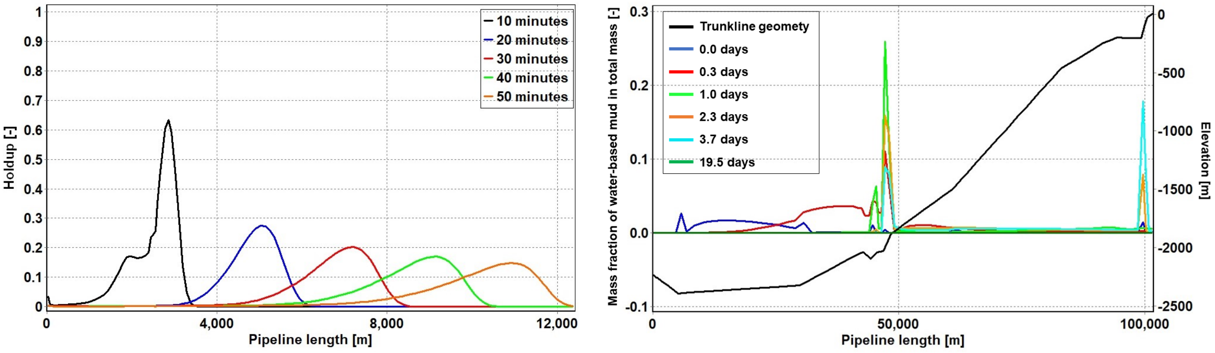

(a) (b)

Figure 8.28: a) Drilling- and completion fluid front propagating through the infield flowline and b) initial mud distribution in the trunkline after dewatering and mud displacement during early production

Figure 8.29 shows how the filtrate is produced out of the reservoir from the well-side, while Figure 8.30 illustrates the reduction of the filtrate on the reservoir-side, obtained from Floviz. Some key values are extracted from Figure 8.29 b) and presented in Table 8.4.

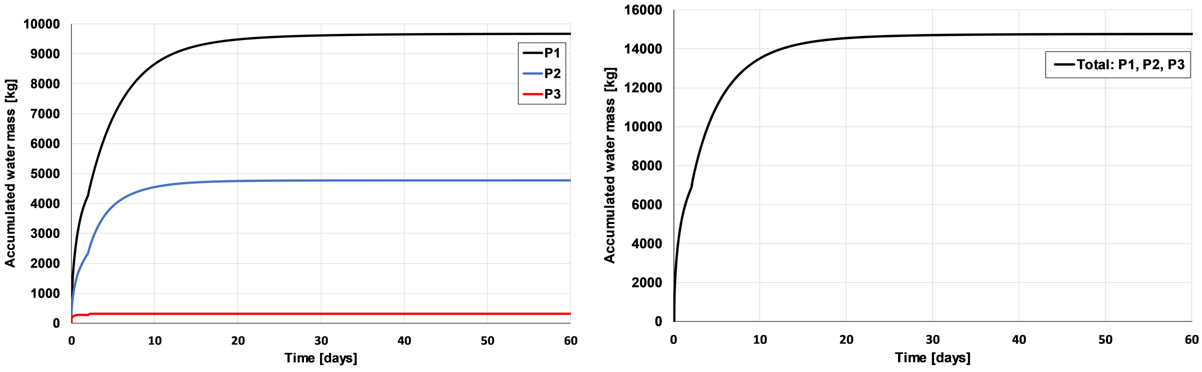

(a) (b)

Figure 8.29: a) Accumulated filtrate backflow over each near-well source and b) total accumulated filtrate backflow over all three near-well sources

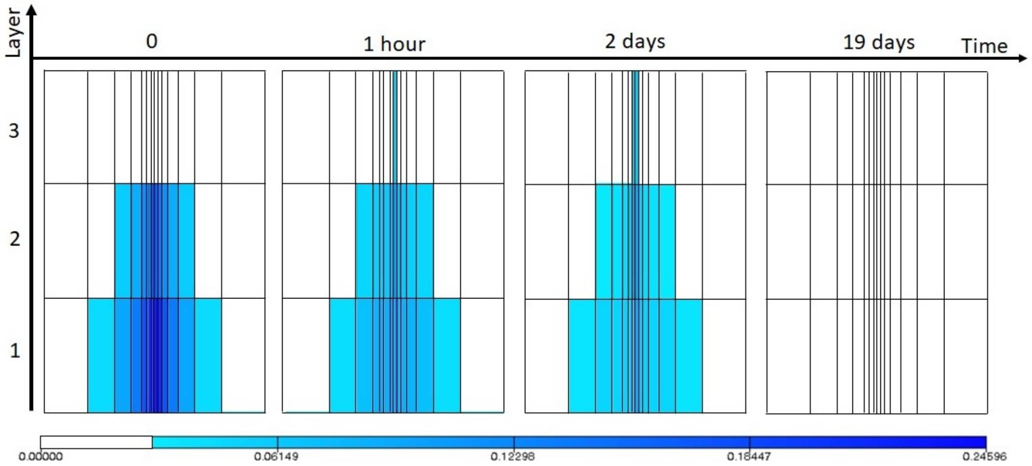
Layer
3
2
1
0
1 hour
2 days
19 days
Time
0.00000
0.06149
0.12298
0.18447
0.24596

Figure 8.30: Filtrate saturation in the 7 cells closest to the wellbore during dewatering and early production

Time	Accumulated filtrate flow [kg]
1 hour	1500
2 days	6887
19 days	14 516
30 days	14 703
60 days	14 760

Table 8.4: Filtrate backflow from the reservoir during dewatering and early production

Figure 8.31 illustrates how the amount of filtrate in the reservoir decreases with 98% from the initial value of 15 tonnes. The remaining 2% constitute a mass of 311 kg which is still present in the reservoir after 60 days of production.

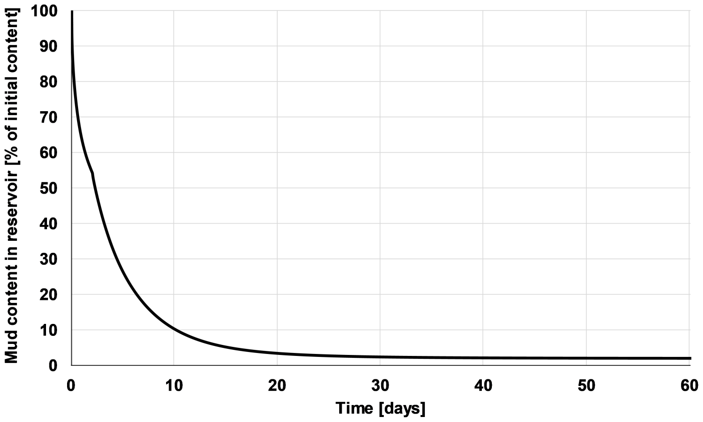

Figure 8.31: Remaining filtrate content in the reservoir during dewatering and well cleanup

9 Discussion

The key findings from Chapter 8 are summarized in Table 9.1 below. A discussion of the results is provided in this chapter.

Table 9.1: Results summary

Reservoir radius	2000 m
Number of vertical grid points in ROCX	3
Number of radial grid points in ROCX	20
Number of angular grid points in ROCX	1
Minimum number of sections per pipe in OLGA	3
Maximum section length in OLGA	100 m
Corey exponent	2
P_{cow}	0.6 bar
P_{cgo}	0.02 bar
Skin factor	5000
Amplification factor PI	-0.01
Integral factor PI	5 s
Required well suspension time	7 days
Total drained mass during well suspension	13 719 kg
Average drainage rate	1960 kg/day
Loss of drilling- and completion fluids during well kickoff	1 352 kg
Dewatering time	36.5 h
Production affected by mud and brine	20 days
Production affected by filtrate	19-30 days

9.1 Near-wellbore radius

The simulation results obtained in Chapter 8.1 are in good agreement with the theory presented in Chapter 2.5 regarding ideal reservoir flow. The pressure distributions show a linear behavior with a semi-logarithmic axis, and the radius of investigation increases with $\sqrt{t}$, as illustrated in Figure 8.2 a). The sudden "jumps" in the simulated curve indicates that the pressure disturbance reaches a new cell midpoint where the pressure is calculated. Hence, the first point after each "jump" shows how the pressure disturbance propagates further into the reservoir. It is observed that the simulated results fit the theoretical curve if the radius of investigation is defined at the point where the initial pressure has decreased by 0.2 bar. If the radius of investigation is defined by a smaller ΔP, on the other hand, the radius will propagate faster, as shown in Figure C.1 a) and b) in Appendix C. In practical applications, ΔP is defined as the smallest measurable pressure drop. In any case, it is observed that the simulated radius of investigation increases by $\sqrt{t}$, which is in correspondence with the theoretical curve.

To fulfill the assumption of an infinite acting reservoir throughout long simulation periods, a large reservoir is required, see Figure 8.1 and Figure 8.2 b). As larger reservoir radii yield higher CPU times, the alternative solution using a smaller reservoir with pressure support at the outer boundary is desirable. Due to the transient behavior associated with the cleanup and dewatering procedures, it is desirable with an infinite acting reservoir during the first 48 hours of simulation, in order to capture these transients. Based on the results in Figure 8.2 a), a reservoir radius of 2000 m is a conservative choice.

Figure 8.3 and Figure 8.4 a) confirms that a reservoir radius of 2000 m is infinite acting for at least 2 days, as the pressure disturbance has not reached the outer wall/boundary by this time. Figure 8.3 a) shows that when the reservoir is no longer infinite acting, the pressure will decline towards the wellbore pressure as the closed tank drains. If a pressure support is applied at the outer boundary the system will reach a steady-state condition with a constant production rate shown in Figure 8.4 c). From Figure 8.4 b) and c), it is observed that the small reservoir modeled as a closed tank differs from the infinite acting reservoir solution, whilst the small reservoir with pressure support is close to the infinite acting solution. Hence, a reservoir of 2000 m with pressure support is considered to produce reliable results.

9.2 Grid sensitivity study

Prior to investigating the effect of the pressure drop across the glass plug, a grid study was already conducted. In the first grid study, the initial reservoir pressure in the different numerical layers in vertical direction was obtained based on a mid-zone pressure at 415 bar in the perforation section. A fixed pressure drop along the vertical perforation section yields different pressures in the upper reservoir layer for different gridding in z-direction, causing different pressure drops across the glass plug for different number of grid blocks in z-direction. The first grid study is attached in Appendix D.

In the modified grid study, the initial reservoir pressure was defined based on a fixed pressure in the upper reservoir grid cell, not the middle, as defined in the first grid study. Consequently, the pressure drop across the glass plug is independent of the reservoir gridding in vertical direction. In addition, the option FASTWALL was used in the second grid study during the stabilization case to ensure a steady-state condition in the well was obtained prior to running the dynamic case.

9.2.1 Pressure drop effect across the glass plug

The effect of negative- and positive pressure drops across the glass plug was assessed in order to verify that the pressure drop could have affected the results in the first grid study. A few bar pressure drop across the glass plug shows to have a significant effect on the drainage, shown in Figure 8.5. The instabilities introduced for certain pressure drops may have caused the instabilities observed in the first grid study, see Figure D.1 c), D.2 b) and D.3 b) in Appendix D. Furthermore, the delayed drainage startup observed in Figure D.4 a) in Appendix D, may also have been a result of a negative pressure drop present across the glass plug. A negative pressure drop yields an upwards flow initially, before the pressure is equalized and the drainage commences under the influence of gravity only. However, an unexpected delayed drainage appears for certain negative pressure drops. In the case of a positive pressure drop, an initial downward directed flow is observed before the pressure is equalized, and the gravity-driven drainage commences.

In conclusion, the pressure drop may have affected the first grid study significantly. Thus, the modified grid study was highly necessary. Figure 8.5 c) verifies that zero pressure drop, used in the modified grid study, promotes a stable drainage with no delay. The same applies to small negative- and positive pressure drops.

9.2.2 Vertical gridding in ROCX

In comparison with the first grid study, oscillating behavior also appears in the modified grid study for a certain number of grid blocks in vertical direction. The drainage rate is more or less unchanged, however, the deviations in filtrate backflow observed in the first grid study in Figure D.1 a) in Appendix D are strongly diminished in the modified grid study. Still, no drainage is commenced for one grid block in vertical direction. With multiple grid blocks present, on the other hand, the gas can flow out from one grid block while the mud flows into another grid block, see Figure F.4 in Appendix F. In conclusion, it is highly necessary with more than 1 grid block. For simplicity, 3 grid blocks were chosen.

9.2.3 Radial gridding in ROCX

As the determined reservoir radius is relatively large compared to the small drainage volume of mud, it is highly beneficial with a fine gridding close to the wellbore to capture the inflow of mud and outflow of filtrate. The results from the sensitivity on a uniform grid in radial direction reveal that a large number of grid blocks in radial direction are required in order to capture the drainage with reasonable accuracy. In comparison, a logarithmic grid manages to capture the physics with a small number of grid blocks. As the computational time is strongly affected by the gridding in radial direction, it is highly recommended to choose as few grid blocks as possible. Consequently, grid refinement was conducted until oscillations were observed.

Stability is preserved for grid blocks up to 30, where oscillating behavior is initiated. For grid blocks more than 50, stability is obtained again. However, in-between the range of 30 and 50 grid blocks, stability is observed in the cases of 35 and 40 grid blocks. Few cases with many grid blocks are conducted, due to immense CPU-time. Hence, the stability observed for grid blocks more than 50 may be arbitrary. Consequently, a more comprehensive grid study for high number of grid blocks in radial direction should be conducted. As many grid blocks in radial direction are undesirable in terms of CPU-times, such a study is irrelevant for the scope of work in this thesis.

In comparison with the results obtained in the first grid study, no major deviations are observed. An underestimation in filtrate backflow is still observed for 5 and 10 grid blocks. The filtrate backflow increases with an increasing number of grid blocks. A possible explanation could be due to the grid refinement near the well for an increasing number of grid blocks. Consequently, the flushing of one grid block filled with filtrate is more efficient the smaller the grid block is, due to a smaller flushing volume respectively. During production, the oscillation occurrence decreases with grid refinement. However, as the simplified case does not account for the flow control during dewatering, nor includes the trunkline to shore, these conditions may affect the early production. Thus, no further considerations are required, as this will most likely not have any significant influence on the objective of this thesis.

9.2.4 Angular gridding in ROCX

Large deviations in the drainage rate for different gridding in angular direction are observed in the first grid study, see Figure D.4 a) in Appendix D. However, multiple grid blocks in angular direction all have in common a delayed drainage startup. Prior to considering the pressure drop effect, the result of neglecting the three-dimensional effects in the reservoir was investigated, see Figure D.4 b) in Appendix D. Neglecting the angular flow in the reservoir, by simply setting the angular permeability to zero in the cases with multiple grid blocks, results in a coincidence with the graph for one grid block. Thus, the delay was considered to be an effect of angular flow in the reservoir, counteracting the vertical flow resulting in immediate drainage initializing.

The modified grid study, on the other hand, does not support the theory of angular flow counteracting the vertical flow, preventing an immediate drainage startup. The solutions for 2 and 8 grid blocks coincides with the solution for 1 grid block, indicating no counteracting flow behavior. Hence, neglecting three-dimensional effects in the reservoir, by choosing 1 grid block, is a reasonable assumption. The reason for the unexpected delayed drainage startup observed for 4 grid blocks is unclear. More simulations on gridding in angular direction should be conducted to investigate this observation. However, as an increase of one grid block in angular diction requires three more near-well sources in OLGA, a more comprehensive grid study in angular direction would be extremely time-consuming. This may instead be a topic for further work.

9.2.5 Gridding in OLGA

The results from the grid study in OLGA exhibit oscillating behavior for a fine grid, see Figure 8.10 b). As the flow rate in this case oscillates around the same drainage rate as obtained for the stable cases, no effect of the instabilities is observed on the drainage in Figure 8.10 a). The finest grid yielding a stable behavior is obtained for a minimum of 3 sections per pipe and a maximum section length of 100 m, and was thus chosen as the desired gridding. Hence, the 1780 m inclined well section is divided into 20 sections and the 500 m upper vertical section is divided into 3 sections. Furthermore, the 150 m spool and the 9850 m infield flowline are divided into 3 and 98 sections, respectively. Regarding the gridding in the 101 617 m long trunkline, a much coarser grid is utilized. However, grid refinement is conducted in areas of large local elevation differences.

9.3 Sensitivity studies on reservoir parameters

As no experimental core data are obtainable for this specific reservoir, relative permeability- and capillary curves were estimated. Furthermore, a skin factor was determined, and sensitivity on different mud densities, skin factors and damaged zone lengths was conducted, to assess their effect on the mud invasion and well cleanup.

9.3.1 Relative permeability curves

The results from the sensitivity study on Corey exponents for fixed endpoints reveal an insignificant effect on the drainage rate. However, some deviations are present during the flushing. It is observed from Figure 8.11 b) that straight line relative permeability curves yield an overestimated flushing rate, compared to the curved curves.

When varying K_{rwoc} for different Corey exponents, dramatic changes in the drainage rate were observed for small changes in K_{rwoc}. Consequently, a sensitivity on K_{rwoc} was conducted, see Figure 8.12. The results reveal that Corey exponents 3 and 4 are highly sensitive to changes in K_{rwoc}, whilst Corey exponent 2 remains unchanged. Instabilities occur for certain values of K_{rwoc} for Corey exponent 3 and 4. To ensure that the stability obtained for the value of K_{rwoc} used for Corey exponents 3 and 4 in Figure 8.11 was not a coincidence, Corey exponent 2 constitute a safe choice. Furthermore, as the results in Figure 8.11 show an insignificant effect for different Corey exponents, 2 was chosen in further simulations.

9.3.2 Capillary pressure curves

Figure 8.14 shows that the straight line P_{cow}-curve solution differs from the other solutions late in the drainage period. This is due to instabilities, which give rise to oscillations in the total mass flow rate during drainage. The 4 next solutions with half-saturations from 0.25 to 0.1 yields approximately the same result with low filtrate backflow during early production. The steeper curvatures with half-saturation 0.05 and 0.025 produce higher filtrate backflow from the reservoir. The magnitude of P_{cgo} is very small compared to P_{cow}, because the interfacial tension between gas and oil is much less than for oil and water, see Table 7.1. Hence, the shape of the P_{cgo}-curve does not matter as illustrated in Figure 8.15.

Figure 8.16 shows that the drainage rate is unaffected by the capillary pressure, however, the amount of drained mud differs. With capillary pressure, all the mud in the well drains into the reservoir whereas with no capillary pressure a small amount remains in the well. As observed earlier, filtrate returns slower from the reservoir when capillary pressure is accounted for.

9.3.3 Determination of skin factor

Figure 8.17 b) and c) show that the flow rate decrease proportionally with one over the mud cake thickness, and one over the skin factor approximately. Hence, the scale of the horizontal axis can be adjusted such that the curves for skin and mud thickness coincide, as done in a). Consequently, the skin factor at the upper horizontal axis must correspond to the mud cake thickness at the lower horizontal axis, as the simulated mass flow rates are equal in both cases. Thus, the simulated relation between mud cake thickness and skin factor is linear, as shown in Figure 8.18.

9.3.4 Sensitivity study on mud density, skin factor and damaged zone length

During the suspension, the mud density, mud cake properties and the length of the damaged zone were considered to be the variables of most influence on the drainage rate. As expected, a higher mud density increases the drainage rate. This is because a higher mud density implies a greater density difference between mud and reservoir gas, which is the key parameter affected by gravity during the suspension.

Regarding the skin factor, the results in Figure 8.19 b) reveal a strong influence on the drainage rate. As the skin factor constraints the flow between the reservoir and the wellbore, lower drainage rates are observed for higher skin factors. By representing the skin factors as mud cake thicknesses, the drainage period seems to increase close to proportionally to the thickness. A doubling in mud cake thickness results roughly in a twice as long drainage period. The contribution of a damaged zone, shown in Figure 8.19 c), on the other hand, shows an insignificant effect on the drainage rate. This means that the amount of mud lost to the formation during drilling of the well does not significantly affect the drainage period. Hence, the damaged zone is neglected in further simulations.

Figure 8.20 a) and b) reveals that both the well cleanup- and dewatering operations are highly sensitive to remaining mud cake amounts. The trend shows an increased efficiency in the aforementioned operations for decreasing skin factors after kickoff, due to increased initial flow rates in c). The reduction of drilling- and completion fluids in the well after the dots marked in Figure 8.20 a), is due to a flushing caused by high pig velocities. As the pig velocity will be constrained by a PID controller later on, the last flushing will not take place.

9.4 Tuning of PID controller

Based on the results presented in Figure 8.21 and Figure 8.22, a PI controller with K_c = -0.01 and $\tau_i = 5$ is chosen to regulate the system. In general, it is desirable to have a fast responding system, hence a large amplification factor. However, with too large amplification factors, the controller tends to easily overshoot and oscillations may occur. If the amplification factor is chosen even higher, the oscillations will escalate and the system becomes unstable, seen from Figure 8.21 for the largest amplification factor. For K_c = -0.04 the PID controller manages to maintain a constant flow rate after 23 hours, but with offset from the desired setpoint value of 0.22 m^3/s. By extending to a PI controller, this offset can be removed by the integral term. Hence, new simulations with K_c = -0.04 and different integral constants were conducted, see Figure E.1 in Appendix E. The results show that the offset is removed for smaller integral constants, but this also causes instabilities. To avoid these instabilities the amplification factor must be reduced. Therefore K_c is set to -0.01 and the same procedure is repeated. The results for different integral constants are plotted in Figure 8.22. This time the desired flow rate is maintained stable at approximately 0.22 m^3/s throughout the whole trunkline for $\tau_i = 5$.

Figure E.2 in Appendix E represents the same data as in Figure 8.23 a), but with different scaling on the vertical axis. Small drops in pig velocity are observed, which the PI controller does not manage to remove. However, this is considered to not affect the conditions in the reservoir which is the main concern in this study. As control engineering is not a central part of the scope of this thesis, further parameter tuning utilizing more comprehensive tuning techniques are not conducted.

9.5 Well suspension

A 20 bar pressure drop across the wellhead choke will correspond to a 20 bar pressure drop across the mud cake when the wellhead choke is opened. Due to the large gas volume in the infield flowline, the gas pressure at the top of the well will become equal to the gas pressure in the infield flowline when the choke is opened. As the pressure drop across the well fluid column is constant, the pressure decreases accordingly at the bottom of the well, resulting in an equal pressure drop across the mud cake. It is assumed that a 20 bar pressure difference between the reservoir and the wellbore will be sufficient to collapse the mud cake. This value is rather arbitrary chosen and should be verified by experiments.

The results revealed that a suspension period of 7 days is required to achieve the desired pressure drop of 20 bar across the wellhead choke. During the 7 days of drainage, the drainage rate remains constant, resulting in a linear reduction of drilling- and completion fluids in the well as seen from Figure 8.25. Most of the drained liquids are mud, and only small amounts of brine enter the reservoir. As the drilling fluid option is not supported by ROCX, the brine is modeled as filtrate with filtrate properties. This is not a major concern as the properties of brine and filtrate are quite similar, besides, only small amounts of brine invade the near-wellbore region.

Figure 8.26 shows that most of the mud is drained into the bottom and middle near-well sources, P1 and P2 respectively. Figure F.4 in Appendix F confirms that reservoir gas flows into the wellbore through the upper near-well source, while mud drains into the two lower near-well sources. Filtrate penetrates longest into the reservoir in the bottom layer, and after 7 days the filtrate is present in the 6 cells closest to the well. The center of the sixth cell is 1.35 m from the wellbore wall, as shown in Figure F.3. As expected, the filtrate saturation is highest in the region near the wellbore and gradually decreases in radial direction.

Figure F.1 and Figure F.2 illustrates how the gas propagates upwards in the well before it reaches the gas pocket at the kickoff after 22 hours. After 2 days, a constant holdup of 0.9 is obtained along the lower part of the well. The holdup stays fixed at 0.9, while the well drains, see Figure F.2 e) and f). Bubble flow occurs in the whole perforation zone as the gas starts to propagate upwards in the well after 1 hour. Shortly after, the flow regime in the bottom of the perforation zone shifts to annular. Stratified flow is present in the rest of the well, except the top vertical section where the flow regime is annular.

9.6 Well cleanup, dewatering and early production

The mud loss observed from Figure 8.27 a), can be explained by the skin factor modeling the mud cake at the inner wellbore wall. Both the wellhead choke opening and the skin factor changes instantly as the dewatering case restarts from the well suspension case. The wellhead opening goes from closed to 20% open, and at the same time the skin factor reduces from 5000 to 0. The instant reduction in skin factor reflects that the mud cake collapses at the wellbore wall. In reality, the mud cake will not collapse before the pressure in the well becomes sufficiently lower than the reservoir pressure. In the simulations, on the other hand, the skin is removed manually at a given time independent of pressure differences in the well and the reservoir. For a short time period (less than 60 seconds), the pressure is higher in the well than in the reservoir. Hence, with no skin present, this causes high flow rates from the well to the reservoir before the flow changes direction and the well unloads. This could have been avoided by reducing the skin factor 1-2 minutes after the wellhead choke is opened.

Figure G.1 in Appendix G illustrates different stages in the combined well cleanup and dewatering procedure. From Figure G.1 b), it can be observed that the well unloading commences after 2 minutes. After approximately 10 minutes, all the drilling- and completion fluids have entered the infield flowline, as shown in Figure 8.28 a). The holdup front of the fluids smears out as it travels through the infield flowline, and accumulates in the deepest part of the trunkline. The flow rates are rather low during the dewatering procedure as the pig travels with a constant velocity of 0.8 m/s, hence the mud front does not follow the pig. The accumulation of drilling- and completion fluids can be seen from the initial holdup curve in Figure 8.28 b). As the choke at the onshore LNG plant is opened during early production, the flow rates increase and the mud starts to displace in the trunkline. Figure 8.28 b) reveals that mud accumulates in the dip in the middle section of the trunkline, and in the bottom of the uphill section close to onshore. After approximately 20 days, all the mud is produced out of the trunkline as seen from Figure 8.27 b) and Figure 8.28 b). As the trunkline profile is very simplified in this study, the mud displacement throughout the trunkline may be different for a more detailed pipeline profile. Hence, investigations of different ramp-up strategies to effectively produce the drilling- and completion fluids out of the trunkline are addressed as further work.

Figure 8.29 and Figure 8.30 shows that it takes about the same time to flush the reservoir for filtrate. Most of the filtrate follows the first production during the 36.5 hours of dewatering. After 19 days of production, the filtrate saturation in all reservoir cells is less than 1%, which is considered insignificant. The flow rates of filtrate into the well after this point are very low, hence the curve in Figure 8.29 b) flattens. Table 8.3 reveals that only 187 kg of filtrate is backflowed from 19 to 30 days. During the second month of production, the backflowed amount is insignificant. Consequently, the reservoir is considered fully flushed and the trunkline fully emptied for drilling- and completion fluids after approximately 20 days.

Figure 8.31 shows that a small amount, approximately 2%, of the injected drilling- and completion fluids never return from the reservoir. This is in good agreement with observations done on the reservoir side, as small saturations of filtrate in the reservoir is still present. It should be stressed that the accumulated curves in Figure 8.29 and Figure 8.31 are produced by applying the trapezoid rule on the flow rates over the near-well sources, as no accumulated flow variable over the near-well sources is implemented in OLGA. It is highly recommended that such a variable is implemented by the software developer.

10 Conclusion

The aim of this thesis was to investigate the contingencies of combined well cleanup and dewatering to shore on Block 2 offshore Tanzania, in an effective and environmentally friendly manner. As initial well conditions at Block 2 inhibit an efficient startup and well unloading, gravity-driven mud drainage to the near-wellbore zone during well suspension was investigated as a possible solution.

A coupled reservoir- and well/flowline model, constituting an OLGA and a ROCX model, was established based on a comprehensive grid sensitivity study. Prior to executing the simulations, sensitivity studies on formation- and fluid properties were conducted, to assess their effect on the drainage of mud during the well suspension and on the reservoir flushing after kickoff. Relative permeability- and capillary curves were estimated, due to lack of experimental core data for the specific reservoir. Furthermore, a skin factor was determined, used to model the mud cake at the wellbore wall during the suspension.

With a robust and efficient model obtained, based on the sensitivity studies, the simulation case was executed. Simulations aiming at the required suspension period, and the corresponding mud drainage volume, in order to obtain effective startup conditions in the well, were conducted. Furthermore, emphasis was made on the flushing of filtrate in the near-wellbore zone during early production. Of particular interest was the period of time the mud would affect the production.

As expected, the mud density and mud cake properties highly affect the drainage rate during the well suspension. The length of the damaged zone after drilling, on the other hand, showed a poor effect on the drainage rate. The well suspension simulations revealed that a suspension period of 7 days was required in order to drain a sufficient amount of mud from the well into the reservoir under the influence of gravity only. The suspension period resulted in a drained mass of 13.7 tons, constituting 13.5 tons of mud and 0.2 tons of brine. The dewatering operation required approximately 36.5 hours to complete, utilizing a PI controller retaining the pig velocity at 0.8 m/s. After 19 days, the drilling- and completion fluid content in the reservoir was reduced to 0.3 tons, and after 20 days, all the drilling- and completion fluids were produced out of the trunkline.

11 Recommendations for further work

In view of the results obtained in this thesis, there exists a great potential for further research on this field. A delay in the drainage starting point has been observed several times for the well suspension simulations. Firstly for over- and underpressures across the glass plug, and secondly for 4 grid cells in angular direction. What causes this delay is unknown and should be further investigated.

A pressure drop of 20 bar was assumed to be sufficient to collapse the mud cake at the wellbore inner wall. This assumption should be verified by experiments. As the collapse of the mud cake was modeled with a reduction in skin factor, the displacement of mud cake particles was not simulated. To accurately simulate the displacement and accumulation of mud cake particles and completion fluids during early production, the trunkline profile should be more detailed. Furthermore, emphasis should be made to find an efficient ramp-up strategy to empty the trunkline for drilling- and completion fluids as fast as possible.

OLGA and ROCX have proven to capture the exchange of heavy completion fluids with light reservoir gas during well suspension. However, the simulations are not verified against field data, thus, simulation of a well suspension where field data is obtainable should be performed. Alternatively, different simulation software could be utilized to verify the results obtained in this thesis.

Throughout this thesis, some limitations with the software have been observed. The following implementations are recommended for the software provider:

- Implement an accumulated variable for the flow over the near-well sources in OLGA
- Allowing a near-well source to be coupled with several grid cell boundaries in ROCX
- Implement drilling fluids in ROCX
- Allowing deviated wells with a horizontal near-well zone on a radial grid in ROCX

References

[1] Blunt, M.J. *Reservoir Engineering Lecture Notes.*

[2] Satter, Abdus and Iqbal, Ghulam M. “4 - Reservoir fluid properties”. In: *Reservoir Engineering.* Ed. by Abdus Satter and Ghulam M. Iqbal. Boston: Gulf Professional Publishing, 2016, pp. 81–105.

[3] Satter, Abdus and Iqbal, Ghulam M. “3 - Reservoir rock properties”. In: *Reservoir Engineering.* Ed. by Abdus Satter and Ghulam M. Iqbal. Boston: Gulf Professional Publishing, 2016, pp. 29–79.

[4] Kamyabi, F. “Multiphase Flows in Porous Media”. MA thesis. Norwegian University of Science and Technology, 2014.

[5] Ahmed, T. and McKinney, P.D. “Chapter 1 - Well Testing Analysis”. In: *Advanced Reservoir Engineering.* Gulf Professional Publishing, 2005, pp. 1–147.

[6] Ehinmowo, A. “Stabilizing slug flow at large valve opening using an intermittent absorber”. PhD thesis. Cranfield University, 2015.

[7] Solbraa, E. “Equilibrium and Non-Equilibrium Thermodynamics of Natural Gas Processing”. PhD thesis. Norwegian University of Science and Technology, 2002.

[8] Schlumberger. *OLGA User Manual.* 2017.

[9] Nydal, O.J. “Dynamic Models in Multiphase Flow”. In: American Chemical Society, 2012.

[10] Kjølaas, J. et al. “Experiments for Low Liquid Loading With Liquid Holdup Discontinuities in Two- and Three-Phase Flows”. In: *17th International Conference on Multiphase Production Technology.* Cannes, France: BHR group, 2015.

[11] Biberg, D. et al. “Comprehensive Experiments and Modelling Reduces Uncertainties in Liquid Management for the Tanzania Gas Project”. In: *Offshore Technology Conference.* Houston, Texas, 2017.

[12] Barnea, D. and Taitel, Y. “Structural and interfacial stability of multiple solutions for stratified flow”. In: *International Journal of Multiphase Flow* (1992).

[13] Kjølaas, J. et al. “Pressure drop measurements in low liquid loading three-phase flows”. In: *18th International Conference on Multiphase Production Technology.* Cannes, France: BHR group, 2017.

[14] Holm, H. “Tanzania gas development - flow assurance challenges”. In: *19th International Conference on Multiphase Production Technology.* BHR Group. 2019.

[15] Schlumberger. *ROCX User Manual.* 2017.

[16] *What are the main steps of an oil or gas field development project.* `https://ferasa.net/what-are-the-main-steps-of-an-oil-or-gas-field-development-project/`.

[17] Renpu, Wan. “Chapter 2 - Well Completion Mode Selection”. In: *Advanced Well Completion Engineering (Third Edition).* Ed. by Wan Renpu. Third Edition. Gulf Professional Publishing, 2011, pp. 75–116.

[18] Zhang, Jincai and Yin, Shang-Xian. “Fracture gradient prediction: an overview and an improved method”. In: Petroleum Science, 2017.

[19] Zain, Z.M. and Sharma, M.M. “Cleanup of Wall-Building Filter Cakes”. In: Society of Petroleum Engineers, 1999.

[20] *Completion fluids.* `https://www.halliburton.com/content/dam/ps/premium/common/PWC_Book/PWC12.PDF`.

[21] Hu, B., Xu, Z.G., and Uv, E.H. “Modelling and Simulation of the Co-Flow of Reservoir Fluids and Drilling/Completion Mud in the Ultra-Long Multilateral Horizontal Wellbores”. In: BHR Group, 2009.

[22] Solvang, B. et al. “History Matching the Clean-up of a Well at the Oselvar Field Using a Transient Multiphase Flow Simulator”. In: International Petroleum Technology Conference. 2014.

[23] Russel, D. “Pigging in pipeline pre-commissioning”. In: Pigging Products and Services Association. 2005.

[24] Guo, B. et al. “Offshore Pipelines (Second Edition)”. In: Gulf Professional Publishing, 2014. Chap. 14 - Pipeline Testing and Precommissioning.

[25] Falck, C and Maribu, J. “Commissioning 8000 Km of Subsea Pipelines”. In: International Society of Offshore and Polar Engineers. 2006.

[26] Smriti, Rao K. and Mishra, Ravi. “Comparative study of P, PI and PID controller for speed control of VSI-fed induction motor”. In: 2014.

[27] Zhang, G. et al. *Giant discoveries of oil and gas fields in global deepwaters in the past 40 years and the prospect of exploration.* 2018.

[28] MLandsverk, G.S. et al. “Multiphase Flow Behaviour at SnøHvit”. In: *14th International Conference on Multiphase Production Technology.* BHR Group. Cannes, France, 2009.

[29] Acworth, W. and Gray, V. *Ultra Long-Offset ’Subsea to Beach’ Controls Technology - Case Study Snøhvit.* Society of Petroleum Engineers, 2006.

[30] Burns, C. et al. “Start-up And Operation of the Ormen Lange Flowlines”. In: *The 18th International Offshore and Polar Engineering Conference.* Vancouver, Canada, 2008.

[31] Holm, H. “Tanzania gas development - flow assurance challenges”. In: *18th International Conference on Multiphase Production Technology.* BHR Group. Cannes, France, 2017.

A OLGA models

A.1 Stabilization model

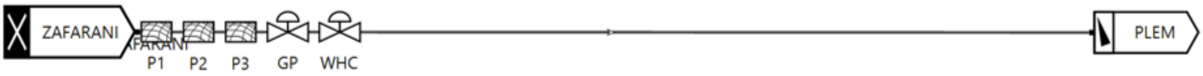
ZAFARANI
ZAFARANI
P1
P2
P3
GP
WHC
PLEM

Figure A.1: Stabilization model used in sensitivity studies

A.2 Simplified dynamic model

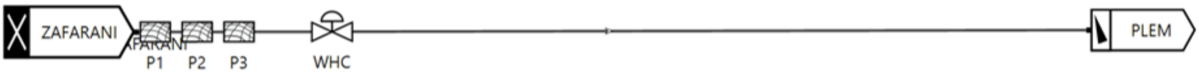
ZAFARANI
ZAFARANI
P1
P2
P3
WHC
PLEM

Figure A.2: Simplified dynamic model used in sensitivity studies

A.3 Simplified dynamic model for ny=8

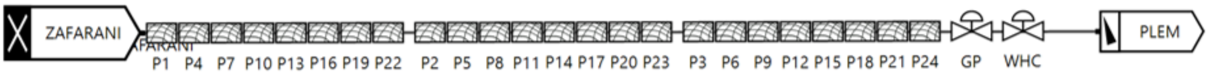
ZAFARANI
ZAFARANI
P1 P4 P7 P10 P13 P16 P19 P22
P2 P5 P8 P11 P14 P17 P20 P23
P3 P6 P9 P12 P15 P18 P21 P24
GP
WHC
PLEM

Figure A.3: Simplified dynamic model used to assess a gridding with ny=8

A.4 Simplified suspension model

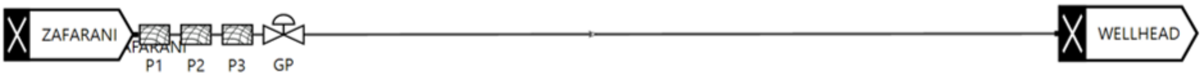
ZAFARANI
ZAFARANI
P1
P2
P3
GP
WELLHEAD

Figure A.4: Simplified suspension model used in sensitivity studies

A.5 Complete suspension model and early production model

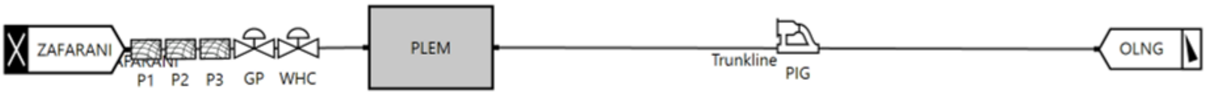
ZAFARANI
ZAFARANI
P1
P2
P3
GP
WHC
PLEM
Trunkline
PIG
OLNG

Figure A.5: Suspension model for the actual simulation case

A.6 Well cleanup and dewatering model

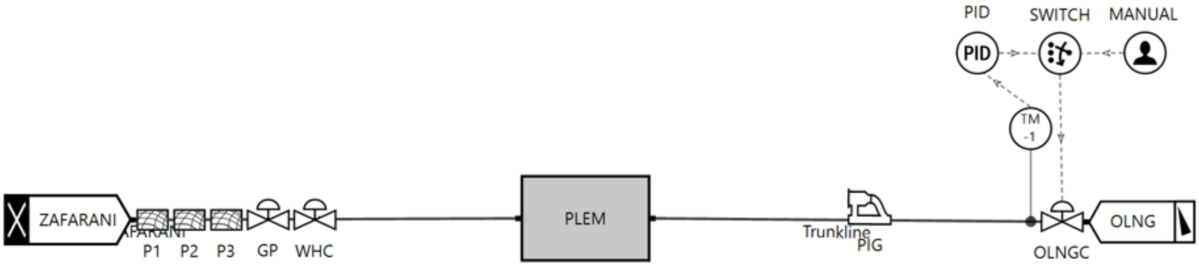
PID
SWITCH
MANUAL
PID
TM
-1
ZAFARANI
P1
P2
P3
GP
WHC
PLEM
Trunkline
PIG
OLNGC
OLNG

Figure A.6: Combined well cleanup and dewatering model with PI controller

B ROCX models

B.1 Model with ny=8

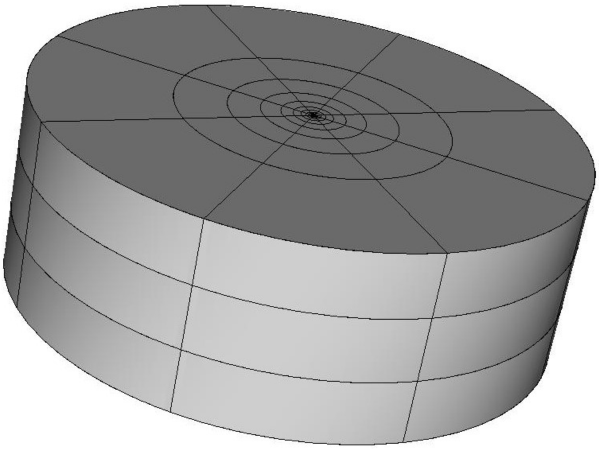

Figure B.1: Model used to assess a gridding with ny=8

B.2 Final model

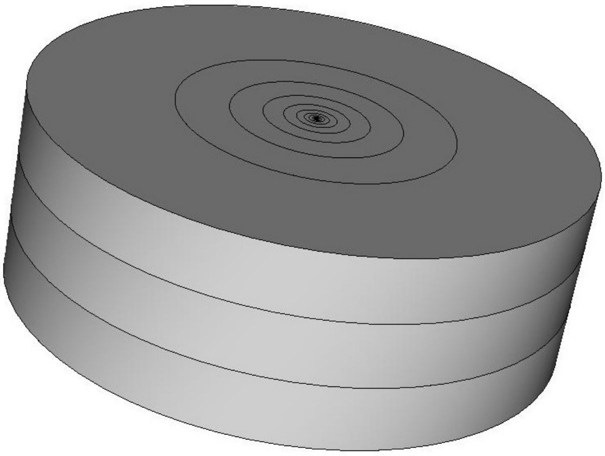

Figure B.2: Final model obtained from grid sensitivity studies

C Near-wellbore radius

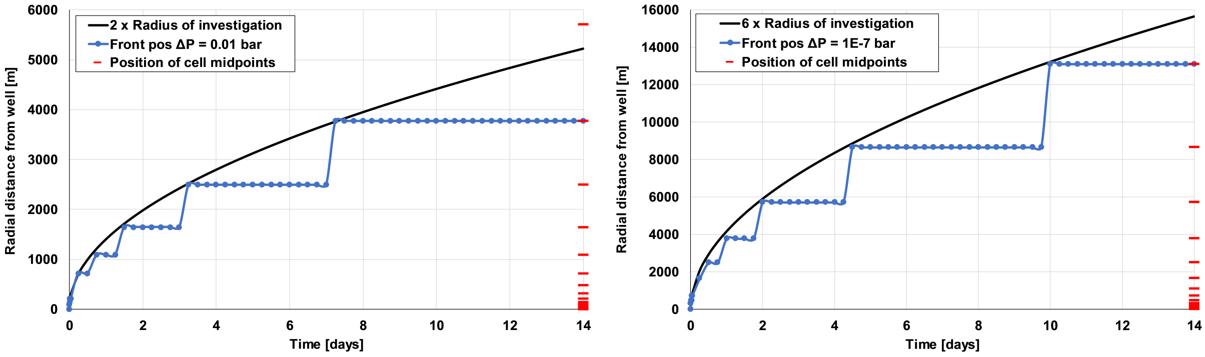

(a) (b)

Figure C.1: Position of the pressure front for a) $\Delta P = 0.01$ and b) $\Delta P = 1E-7$

D Grid sensitivity study

D.1 Vertical gridding in ROCX

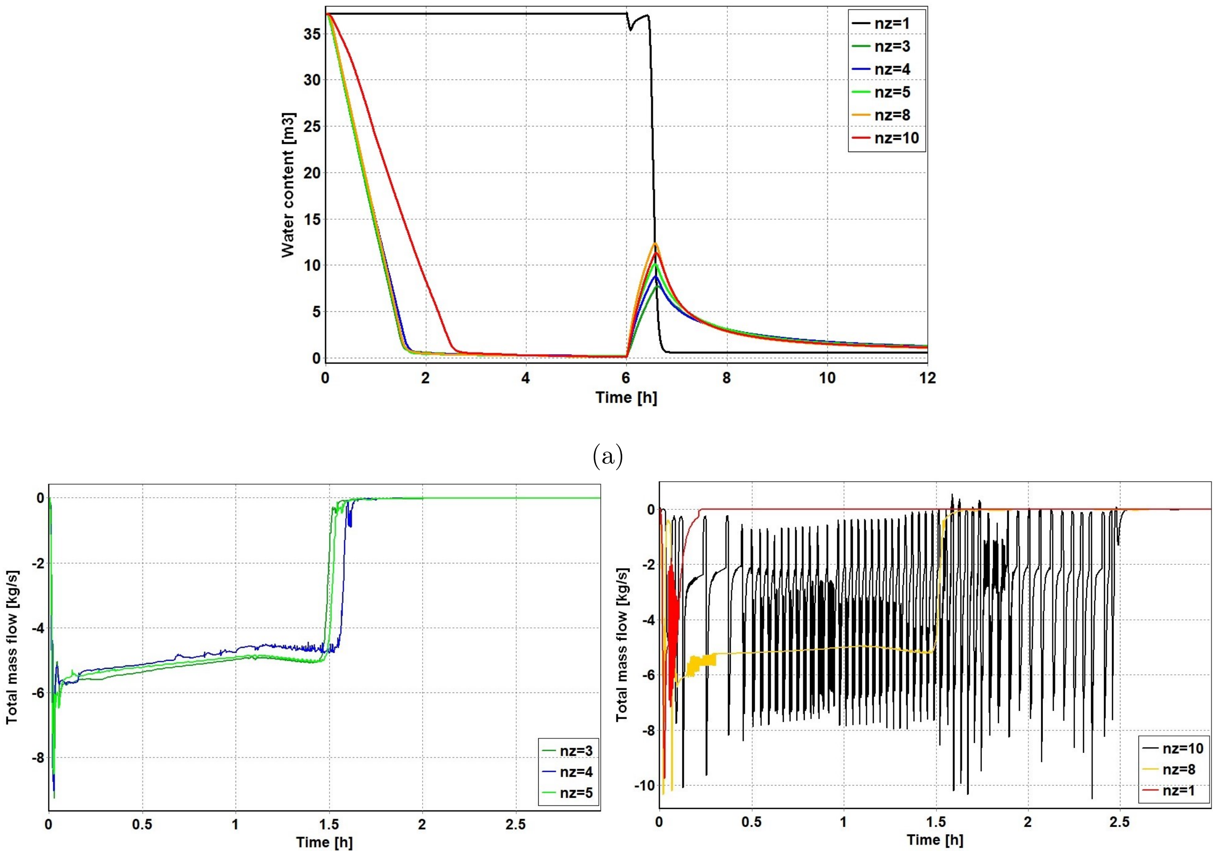

(a)

(b) (c)

Figure D.1: a) Water content in the well and b), c) total mass flow above perforation during drainage for different number of grid blocks in z-direction

D.2 Radial gridding in ROCX

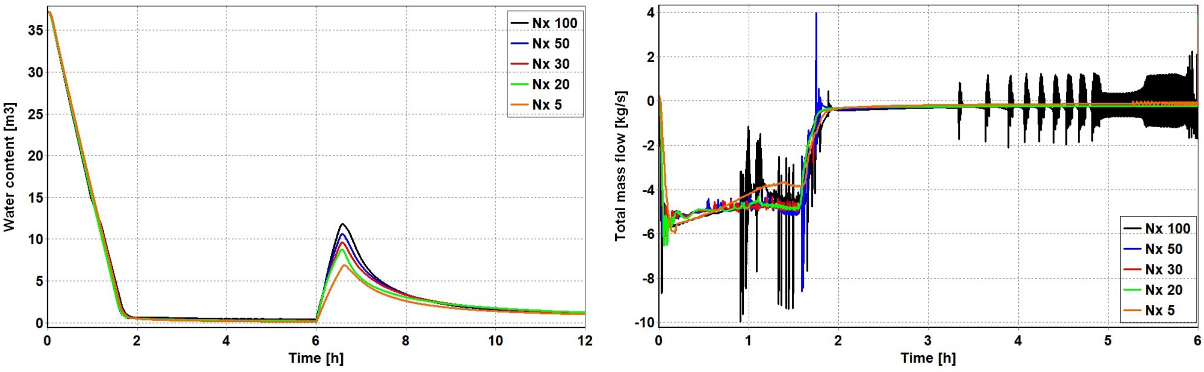

(a) (b)

Figure D.2: a) Water content in the well and b) total mass flow over the near-well source located at the bottom of the perforation zone

D.3 Angular gridding in ROCX

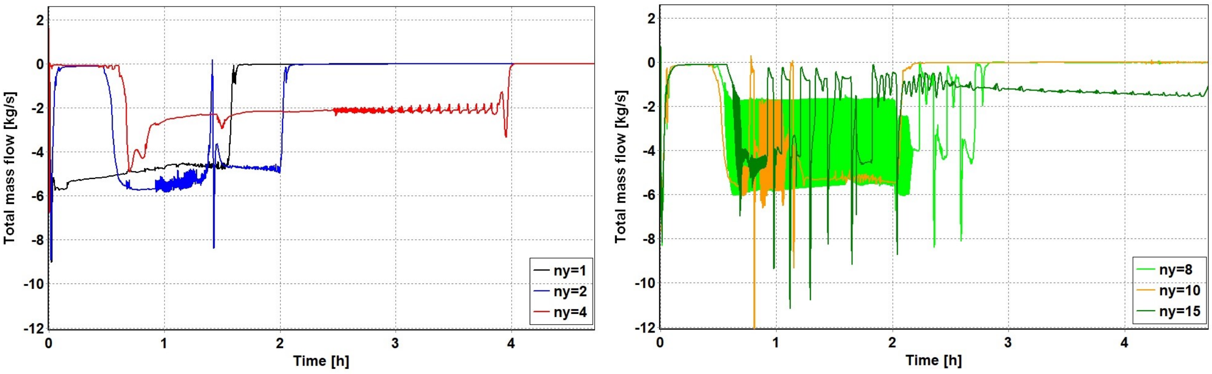

(a) (b)

Figure D.3: Total mass flow above perforation during the drainage for different number of grid blocks in angular direction

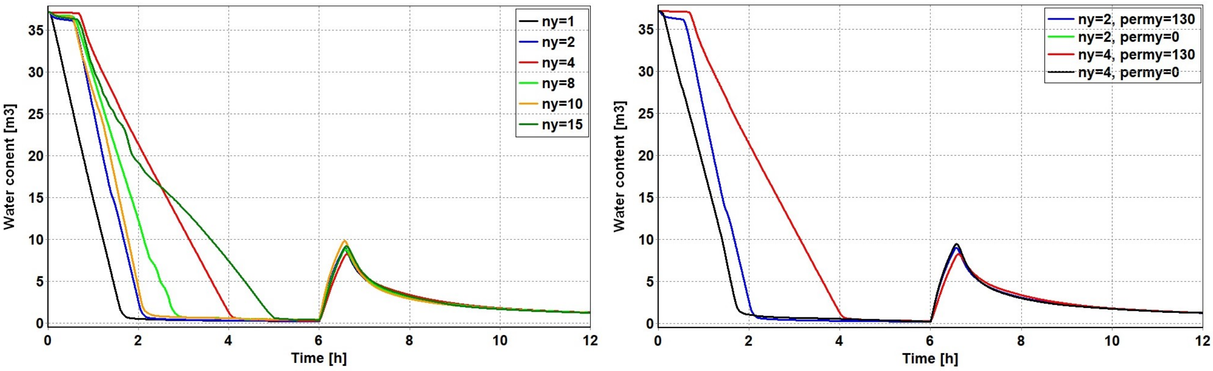

(a) (b)

Figure D.4: Water content in the well for different number of grid blocks in angular direction

D.4 Gridding in OLGA

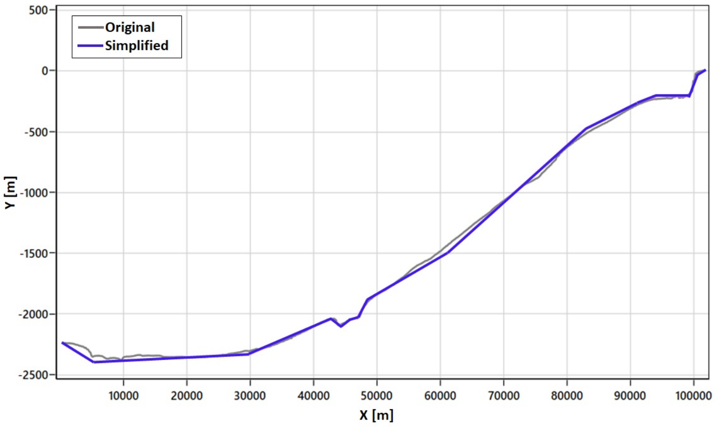

Figure D.5: Comparison of original flowline profile and simplified flowline profile

E Tuning of PID controller

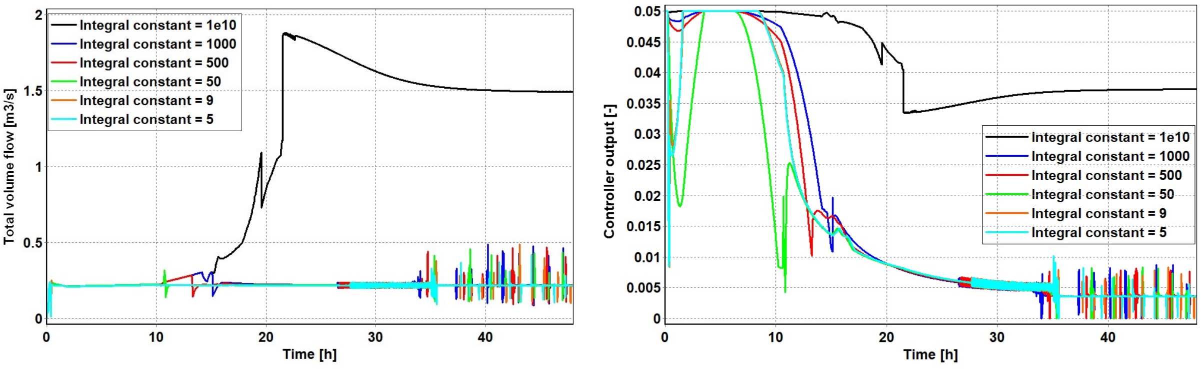

(a)

(b)

Figure E.1: a) Flow rate recorded by transmitter and b) output from PID controller for different integral constants

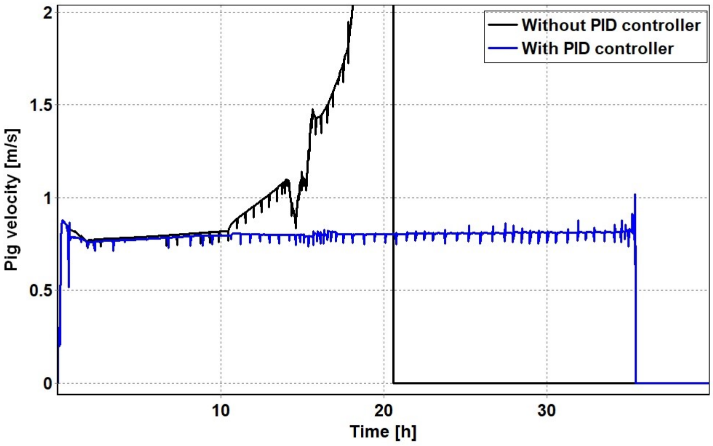

Figure E.2: Pig velocity with and without controller

F Well suspension

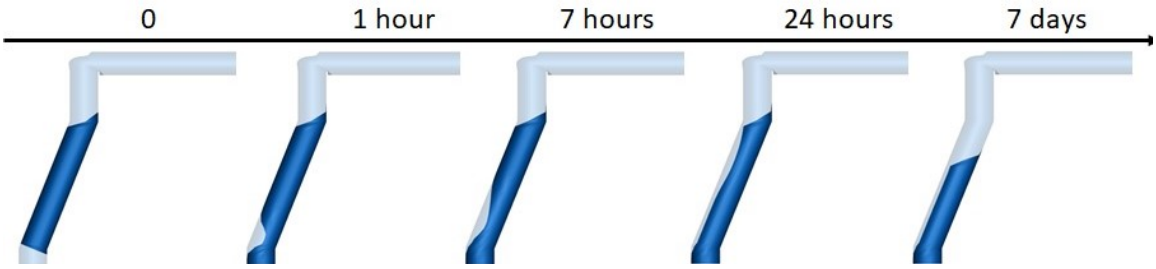
0
1 hour
7 hours
24 hours
7 days

Figure F.1: 7 days well suspension

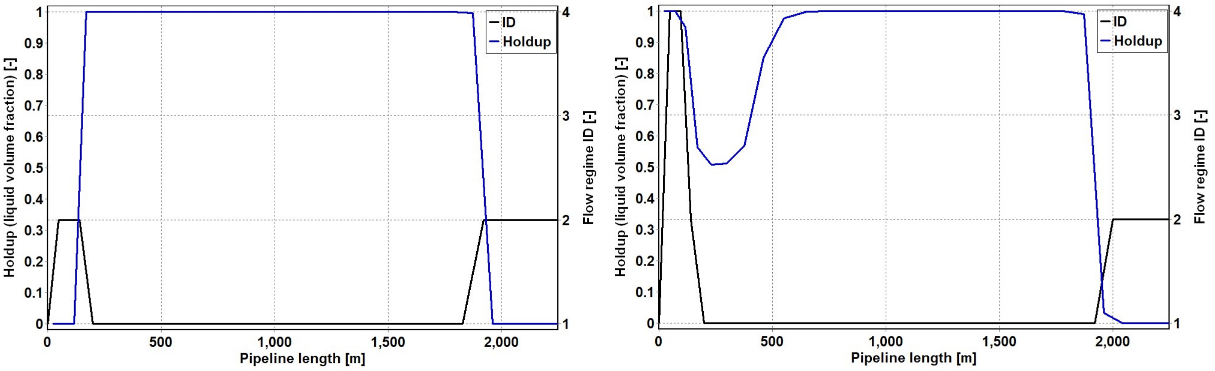

(a) Initially

(b) After 1 hour

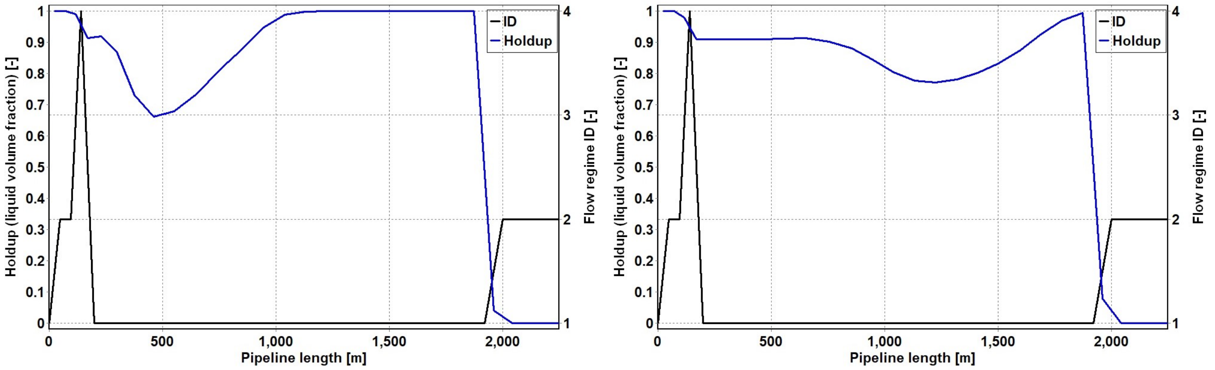

(c) After 7.5 hours

(d) After 22 hours

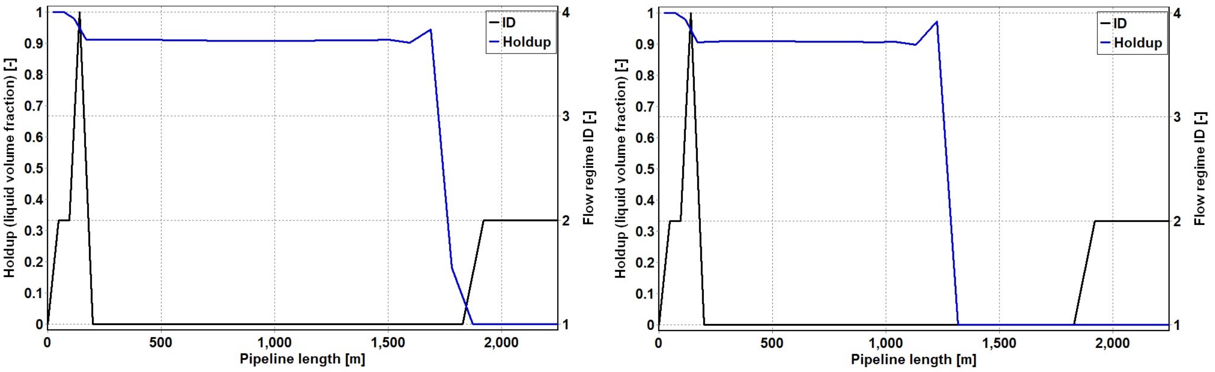

(e) After 2 days

(f) After 7 days

Figure F.2: Holdup and flow regime ID (1=stratified, 2=Annular, 3=slug, 4=Bubble) in the well during 7 days of well suspension

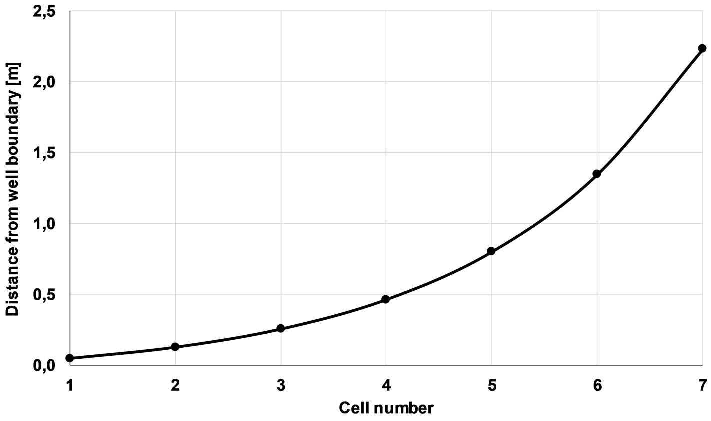

Figure F.3: Distance from the well boundary to each cell midpoint for the 7 cells closest to the well

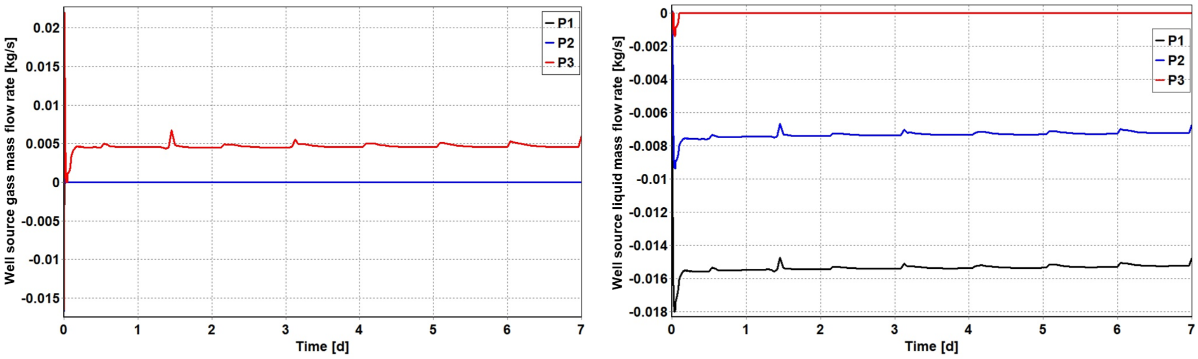

(a) (b)

Figure F.4: Gas and liquid mass flow rate over the near-well sources

G Well cleanup, dewatering and early production

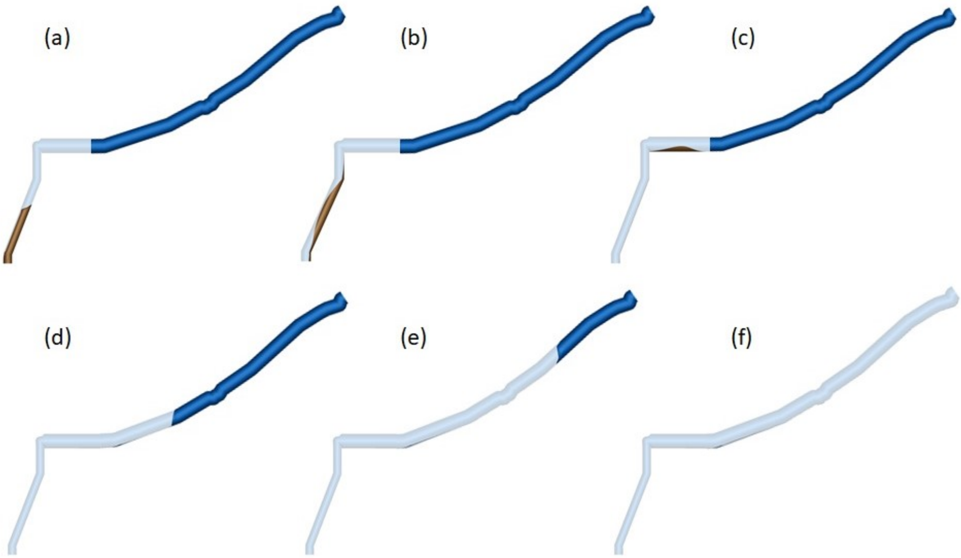

Figure G.1: a) Initial and after b) 2 min, c) 20 min, d) 10 hours, e) 26 hours and f) 36 hours

NTNU
Norwegian University of
Science and Technology